AN EXPERIMENTAL STUDY ON THE PERFORMANCE OF AN ADSORPTION COOLING SYSTEM AND THE NUMERICAL ANALYSIS OF ITS ADSORBENT BED

A THESIS SUBMITTED TO
THE GRADUATE SCHOOL OF NATURAL AND APPLIED SCIENCES
OF
MIDDLE EAST TECHNICAL UNIVERSITY

BY

İSMAİL SOLMUŞ

IN PARTIAL FULFILLMENT OF THE REQUIREMENTS
FOR
THE DEGREE OF DOCTOR OF PHILOSOPHY
IN
MECHANICAL ENGINEERING

DECEMBER 2011

Approval of the thesis:

AN EXPERIMENTAL STUDY ON THE PERFORMANCE OF AN ADSORPTION COOLING SYSTEM AND THE NUMERICAL ANALYSIS OF ITS ADSORBENT BED

submitted by **İSMAİL SOLMUŞ** in partial fulfillment of the requirements for the degree of **Doctor of Philosophy in Mechanical Engineering Department, Middle East Technical University** by,

Prof. Dr. Canan Özgen
Dean, Graduate School of **Natural and Applied Sciences**

Prof. Dr. Suha Oral
Head of Department, **Mechanical Engineering**

Assoc. Prof. Dr. Cemil Yamalı
Supervisor, **Mechanical Engineering Dept., METU**

Prof. Dr. Bilgin Kaftanoğlu
Co-supervisor, **Manufacturing Engineering Dept., Atılım University**

Examining Committee Members:

Prof. Dr. Kahraman Albayrak
Mechanical Engineering Dept., METU

Assoc. Prof. Dr. Cemil Yamalı
Mechanical Engineering Dept., METU

Assoc. Prof. Dr. Derek Baker
Mechanical Engineering Dept., METU

Prof. Dr. Mecit Sivrioğlu
Mechanical Engineering Dept., Gazi University

Prof. Dr. Haşmet Türkoğlu
Mechanical Engineering Dept., Gazi University

Date:

I hereby declare that all information in this document has been obtained and presented in accordance with academic rules and ethical conduct. I also declare that, as required by these rules and conduct, I have fully cited and referenced all material and results that are not original to this work.

Name, Last Name: İSMAİL SOLMUŞ

Signature :

ABSTRACT

AN EXPERIMENTAL STUDY ON THE PERFORMANCE OF AN ADSORPTION COOLING SYSTEM AND THE NUMERICAL ANALYSIS OF ITS ADSORBENT BED

Solmuş, İsmail
Ph.D., Department of Mechanical Engineering
Supervisor : Assoc. Prof. Dr. Cemil Yamalı
Co-Supervisor : Prof. Dr. Bilgin Kaftanoğlu
December 2011, 150 pages

In this thesis, firstly, the equilibrium adsorption capacity of water on a natural zeolite at several zeolite temperatures and water vapor pressures has been experimentally determined for adsorption and desorption processes. Additionally, the modified Dubinin-Astakhov adsorption equilibrium model has been fitted to experimental data and separate correlations are obtained for adsorption and desorption processes as well as a single correlation to model both processes. Experimental results show that the maximum adsorption capacity of natural zeolite is nearly 0.12 $\mathrm{kg_w/kg_{ad}}$ for zeolite temperatures and water vapor pressures in the range 40-150 °C and 0.87-7.38 kPa. Secondly, a thermally driven adsorption cooling prototype using natural zeolite-water as working pair has been built and its performance investigated experimentally at various evaporator temperatures. Under the experimental conditions of 45 °C adsorption, 150 °C desorption, 30 °C condenser and 22.5 °C, 15 °C and 10 °C evaporator temperatures, the COP of the adsorption cooling unit is approximately 0.25 and the maximum average volumetric specific cooling power density (SCP_v) and mass specific cooling power density (SCP) of the cooling unit are 5.2 $\mathrm{kWm^{-3}}$ and 7 $\mathrm{Wkg^{-1}}$, respectively. Thirdly, in order to investigate the dynamic heat and mass transfer behavior of the adsorbent bed of an adsorption cooling unit, a transient local thermal non equilibrium model that accounts for both internal and external mass transfer resistances has been developed using the local volume averaging method. Finally, the influence of several design parameters on the transient distributions of temperature, pressure and amount adsorbed inside the cylindrical adsorbent bed of an adsorption cooling unit using silica-gel/water have been numerically investigated for the one and two dimensional computational domains. Moreover, validity of the thermal equilibrium model assumption has been shown under the given boundary and design conditions. Generally, for the conditions investigated, the validity of the local thermal equilibrium and spatially isobaric bed assumptions have been confirmed. To improve the performance of the bed considered, efforts should be focused on reducing heat transfer resistances and intra-particle mass transfer resistances but not inter-particle mass transfer resistances.

Keywords: Adsorption, Cooling, Porous, Natural zeolite/water, Silica gel/water

ÖZ

ADSORPSİYONLU SOĞUTMA SİSTEMİNİN PERFORMANSI ÜZERİNDE DENEYSEL BİR ÇALIŞMA VE SİSTEMİN ADSORBAN YATAĞININ SAYISAL ANALİZİ

Solmuş, İsmail
Doktora, Makina Mühendisliği Bölümü
Tez Yöneticisi : Doç. Dr. Cemil Yamalı
Ortak Tez Yöneticisi : Prof. Dr. Bilgin Kaftanoğlu

Aralık 2011, 150 sayfa

Bu çalışmada, ilk olarak, zeolit su çalışma çiftine ait eş sıcaklık eğrileri adsorpsiyon ve desorpsiyon prosesleri için çeşitli zeolit sıcaklıkları ve su buharı basınçlarında deneysel olarak elde edilmiştir. Ayrıca, Dubinin-Astakhov adsorpsiyon denge denklemi elde edilen deney verilerine uyarlanmış ve bunun sonucunda adsorpsiyon ve desorpsiyon prosesinin yanı sıra her iki proseside kapsayan korelasyon denklemlerine ulaşılmıştır. Deneyler sonucunda doğal zeolitin maksimum su buharı adsorplama kapasitesi, 40-150 °C zeolit sıcaklığı ve 0.87-7.38 kPa su buharı basıncı aralığında yaklaşık 0.12 $\mathrm{kg_{su}/kg_{ad}}$ olarak bulunmuştur. İkinci olarak, doğal zeolit-su çalışma çiftini kullanan termal enerji destekli adsorpsiyonlu örnek soğutma grubu üretilmiş ve bu soğutma grubunun performansı farklı buharlaştırıcı sıcaklıklarında deneysel olarak incelenmiştir. Adsorpsiyon sıcaklığının 45 °C, desorpsiyon sıcaklığının 150 °C, yoğuşturucu sıcaklığının 30 °C olduğu farklı buharlaştırıcı sıcaklıkları (22.5, 15 ve 10 °C) için prototip soğutma sisteminin ortalama COP değeri 0.25 olarak bulunmuştur. Prototip soğutma sisteminin maksimum hacimsel özgül soğutma miktarı (SCP_v) ve ortalama kilogram adsorban başına özgül soğutma miktarı (SCP) sırasıyla 5.2 $\mathrm{kWm^{-3}}$ and 7 $\mathrm{Wkg^{-1}}$ mertebesindedir. Üçüncü olarak, adsorpsiyonlu bir soğutma sisteminde mevcut olan adsorban yatağın dinamik davranışını ısı ve kütle transferi bakımından incelemek için, lokal hacimsel ortalama method kullanılarak zamana bağlı lokal olarak ısıl dengenin olmadığı, iç ve dış kütle transfer dirençlerinin dikkate alındığı bir sayısal model geliştirilmiştir. Son olarak, çeşitli tasarım parametrelerinin, silika jel/su çalışma çiftini kullanan adsorpsiyonlu bir soğutma sisteminin silindirik adsorban yatağı içerisinde zamana bağlı sıcaklık, basınç ve adsorpsiyon miktarı dağılımı üzerine olan etkileri bir ve iki boyutlu hesaplama sınırları için sayısal olarak araştırılmıştır. Ayrıca, yatak içerisinde lokal ısıl denge modeli varsayımının geçerliliği verilen sınır ve tasarım koşulları altında incelenmiştir. Genel olarak, incelenen koşullar için, lokal ısıl denge modelinin ve izo barik yatak varsayımının geçerliliği doğrulanmıştır. Söz konusu adsorban yatağın performansını iyileştirmek için, ısı transferi dirençlerinin ve dış (iç değil) kütle transfer dirençlerinin azaltılması yönünde uğraş verilmelidir.

Anahtar Kelimeler: Adsorpsiyon, Soğutma, Gözenekli, Doğal zeolit/su, Silika jel/su

To my daughter, Duru

ACKNOWLEDGMENTS

I am deeply grateful to my supervisor, Assoc. Prof. Dr. Cemil Yamalı, for his guidance, inspiration, and invaluable help all throughout my study.

I would like to thank to my co-supervisors Prof. Dr. Bilgin Kaftanoğlu and Assoc. Prof. Dr. Derek Baker for their precious advices and continuous support.

I wish to express my sincere thanks to Professor D. Andrew S. Rees (Mechanical Engineering Department, University of Bath, UK) for his hospitality and warm friendship during my study at the University of Bath and valuable contributions to the numerical part of this study.

I also would like to thank The Scientific and Technological Research Council of Turkey (TÜBİTAK) and the Middle East Technical University for supporting me with a fellowship during my study at the University of Bath, UK.

I gratefully acknowledge Mustafa Yalçın, for his technical assistance in manufacturing and operating the experimental setups.

I furthermore wish to express my deepest gratitude to each member of my family for provided me a comfortable and excellent environment.

Finally, I offer sincere appreciation to my wife, Saçak, for her continuous encouragement, understanding and support.

The experimental parts of this work is supported by The Scientific and Technological Research Council of Turkey (TÜBİTAK) project 105M244 and Ataç Holding Company, Antalya, Turkey.

TABLE OF CONTENTS

CHAPTERS

LIST OF TABLES

TABLES

LIST OF FIGURES

FIGURES

LIST OF ABBREVIATIONS

ABBREVATIONS

A_{gs}	area of the g-s interface, m^{2}
a_v	area of g-s interface per unit volume of the packed bed, m^{-1}
C_g	mass rate of adsorption, kg$_{\mathrm{w}}$m^{-2}s^{-1}
COP	coefficient of performance
c_p	heat capacity, Jkg^{-1}K^{-1}
D_e	equivalent diffusivity in the adsorbent particles, m^{2}s^{-1}
D_g	diffusivity of adsorbate gas, m^{2}s^{-1}
D_k	Knudsen diffusivity, m^{2}s^{-1}
D_m	molecular diffusivity, m^{2}s^{-1}
D_o	reference diffusivity, m^{2}s^{-1}
D_s	surface diffusivity, m^{2}s^{-1}
D_{so}	structural constant of the adsorbent material
d_p	diameter of the adsorbent particle, m
d_{pore}	average pore diameter, m
E_a	activation energy of surface diffusion, kJkg^{-1}
h	convective heat transfer coefficient, Wm^{-2}K^{-1}
h_{gs}	interfacial convective heat transfer coefficient, Wm^{-2}K^{-1}
K_a	apparent permeability, m^{2}
K_d	real permeability, m^{2}
k_m	mass transfer coefficient within the adsorbent particles, s^{-1}
k	thermal conductivity, Wm^{-1}K^{-1}
L	latent heat of the water, kJkg^{-1}
M	molar mass, kgmol^{-1}
m	mass, kg
Nu	Nusselt number
P	pressure, kPa

Pr	Prandtl number
Q	enerji, kJ
Q_{ad}	isosteric heat of adsorption, $\mathrm{kJkg_w^{-1}}$
Q_s	volumetric heat generation, $\mathrm{Wm^{-3}}$
R	universal gas constant, $\mathrm{Jmol^{-1}K^{-1}}$
Re	Reynolds number
R_i	inner diameter of the adsorbent bed, m
R_o	outer diameter of the adsorbent bed, m
R_w	specific gas constant for water, $\mathrm{kJkg^{-1}K^{-1}}$
r	radial coordinate, m
r_p	radius of the adsorbent particle, m
SCP	mass specific cooling power density, $\mathrm{Wkg^{-1}}$
SCP_v	volumetric cooling power density, $\mathrm{kWm^{-3}}$
T	temperature, K
t	time, min
V	volume, $\mathrm{m^3}$
v	velocity, $\mathrm{ms^{-1}}$
v_r	gas phase velocity in radial direction, $\mathrm{ms^{-1}}$
v_z	gas phase velocity in axial direction, $\mathrm{ms^{-1}}$
X	amount adsorbed or adsorption capacity, $\mathrm{kg_w kg_{ad}^{-1}}$
z	axial coordinate, m

GREEK SYMBOLS

μ	viscosity, $\mathrm{Nsm^{-2}}$
ρ	density, $\mathrm{kgm^{-3}}$
ϵ	volume fraction
ϵ_t	total porosity
ϵ_b	bed porosity
ϵ_p	particle porosity
τ	tortuosity
σ	collision diameter for Lennard-Jones potential
Ω	collision integral
λ_{ge}	effective thermal conductivity tensor for the gas phase, $\mathrm{Wm^{-1}K^{-1}}$

λ_{gs}	stagnant thermal conductivity tensor for the gas phase, $\mathrm{Wm^{-1}K^{-1}}$
λ_{gd}	thermal dispersion tensor for the gas phase, $\mathrm{Wm^{-1}K^{-1}}$
λ_{se}	effective thermal conductivity tensor for the solid phase, $\mathrm{Wm^{-1}K^{-1}}$

SUBSCRIPTS

a	adsorption
ad	adsorbent
$ad-c$	adsorbent cold
$ad-h$	adsorbent hot
b	boundary
c	condenser
cy	cycle
d	desorption
ev	evaporator
$ev-f$	evaporator final
$ev-i$	evaporator initial
g	adsorbate gas
gs	gas-solid interface
i	input
l	loss
max	maximum
min	minimum
r	refrigeration
s	solid adsorbent
sat	saturation
u	useful
v	vapor
w	water
∞	equilibrium
$\tilde{}$	deviation
$\langle\rangle$	phase average
$\langle\rangle^g$	intrinsic phase average
$\langle\rangle_{gs}$	area average

CHAPTER 1

INTRODUCTION

1.1 THERMAL POWERED ADSORPTION COOLING SYSTEMS

As noted previously, Turkey is a rapidly developing country and electrical demand is projected to grow at an annual rate of 6-8 % for the next 10 years [1]. Currently, approximately 40 % of Turkey's electricity is generated using natural gas, almost all of which is imported. Additionally, approximately 40 % of electricity is generated using coal. The majority of the remaining electricity demand of Turkey is generated from hydroelectric [2, 3].

Turkey's growth in electrical demand is driven in part by an increase in cooling demand, particularly along the Mediterranean and Aegean coasts that are characterized by long and hot summers. In addition to being two of the more heavily populated and developed regions in Turkey, these regions have a very large and economically important tourism industry. Many of the largest population and tourist centers in these regions are presently not served by natural gas lines. While some large buildings and resorts use absorption chillers fired by liquefied natural gas, much of the cooling demand, even in large buildings, is met using traditional room-sized electrically-driven vapor-compression (VC) air conditioners. Traditional air-conditioning technologies can have numerous adverse impacts due to both the energy they consume and the refrigerants used including the following: contributing to environmental problems such as climate change, ozone depletion, and pollution [4–9]; contributing to infrastructure problems by stressing the electric generating, transmission and distribution infrastructure by increasing the peak demand for electricity [5]; contributing to economic problems through the cost of supplying this energy [5, 6]; and reducing energy security if energy must be imported to meet this demand [8]. However, these problems related to cooling demand are not unique to Turkey and have been discussed previously in the literature; e.g., [10–12].

Thermally driven cooling systems powered using solar energy or waste heat such as absorption, adsorption, and desiccant systems have the potential to reduce or eliminate many of these problems [7, 9]. The present work is focused on adsorption cooling systems and their adsorbent beds. Dieng and Wang provide an excellent overview of this technology [13].

Thermal powered adsorption cooling (TPAC) systems have received much attention in the recent years since they are environmentally friendly and can be operated with low-grade heat sources such as solar energy or waste heat. With both the Mediterranean and Aegean coasts as well as many other regions in Turkey enjoying large summer solar resources, the widespread commercialization of solar-driven adsorption air-conditioning systems in Turkey could help reduce many of the problems related to cooling demand. The heart of this technology is a thermal compression process using an adsorbent bed that replaces the mechanical compression process in a vapor-compression cycle. This adsorbent bed is alternately cooled and heated, which in turn alternately causes the bed to adsorb refrigerant at a low pressure and desorb refrigerant at high pressure, thus producing a thermally powered compression process. However, these systems are not competitive with electrically-driven refrigeration systems due to their high investment costs and low coefficient of performance. Therefore, extensive efforts have been exerted by researchers to improve their coefficient of performance and make them commercially viable.

1.2 PRINCIPLES OF THE ADSORPTION

The process of adsorption involves separation of a substance from one phase accompanied by its accumulation or concentration at the surface of another and it occurs at the surface interface of two phases. The adsorbing phase is the adsorbent (for a water-zeolite system, the adsorbent is zeolite) and the material adsorbed at the surface of that phase is the adsorbate (for a water-zeolite system, the adsorbate is water). Figure 1.1 indicates the simulated adsorption of methanol in zeolite [14]. The zeolite is represented by red (oxygen) and grey (silicon) sticks and methanol by white (hydrogen), blue (oxygen) and grey (carbon) spheres. Adsorption process can be classified as either chemical or physical. Chemical adsorption occurs as covalent or ionic bonds are formed between the adsorbing molecules and the solid substance. The process may not be completely reversible. Physical adsorption occurs as Van der Waals forces bind the adsorbing molecule to the solid phase. The process is always completely reversible

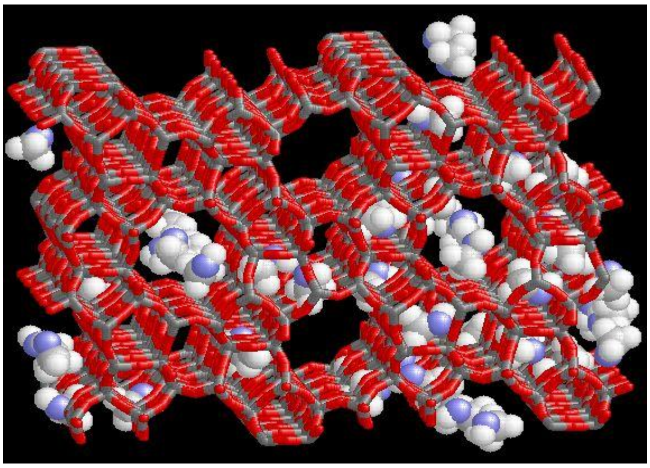

Figure 1.1: The simulation adsorption of methanol in zeolite [14].

by applying heat. Hence, physical adsorption (not chemical) typically occurs in adsorption cooling systems.

Adsorption is accompanied by evolution of heat. The heat of adsorption is the amount of energy released during the adsorption process. It is usually 30-100 % higher than that of condensation of the adsorbate. Heat of adsorption is either derived from adsorption isotherms (i.e., the saturation loading for adsorbent varies with temperature of the adsorbent and the partial pressure of the adsorbate and generally, this information is presented by plotting isotherms on saturation loading versus partial pressure graphs) or, as the differential heat of adsorption determined experimentally using a calorimetric method. Differential heat of adsorption for some adsorbent/adsorbate pairs are given in Table 1.1 [15]. The performance of adsorbents used in physical adsorption is governed by surface properties, such as surface area, micro-pores and macro-pores, size of granules in powders, crystals or in pellets. Adsorbents having special affinity with polar substances like water are termed 'hydrophilic'. These include silica gel, zeolites and porous or active alumina. Non-polar adsorbents, termed 'hydrophobic', have more affinity for oils and gases than for water. These substances include activated carbons, polymer adsorbents and silicalites.

Adsorbents are characterized by surface properties such as surface area and polarity. A large specific surface area is preferable for providing large adsorption capacity, but the creation of a large internal surface area in a limited volume inevitably gives rise to large numbers of small

Table 1.1: Differential heat of adsorption for some adsorbent/adsorbate pairs.

Adsorbent	Adsorbate	Heat of adsorption ($kJkg^{-1}$)	Remarks
Activated alumina	Water	3000	Water is applicable except for very low operating pressures
Zeolite (various grades)	Water	3300−4200	Natural zeolites have lower values than synthetic zeolites
	Ammonia	4000−6000	
	Carbondioxide	800−1000	
	Methanol	2300−2600	
Silica gel	Methyl alcohol	1000−1500	Not suitable above 200 °C
	Water	2800	Used mostly for desiccant cooling
Charcoal	C_2H_4	1000−1200	Reacts at approximate 100 °C
	Ammonia	2000−2700	not compatible with copper at high temperature
	Water	2300−2600	
	Methanol	1800−2000	not compatible with copper at high temperature
	C_2H_5OH	1200−1400	

sized pores between adsorption surfaces. The pore size distribution of micro pores, which determines the accessibility of adsorbate molecules to the internal adsorption surface, is important for characterizing adsorptivity of adsorbents [16].

1.2.1 Selection of adsorbent/adsorbate pairs

The choice of the adsorbate should be depend mainly on the following factors [15, 16]:

- evaporation temperature below 0 °C
- high latent heat of vaporization and low specific volume
- low saturation pressures (slightly above atmospheric) at normal operating temperature
- small size of molecules such that it can easily be adsorbed into the adsorbent
- high thermal conductivity and good thermal stability
- low viscosity and specific heat
- non-toxic, non-inflammable, non-corrosive and chemically stable in the working temperature range

The selected adsorbent should have the following positive attributes [15, 16]:

- high adsorption and desorption capacity, to attain high cooling effect
- good thermal conductivity and low specific heat capacity
- possession of high latent heat of adsorption compared to its sensible heating load
- chemically compatible with the chosen refrigerant
- low cost, widely available and no deterioration with age or use

Based on the above criteria, some of the appropriate working pairs are zeolite-organic refrigerants, silica gel-water, zeolite-water and activated carbon- methanol in solid adsorption systems.

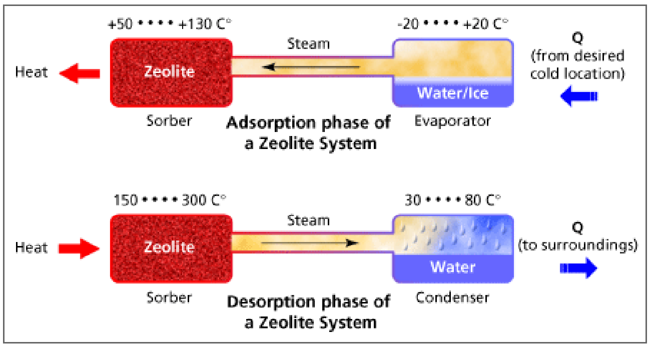

Figure 1.2: The adsorption and desorption processes of the water in zeolite [17].

1.3 FUNDAMENTALS OF THE ADSORPTION COOLING TECHNOLOGY

The adsorption and desorption processes of the water in zeolite can be explained with the help of the Figure 1.2. If the adsorption process proceeds in an evacuated (airless) environment, the attraction of water by the zeolite is so forceful that the internal pressure drops dramatically. The remaining water in an attached vessel evaporates, cools down and freezes immediately due to the heat of evaporation. The resulting ice can be used for cooling and air conditioning while the simultaneously produced heat of adsorption within the zeolite tank can be utilized for heating. If a valve is included between the two vessels, the heat or cold production can be interrupted for any periods without loss of energy. The first phase of this process proceeds up to the point when the zeolite is saturated with water. The reverse process is initiated by heating the zeolite at high temperatures in the second phase. The adsorbed water molecules are forced to evaporate (desorption). Condensation takes place in the water tank (condenser). The sequence of adsorption/desorption processes can be repeated indefinitely [17].

1.4 SURVEY OF LITERATURE

The following is a review of the literature most important for the adsorption properties of the various adorbate/adsorbent working pairs, thermal powered adsorption cooling systems and dynamic heat and mass transfer behavior of the adsorbent bed of the adsorption cooling units, respectively.

1.4.1 Adsorption properties of the various adsorbate/adsorbent working pairs

Over the past few decades, many researchers have conducted experimental studies to investigate the equilibrium adsorption capacity and thermodynamic properties of different adsorbent-refrigerant working pairs at various equilibrium conditions. The following is a brief review of the literature most important for the present work. El-Sharkawy et.al [18] measured the adsorption capacity of ethanol on Unitika activated carbon fiber of types A-20 and A-15 for adsorption cooling system applications. Ng et. al. [19] studied experimentally the adsorption characteristics of silica gel (specifically Fuji Davison Type A, Type 3A and Type RD)-water working pairs for the sizing of adsorption chillers. Additionally, the authors determined the isosteric heat of adsorption of these working pairs. Cui et. al. [20] developed a family of new composite adsorbents, NA and NB. In their study, the comprehensive experimental study of the adsorption capacity and kinetics of adsorption/desorption cycles of new composite adsorbents of NA, NB, 13x molecular sieve, silica gel and activated carbon paired with water and ethanol were performed. Wang et. al. [21] improved an adsorption model for adsorption refrigeration pairs such as activated carbon-methanol and zeolite water, and this model was verified by various experimental results. In another study, Wang et. al. [22] investigated the adsorption properties three types of adsorption working pairs (activated carbon-methanol, activated carbon-ammonia and composite adsorbent-ammonia) and evaluated their applicability to refrigeration applications. Loh et. al. [23] presented the relationships between equilibrium pressures, adsorbent temperatures and equilibrium adsorption capacity of ACF (A-15)-ethanol, ACF (A-20)-ethanol, silica gel-water, Chemviron-R134a, Fluka-R134a and MaxsorbII-134a working pairs. By using these adsorption working pairs, the performance analysis of both ideal single-stage and single-effect double-lift adsorption cooling cycles working at partially evacuated and pressurized conditions were carried out. Saha et. al. [24] measured the adsorption isotherms of n-butane on pitch based activated carbon (type Maxsorb III) and calculated the isosteric heat of adsorption of n-butane on Maxsorb III for different adsorption capacities. They also presented the thermodynamic property maps as a function of pressure, temperature and adsorption capacity. Moreover, a review of the types, characteristics, advantages and disadvantages of different adsorbents, refrigerants and working pairs together with their models are presented by Wang et al. [25].

1.4.2 Thermal powered adsorption cooling (TPAC) systems

Over the past several decades, various types of adsorption cooling systems using different adsorbent-refrigerant pairs have been designed, built, and tested, such as exhaust gas-driven adsorption air conditioners [26–28], exhaust gas-driven adsorption ice makers [22,29], solar-powered adsorption air conditioners [30–33], and solar-powered adsorption ice makers [34–36]. The specifics of some of these systems at base conditions have been presented in Table 1.2. These systems have used a variety of adsorbent-refrigerant pairs, including zeolite 13x-water, silica gel-water, silica gel-methanol, activated carbon-methanol and activated carbon-ammonia. Zeolite is a mineral available naturally and in synthetic forms. Most zeolites are environmentally benign, do not deteriorate with age or use, and are suitable for reversible adsorption processes. In addition, they have a strong affinity for water relative to other possible refrigerants and unlike many other refrigerants water is environmentally benign, non-flammable, and non-toxic. Due to the large natural zeolites resources indigenous to Turkey, the Turkish EIE (General Directorate of Electrical Power Resources Survey and Development Administration) is specifically interested in developing adsorption heat pumps using natural zeolite as the adsorbent and hence, natural zeolite-water was chosen as the adsorbent-adsorbate working pair for this research.

1.4.3 Dynamic heat and mass transfer behavior of the adsorbent beds

The successful operation of a TPAC system depends strongly on the performance of its adsorbent bed filled with a porous material. The performance of an adsorbent bed is affected adversely by the heat and mass transfer limitations inside the bed, such as poor thermal conductivity of the solid adsorbent, and internal (intraparticle) and external (interparticle) mass transfer resistances. The internal and external mass transfer resistances are generally considered for the respective adsorbate gas flows inside the solid adsorbent particle and through the voids between the solid adsorbent particles. Therefore, many attempts have been made to improve the heat and mass transfer characteristics of the adsorbent beds for a TPAC system. However, reducing heat transfer resistances inside a bed tends to increase the mass transfer resistances and vice versa. Therefore, heat and mass transfer conditions inside the adsorbent bed need to be understood well to design a high performance adsorbent bed.

Table 1.2: The specifics of some of the adsorption cooling systems at base conditions.

Ref.	Working pair	Driven by	Type	COP	SCP (Wkg^{-1})	t_{cy} (s)	Q_{refr} (kW)	SCP_v (kWm^{-3})
[27]	Zeolite13x-water	Exhaust gas	AC	0.38	25.7			
[26]	Zeolite13x-water	Exhaust gas	AC	0.152			3.2	
[22]	Activated carbon-methanol	Exhaust gas	Refr.	0.125	32.6	3960		9.3
	Composite adsorbent-ammonia	Exhaust gas	Refr.	0.35	493.2	3600		52.7
[29]	Activated carbon-methanol	Waste heat	Refr.	0.13	2.6 kg$_{\text{ice}}$	6000		
			AC	0.4	150		3000	
[32]	Silica gel-water	Solar-Waste heat	AC	0.36		440	3.2	
[33]	Silica gel-water	Solar-Waste heat	AC	0.371	63.4	900	6.6	
[34]	Activated carbon-methanol	Solar energy	Refr.	0.12/0.14			5.6 kg$_{\text{ice}}$	

Over the past several decades, many researchers have proposed various mathematical models to investigate the heat or coupled heat and mass transfer mechanism inside the adsorbent beds of TPAC systems [37–48]. These models are summarized in Table 1.3 in terms of their important characteristics and their most important characteristics in terms of the present research are as follows. The equations have been developed for the heat transfer within a porous medium typically assuming a mobile gas (vapor) phase, an immobile solid phase (adsorbed adsorbate + adsorbent), and local thermal equilibrium (LTE) between the gas and solid phases; the sole exception is the paper by Mhimid [39]. LTE is based on the assumption that the temperature of the gas and solid phases are the same and thus, a single temperature suffices to describe the heat transport process. However, this assumption is no longer valid if the following conditions are in existence [58]

- the particles or pores are not sufficiently small
- the thermal properties differ widely or convective transport is important
- there is a significant heat generation in any of the phases

and thus, an energy equation for each phase needs to be developed, i.e. Local Thermal Non-Equilibrium (LTNE).

In the proposed conservation of mass equations, the mass transfer resistance within the solid adsorbent particles was typically accounted for and the internal mass transfer rate between the solid adsorbent and adsorbate gas phases (including sorption processes) was predicted using the solid diffusion (SD) [45] or liner driving force (LDF) model [37–48]. Solid diffusion model is obtained from the Fick's law and defined as follow;

$$\frac{\partial X}{\partial t} = \frac{D_s}{r^2}\frac{\partial}{\partial r}\left(r^2\frac{\partial X}{\partial r}\right) \tag{1.1}$$

The LDF model, widely used because of its simplicity and accuracy, is derived from the solid diffusion model using a simplifying mathematical assumption that is the concentration profile within the particle is parabolic and thus, it has a restricted domain of validity and is given as follow [45].

Table 1.3: Classification of the existing mathematical models in terms of their most important characteristics.

Ref.	Dimension	Internal Mass Transfer Resistance Model	External Mass Transfer Resistance Model	Energy Equation
[41, 42, 44]	3D	LDF	Darcy’s equation	LTE
[37, 45]	1D	LDF	Uniform pressure	LTE
[37, 45]	1D	SD	Uniform pressure	LTE
[37, 45, 49]	1D	Adsorption equilibrium	Uniform pressure	LTE
[40, 43, 50–52]	2D	LDF	Darcy’s equation	LTE
[46, 47]	2D	Adsorption equilibrium	Ergun’s equation	LTE
[48]	2D	LDF	Uniform pressure	LTE
[54]	Lumped	LDF	Uniform pressure	LTE
[39, 55]	2D	LDF	Darcy’s equation	LTE and LTNE
[53, 56]	2D	Adsorption equilibrium	Uniform pressure	LTE
[57]	1D	Adsorption equilibrium	Darcy’s equation	LTE
[38]	1D	LDF	Darcy’s equation	LTE

$$\frac{\partial X}{\partial t} = k_m \left(X_\infty - X \right) \tag{1.2}$$

Occasionally, resistance to this type of flow is neglected and adsorption equilibrium is assumed [45]. In the equilibrium model, internal mass transfer (adsorption) is assumed to be sufficiently rapid and hence, concentration gradients in the solid adsorbent particles do not exist. In this case, the adsorption rate is only related to adsorbate gas pressure and adsorbent temperature. This assumption is reasonably good for adsorbent particles with small diameters.

Darcy's law described in Equation 1.3 has been used widely to account for the external mass transfer through the voids between the solid adsorbent particles by convection, instead of using the Navier-Stokes equations [38–44]. Darcy's law is one of the forms of the momentum equation which is the porous medium analog of the Navier-Stokes equations [59] and it is only applicable for the incompressible and isothermal creeping flow (very low speed) of Newtonian fluid through a relatively long, uniform and isotropic porous medium of low hydraulic conductivity [60].

$$v = -\frac{K_d}{\mu_g} \nabla P \tag{1.3}$$

where, the real permeability K_d is generally a second-order tensor but for an isotropic medium, it is a scalar.

Additionally, in two instances the adsorbate gas velocity through the adsorbent bed was determined using Ergun's equation which includes inertial effects [46, 47] and it is defined as follow.

$$v + \frac{\rho_g}{\mu_g} K_E v \left| v \right| = -\frac{K_a}{\mu_g} \nabla P \tag{1.4}$$

Blake-Kozeny model which obeys Darcy's law can be apply for Reynolds number less than ten but inertial effects must be included for higher Reynolds numbers. The Ergun's equation combines the low Reynolds number Blake-Kozeny model with the high Reynolds number Burke-Plummer model and it works for both regimes [61].

On the other hand, in some previous studies, the pressure across the bed was assumed to be uniform as a result of a high permeability within the bed or the use of a high working-pressure refrigerant like ammonia. This means that the external mass transfer resistances in the adsorbent bed were neglected [37,45,48].

These previous studies shows that even though the performance of TPAC units have been widely studied for different design parameters and operating conditions [37,40–54], little attention has been focused on investigating the transient heat and mass transfer behavior of the adsorbent bed of the TPAC units [38, 39, 55–57]. Mhimid [39] studied the heat and mass transfer in a zeolite bed during water desorption using the LTE and LTNE models and the results showed that the LTE assumption is not valid in regions with high rates of heat transfer (at the wall where external heating occurs, in the region where the vaporization takes place). Jemni and Nasrallah [55] investigated transient heat and mass transfer in a metal-hydrogen reactor and they concluded that the LTE model is not valid in the whole reactor. Guilleminot and Meunier [56] investigated numerically and experimentally heat and mass transfer in a non-isothermal fixed bed solid adsorbent reactor and they concluded that the uniform pressure model is more realistic than the uniform temperature models proposed previously. Yong and Sumathy [57] compared heat transfer only and combined heat and mass transfer models for transport processes in an adsorbent bed and they proposed two general criteria to perform an order of magnitude analysis to determine when the simpler heat transfer only model is appropriate. Demir et.al. [38] performed a numerical study to investigate the effects of porosity on heat and mass transfer in a granular adsorbent bed and they found that the distributions of temperature and adsorbate concentration are strongly influenced by the bed porosity.

1.5 SCOPE OF THE WORK

In this thesis, the equilibrium adsorption capacity of water on natural zeolite at several zeolite temperatures and refrigerant pressures for adsorption and desorption processes has been investigated experimentally in Chapter 2. The modified Dubinin-Astakhov (D-A) equation is used to correlate the equilibrium data of the adsorption and desorption experiments in this Chapter as well. In Chapter 3, a thermally driven adsorption cooling unit using natural zeolite-water as the adsorbent-refrigerant pair has been built and the performance of the cooling unit at various evaporator temperatures has been investigated. To investigate the dynamic heat and mass transfer behavior of the adsorbent bed of an adsorption cooling unit, a transient one and two dimensional local thermal non equilibrium model that accounts for both internal and external mass transfer resistances have been developed using the local volume averaging method in Chapter 4. The influence of several design parameters on the transient distributions of temperature, pressure and amount adsorbed in the cylindrical adsorbent bed of a solid sorption cooling unit using silica-gel/water as working pair have been investigated numerically in Chapter 5 and 6 for the 1D and 2D computational domain, respectively. Additionally, validity of the thermal equilibrium model assumption has been shown under the given boundary and design conditions. Finally, results obtained from the numerical and experimental studies have been summarized in Chapter 7.

CHAPTER 2

ADSORPTION PROPERTIES OF A NATURAL ZEOLITE-WATER PAIR FOR USE IN ADSORPTION COOLING CYCLES

2.1 INTRODUCTION

One of the objectives of this thesis is to develop and assess the commercial feasibility of a solar-thermal driven adsorption cooling system using natural zeolite-water as the adsorbent-refrigerant pair. For this purpose, the equilibrium adsorption capacity of water on natural zeolite at several zeolite temperatures and refrigerant pressures for adsorption and desorption processes has been investigated experimentally. In addition, the modified Dubinin-Astakhov ("D-A") equation is used to correlate the equilibrium data of the adsorption and desorption experiments. The isosteric heat of adsorption of natural zeolite-water pair as a function of equilibrium adsorption capacity is calculated by using the Clausius-Clapeyron equation. Furthermore, the cyclic swing in adsorption capacities of natural zeolite-water for different condenser, evaporator and adsorbent temperatures is compared to that for select alternate working pairs including activated carbon-methanol, silica gel-water and zeolite 13X-water.

This chapter is mainly based on the publication "Solmuş İ., Yamalı C., Kaftanoğlu B., Baker D., Çağlar A., Adsorption properties of a natural zeolite-water pair for use in adsorption cooling cycles. Applied Energy 87 (2010) 2062-2067."

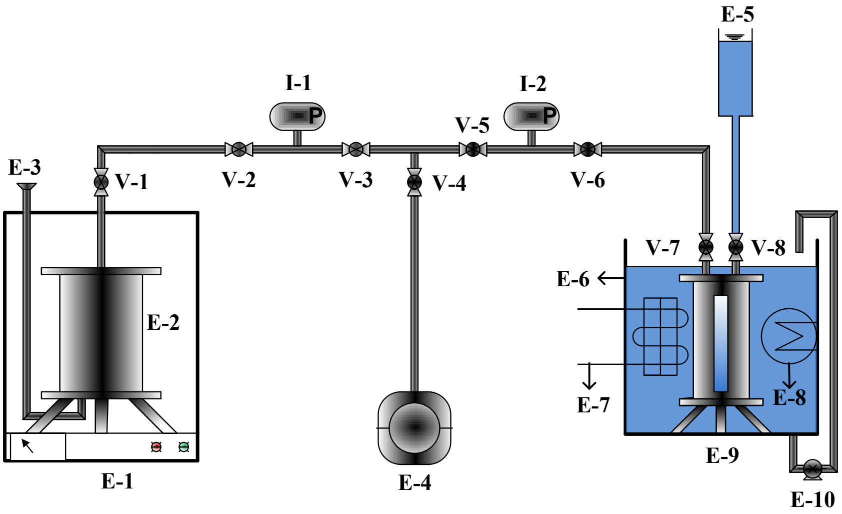

Figure 2.1: A schematic view of the experimental set-up (E-1 Oven; E-2 Zeolite canister; E-3 Thermocouple output; E-4 Vacuum pump; E-5 Feed water; E-6 Water bath; E-7 V-C cooling system; E-8 Electrical heater; E-9 Evaporator/Condenser ; E-10 Circulation pump; V-1 … 8 Vacuum valves; I-1,2 Pressure transducers).

2.2 DESCRIPTION OF THE EXPERIMENTAL SET-UP

An experimental apparatus has been designed and constructed to obtain the equilibrium adsorption capacity of a natural zeolite mined in Turkey. A schematic and photograph of the experimental apparatus are shown in Figure 2.1 and Figure 2.2, respectively. The main components of the experimental apparatus are as follows: zeolite canister; combination evaporator/condenser; water bath; oven; vacuum pump; piping system; and data acquisition and control (DAQ) system. Detailed descriptions of these main components are as follows.

2.2.1 Zeolite Canister

In Figure 2.3 a photograph of the stainless steel zeolite canister (adsorber bed) and its components are presented. The zeolite canister consists of a 140 mm diameter and 250 mm long tube with top and bottom covers and is filled approximately 3/5 full of zeolite with the remaining top 2/5 being a vapor gap. The canister is heated and cooled by the heat transfer fluid through the outer shell. Zeolite is a relatively poor thermal conductor and the zeolite used in these experiments consists of small grains (approximately 0.5 mm), which when packed

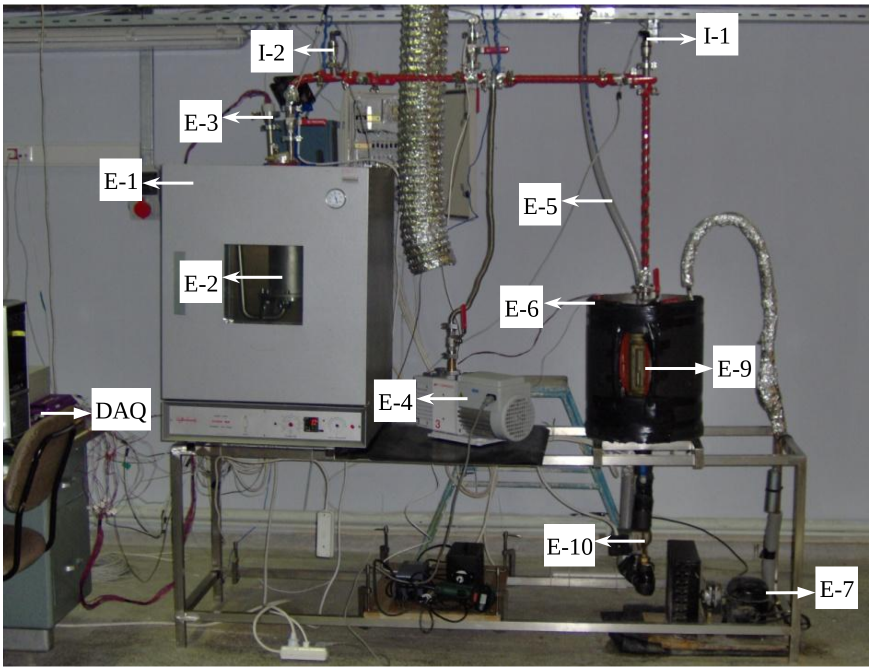

Figure 2.2: A photograph of the experimental set-up (E-1 Oven; E-2 Zeolite canister; E-3 Thermocouple output; E-4 Vacuum pump; E-5 Feed water; E-6 Water bath; E-7 V-C cooling system; E-9 Evaporator/Condenser ; E-10 Circulation pump; I-1,2 Pressure transducers).

together results in large contact resistances. To enhance heat transfer rates, and therefore reduce the thermal response time, 8 heat transfer fins and a compression plate are used. The fins are 5 mm thick, 65 mm wide and 150 mm long and mounted in the axial plane inside the outer shell. Due to space limitations, only four of these fins could be welded directly to the inside of the outer shell, while the remaining four were welded onto the bottom cover. The compression plate is a spring loaded stainless steel disk that is used to separate the zeolite from the 100 mm vapor gap and to slightly compress the zeolite and decrease thermal contact resistances. Refrigerant vapor enters and leaves the zeolite canister through the top cover by passing through the vapor gap. To enhance mass transfer between the vapor gap and the packed zeolite, tightly spaced 3 mm mass transfer holes were drilled throughout the compression plate. Mass transfer to the lower levels of zeolite is enhanced through mass transfer tubes. Each mass transfer tube has a 10 mm diameter and is 167 mm in height. One end is welded to the bottom cover of the zeolite canister while the other end passes through holes in the compression plate and opens to the vapor gap. Numerous 3 mm mass transfer holes were drilled throughout the mass transfer tubes, allowing refrigerant vapor to pass from the vapor

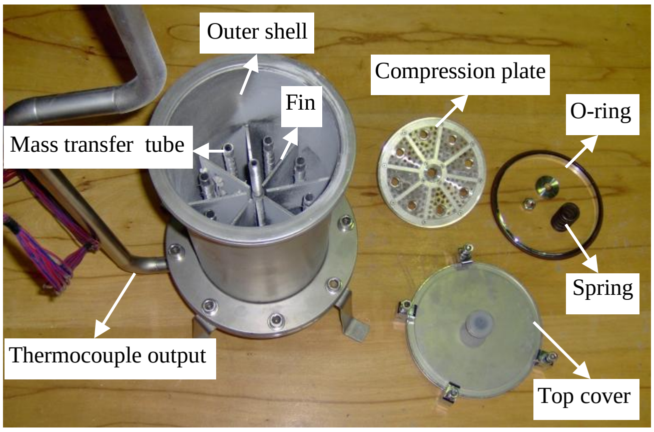

Figure 2.3: A photograph of the stainless steel zeolite canister and its components.

gap, down the inside of the mass transfer tubes, and then through the holes to the zeolite. To prevent the zeolite from passing through the small mass transfer holes in the compression plate and mass transfer tubes, a fine stainless mesh is used. The total interior volume of the canister is 2.25 liters and it holds approximately 1.68 kg of zeolite. Twelve thermocouples are distributed in a single axial plane to obtain the temperature distribution inside the adsorber bed, with 3 thermocouples at radii of 24, 46 and 68 mm from the center of the zeolite canister placed at approximately 17, 57, 97, and 135 mm from the bottom of the canister. The zeolite canister is put inside the oven and the oven is used to control the zeolite's temperature.

2.2.2 Evaporator/Condenser

The evaporator/condenser (water canister) consists of an 80 mm inner diameter stainless steel tube that is 200 mm long, with top and bottom covers. Glass covers a 30 mm wide slot cut axially through one side of the cylinder and allows the height of liquid water inside the water canister to be measured. The change in the height of liquid water indicates the change in mass of liquid water inside the evaporator/condenser, and therefore the change in water adsorbed on the zeolite. Two thermocouples are inserted in the evaporator/condenser to measure the liquid and vapor temperatures. The interior volume of the evaporator is 0.88 liters and it is submersed in a temperature controlled water bath.

2.2.3 Water Bath and Oven

The water bath for the evaporator/condenser contains three 1.5 kW electrical heaters, an evaporator coil of a vapor compression cooling system, and a water circulation pump. By varying the temperature of the water bath, the vapor pressure inside the zeolite canister is controlled. The electrically heated oven in which the zeolite canister is placed has an air blower to enhance heat transfer between the oven air and the zeolite canister. Two thermocouples measure and control the temperatures of the water bath and oven.

2.2.4 Piping System

A piping system connects the zeolite canister to the evaporator/condenser. A two-stage Edwards RV-3 rotary vane vacuum pump is used to initially evacuate the system before introducing the refrigerant (water) into the system. Note that condensation will occur on any surface exposed to the water vapor and at a lower temperature than the saturated water in the evaporator/condenser. Therefore, the whole piping system is maintained at an elevated temperature by wrapping the pipes with electrical heater tape.

2.2.5 Data Acquisition and Control System

The data acquisition and control (DAQ) system is a Datataker-DT800 that is used to measure and record all thermocouple and pressure gage measurements. The software DeLogger is used to program the Datataker-DT800 and download and visualize the data. The computer is connected to the Datataker with the COMM cable. The vapor pressure inside the system is measured with two Edwards ASG1000 pressure gages. The temperatures in the zeolite canister, evaporator/condenser, oven and water bath are measured using T-type thermocouples connected to the DT800. The data are collected every 5 seconds and stored on the computer's hard disk.

Table 2.1: Thermo physical properties of natural zeolite.

Appearance	Ivory white
Porosity	0.45-0.5
Average pore diameter (A)	4
pH	7-8
Bulk density (kg/m^3)	650-850
Melting temperature (°C)	1300
Mesopore surface area (m^2/gr)	29
Micropore surface area (m^2/gr)	11
Thermal conductivity (W/m^{2}K)	0.155

2.3 EXPERIMENTAL PROCEDURE

The goal for the experimental procedure is to obtain adsorption data relating the equilibrium adsorption capacity of the zeolite to the zeolite's temperature and the refrigerant's vapor pressure. These data are important as they define the thermodynamic operation of an ideal cycle and therefore set limits with respect to performance and system size. Natural zeolite (88-95 % klinoptilolit) with 0.5 mm grain size supplied by the ROTA mining company was used in these experiments and its thermophysical properties are presented in Table 2.1. The experimental study can be divided into two steps. In the first step the zeolite is prepared and in the second step the adsorption data are obtained.

2.3.1 Zeolite Preparation

The zeolite undergoes several processes before it is poured into the zeolite canister. First, the zeolite is sifted using a micro size screen to remove fine particles. Then, it is washed using de-ionized water. The washed zeolite is spread over a clean surface and allowed to air dry for 24 hours and then is further dried inside an oven at 200 °C. The mass of the zeolite in the oven is measured every 30 minutes during the drying process. Once the difference between two successive measurements is less than 1 gr (0.06 % of the total mass), this process is ended.

2.3.2 Isotherm Experiments

Equilibrium adsorption data are obtained at several zeolite temperatures and refrigerant pressures. While holding the zeolite temperature constant at 150 °C, adsorption data are obtained for refrigerant pressure corresponding to water bath temperatures of approximately 5, 10, 20, 30 and 40 °C. This process is repeated for oven temperatures of 125, 100, 75 and 40 °C.

A known mass and volume of zeolite prepared according to the procedure above is poured into the zeolite canister and the zeolite canister is sealed. This canister is put inside the oven and attached to the rest of the experimental apparatus. The valves (V-5) and (V-8) in Figure 2.1 are closed and the others were kept open. The oven temperature is set to 150 °C, and the vacuum pump is turned on. The zeolite canister is evacuated until the pressure inside the zeolite canister is less than 0.1 kPa. After the end of this process, the valve (V-3) is closed and the valve (V-5) is opened, and the rest of the system is completely evacuated. After the residual gas pressure inside the system is measured to be less than approximately 0.1 kPa the system is assumed to be evacuated. Subsequently, the valve (V-4) is closed and the vacuum pump is turned off. The water bath temperature is set to 5 °C and the valve (V-5) is closed before introducing the de-ionized water into the evaporator/condenser. The water intake valve (V-8) is then slowly cracked and water is allowed to flow into the evaporator/condenser. The mass of water brought into the system is calculated based on the measured liquid volume in the condenser/evaporator, while the mass of water in the vapor phase is neglected. The pressure in the evaporator/condenser is compared with the water's saturation pressure at the bath temperature. If the measured and saturation pressure differ by more than 0.3 kPa, the vacuum pump is turned on and valves (V-4 and V-5) are opened. Once the measured and saturation pressures are approximately equal, the valve (V-4) is closed and vacuum pump is turned off. The mass of the water vapor pumped out of the system during this process is assumed negligible. Finally, valve (V-3) is slowly cracked allowing water vapor to flow from the evaporator/condenser to the zeolite canister. Some of this water vapor is then adsorbed on the zeolite, releasing its heat of adsorption and causing the zeolite to warm slightly. The valves (V-1 and V-7) are closed when the system reaches thermodynamic equilibrium as defined below. The mass of water adsorbed is assumed to be proportional to the decrease in liquid water in the condenser/evaporator, which is recorded with the temperatures of the water bath and oven and the refrigerant pressure. The relaxation time for the zeolite canister is assumed to be limited by thermal and not mass resistances; i.e., the effects of pressure gradients are assumed negligible relative to temperature gradients. Temperature gradients develop inside the zeolite canister due to both heat exchanges with the oven air through the canister's walls and heat of adsorption being released/adsorbed with the sorption processes. Therefore the zeolite canister is assumed to reach thermodynamic equilibrium when all the thermocouples inside the canister are within 5 °C of the oven temperature. The evaporator/condenser has two thermocouples, one that measures the liquid and the other that measures the vapor temperature. The temperature indicated by the thermocouple that measures the vapor temperature is sensitive to evaporation and condensation processes, and therefore when the temperatures indicated by these two thermocouples are within 1 °C of one another the evaporator/condenser is assumed to reach equilibrium. A final check for system equilibrium is that the vapor pressure needs to stabilize. This process is repeated at decreasing zeolite temperatures and increasing refrigerant pressures such that refrigerant is adsorbed between each equilibrium state. After a complete set of data is obtained, the same set of zeolite temperatures and refrigerant pressures are revisited in the reverse direction such that desorption occurs between each equilibrium state to check for both repeatability and hysteresis.

2.4 RESULTS

2.4.1 Adsorption Equilibrium

The equilibrium adsorption capacity (X) of the adsorbent-refrigerant working pair varies with the adsorption pressure (P_v) and adsorbent temperature (T_{ad}); i.e., $X = f\,(P_v, T_{ad})$. The equilibrium adsorption capacity of the natural zeolite for adsorption/desorption processes have been measured at zeolite temperatures from 40 to 150 °C and equilibrium pressures from 0.87 to 7.38 kPa. Equilibrium pressure is the saturated pressure of the refrigerant (water) corresponding to the saturated refrigerant liquid temperature.

Evaluating and predicting the performance of an adsorption cooling system is facilitated by correlating the experimental data with an adsorption equilibrium model as a function of pressure and temperature. In the present study, the modified Dubinin-Astakhov equation (Equation 2.1) is used to correlate the experimental data [22], because the D-A equation is exten-

Table 2.2: Constants for the D-A equation for adsorption, desorption, and average models.

	x_o	k	n
Adsorption	0.1219	5.052	1.4
Desorption	0.1249	3.62	1.2
Average	0.1233	4.268	1.3

sively used to represent the experimental data that belongs to heterogeneous adsorbents, like natural zeolite [24].

$$X = x_o \exp\left[-kA\right] \tag{2.1}$$

where, A is defined by the following equation

$$A = (T_{ad}/T_{sat} - 1)^n \tag{2.2}$$

Where X is the refrigerant adsorbed ($\mathrm{kg_w/kg_{ad}}$), T_{ad} is the adsorbent temperature (K), T_{sat} is the saturation temperature of the refrigerant (K), and k, x_o and n are experimental constants used to fit the equation to the experimental data. Using the experimental X, T_{ad}, and T_{sat} data sets, the D-A equation was fitted to only the adsorption data, only the desorption data, and all the sorption data (adsorption + desorption) to yield k, x_o and n values for three types of adsorption capacity models: adsorption, desorption, and average. Any differences in the adsorption and desorption data is due to hysteresis. To fit the D-A equation to the appropriate data, a value of n in Equation 2.2 is assumed and A is calculated for each X, T_{ad} and T_{sat} data set. The MatLab Curve Fitting toolbox is used to determine the values of k, x_o that best fit Equation 2.1 to the X and A data sets. The assumed value of n is iterated upon and the procedure repeated until a sufficiently good fit is obtained. Numerical values of the experimental constants corresponding to the best fits for adsorption, desorption and average models are presented in Table 2.2.

The equilibrium adsorption capacity of the zeolite-water pair for adsorption and desorption

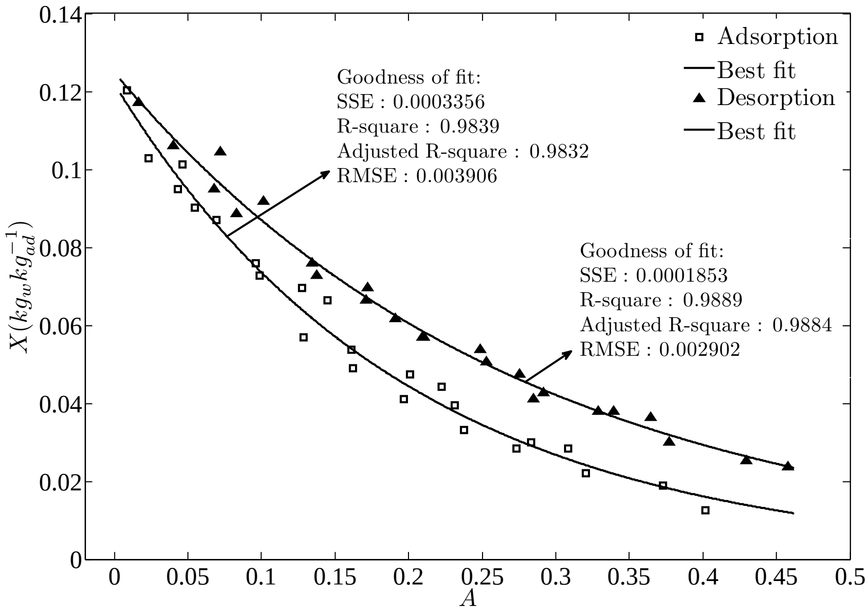

Figure 2.4: Goodness of fit of the adsorption and desorption models.

process versus *A* are shown in Figure 2.4. In this figure, experimental data points for adsorption and desorption processes are shown using rectangular and triangle symbols, respectively, and the solid lines show the best fit to the experimental data. As indicated above, to get the best fit to the adsorption and desorption experimental data, different *n* values for adsorption and desorption process are used and thus, the different *n* values for both processes indicates that there is a hysteresis effect. Figure 2.4 also shows that within the range of adsorbent temperatures and adsorption pressures explored, the maximum adsorption capacity of the natural zeolite-water working pair is nearly 12 %. As expected, the amount of water that is adsorbed by the adsorbent material increases with increasing refrigerant pressure and decreasing adsorbent temperature. However, the adsorption capacity of the adsorbent material is a weak function of the refrigerant pressure at high adsorbent temperatures.

Figure 2.5 shows the equilibrium adsorption capacity data for the average (adsorption or desorption) process versus *A*. Although the adsorption and desorption experimental data can be represented by a single D-A equation, the goodness of fit decreases relative to using separate adsorption and desorption models.

When the equilibrium adsorption capacities measured for adsorption and desorption processes are compared at low adsorbent temperatures, little hysteresis is found. However, the hysteresis

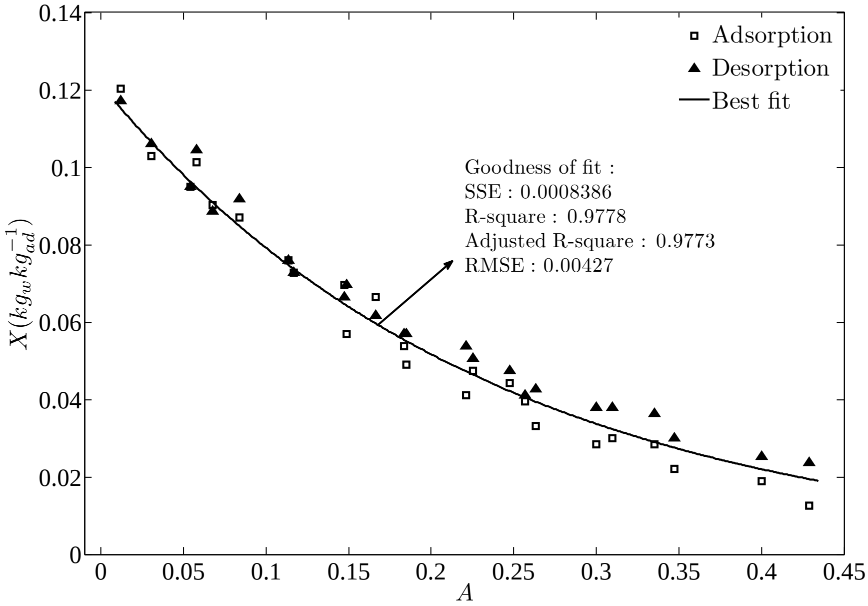

Figure 2.5: Goodness of fit of the average model.

increases with increasing adsorbent temperature. The reasons behind the increasing hysteresis can be explained as follows:

- If the condensation surface area in the condenser/evaporator is not large enough, at low refrigerant pressures the condensation process takes a long time to reach equilibrium conditions. Additionally, the presence of the non-condensible gases on condensation surfaces adversely affects the condensation rate.
- The experiment at any given conditions was probably terminated before equilibrium was reached in the condenser/evaporator. Consequently, the adsorption capacity measured during desorption process is higher than the true equilibrium adsorption capacity.
- Equilibrium adsorption capacity decreases with an increasing adsorbent temperature. Thus, at low adsorption capacities, the error in reading the level of condensate becomes larger since the amount of condensate level change is small.

The cyclic adsorption capacity swings calculated using the adsorption and desorption D-A equations, and using the average D-A equations for different condenser temperatures are shown in Figure 2.6 as a function of adsorbent temperature. The maximum adsorption capacities are evaluated at an adsorbent temperature of 40 °C. It can be seen from the figure that

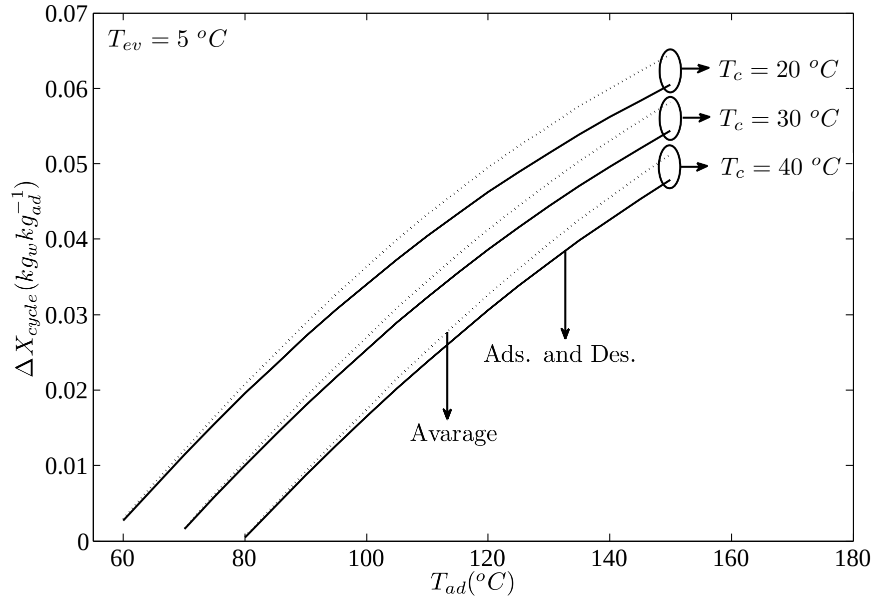

Figure 2.6: Cyclic adsorption capacity swing as a function of adsorbent temperature for various condenser temperatures.

the differences in the cyclic adsorption capacity swing between the adsorption and desorption versus average D-A equations for different condenser temperatures increases with increasing adsorbent temperature and this difference is almost the same for all condenser temperatures at different adsorbent temperatures.

In conclusion, for adsorption, desorption and average sorption processes, the adsorption capacity of the natural zeolite-water working pair can be calculated numerically with the aid of the D-A equation by using the adsorbent temperature and saturation temperature of refrigerant. Note, however, that the experimental conditions to which these equations were fitted were for adsorption temperatures and refrigerant pressures ranges of 40-150 °C and 0.87-7.38 kPa, respectively. Therefore, these equations will likely not be accurate at predicting adsorption capacities outside this range.

2.4.2 Heat of Adsorption

The isosteric heat of adsorption for water on natural zeolite as a function of equilibrium adsorption capacity shown in Figure 2.7 is calculated by the Clausius-Clapeyron equation as follows.

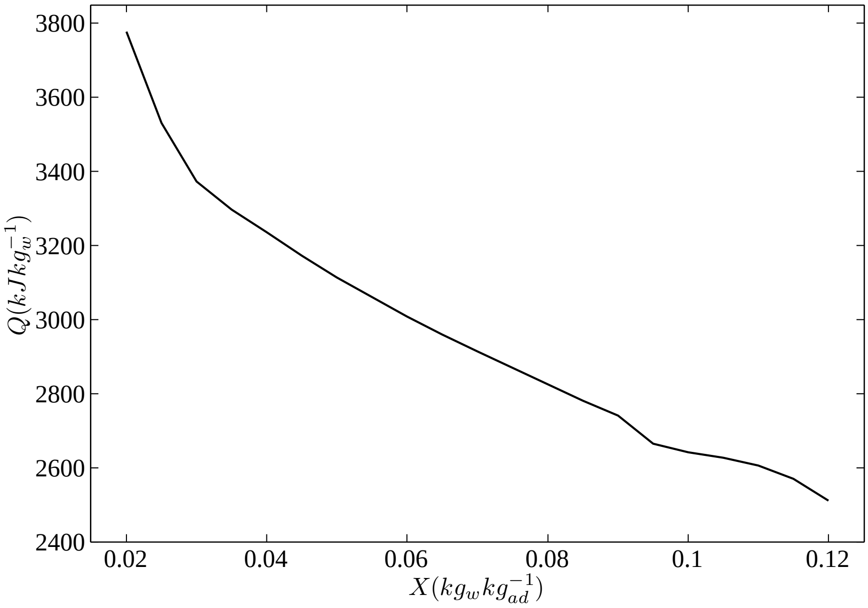

Figure 2.7: The isosteric heat of adsorption for water on natural zeolite as a function of equilibrium adsorption capacity.

$$\left(\frac{\delta \ln P_v}{\delta (1/T_{ad})}\right)_X = -\frac{Q_{ad}}{R} \tag{2.3}$$

In Equation 2.3, X is the adsorption capacity ($\mathrm{kg_w/kg_{ad}}$), T_{ad} is adsorption temperature (K), P_v is the refrigerant pressure (Pa), Q is the isosteric heat of adsorption ($\mathrm{kJ/kg_w}$), and R is the specific gas constant for water (kJ/kgK).

In Equation 2.1 and with the constants in Table 2.2, the variation of $\ln P_v$ with $1/T_{ad}$ at constant X is almost linear and this variation can be represented by the following relation.

$$\ln P_v = a + \frac{b}{T_{ad}} \tag{2.4}$$

As can be deduced from Equation 2.4, the isosteric heat of adsorption at any given X can be calculated by multiplying b in Equation 2.4 with (-R).

It is clear in Figure 2.7 that the isosteric heat of adsorption decreases with increasing adsorption capacity. The reason behind this behavior is clearly explained by B. B Saha et.al. [24] for Maxsorb III-n-butane pair by considering the mechanism of the diffusion of refrigerant into the pores of the adsorbent. Additionally, there are some jumps in a curve presented in Figure 2.7 and they can be eliminated if the isosteric heat of adsorption is calculated for a small increment of X.

2.4.3 Comparison of Different Adsorbent-Refrigerant Working Pairs

The design and performance analysis of the adsorption cooling system can be accomplished with knowledge of the cyclic adsorption capacity swing of the adsorption working pair used in the system at different conditions. For this reason, the cyclic adsorption capacity swings of the adsorbent-refrigerant working pairs natural zeolite-water, activated carbon-methanol, silica gel-water and zeolite13X- water at different condenser, evaporator and adsorbent temperatures are presented.

The adsorption capacity of activated carbon-methanol, silica gel-water and zeolite 13X- water at various equilibrium conditions are calculated using Equations 2.5-2.7, respectively [25]. The adsorption capacity of the natural zeolite-water pair is calculated by using the modified D-A equation with the coefficients given in Table 2.2 for adsorption and desorption processes. For all these pairs, the maximum adsorption capacity is evaluated at 40 °C adsorbent bed temperature.

$$X = 0.45 \exp\left[-13.38\left(\frac{T_{ad}}{T_{sat}} - 1\right)^{1.5}\right] \tag{2.5}$$

$$X = 0.35 \exp\left[-6.10^{-6}\left(T \ln \frac{P}{P_{sat}}\right)^{1.7}\right] \tag{2.6}$$

$$X = 0.261 \exp\left[-5.36\left(\frac{T_{ad}}{T_{sat}} - 1\right)^{1.73}\right] \tag{2.7}$$

Figure 2.8 shows the cyclic adsorption capacities swings of activated carbon-methanol (A), silica gel-water (B), zeolite 13X- water (C) and natural zeolite-water (D) at evaporator temperatures of 15 °C, 10 °C and 5 °C, respectively. The cyclic adsorption capacity swing of

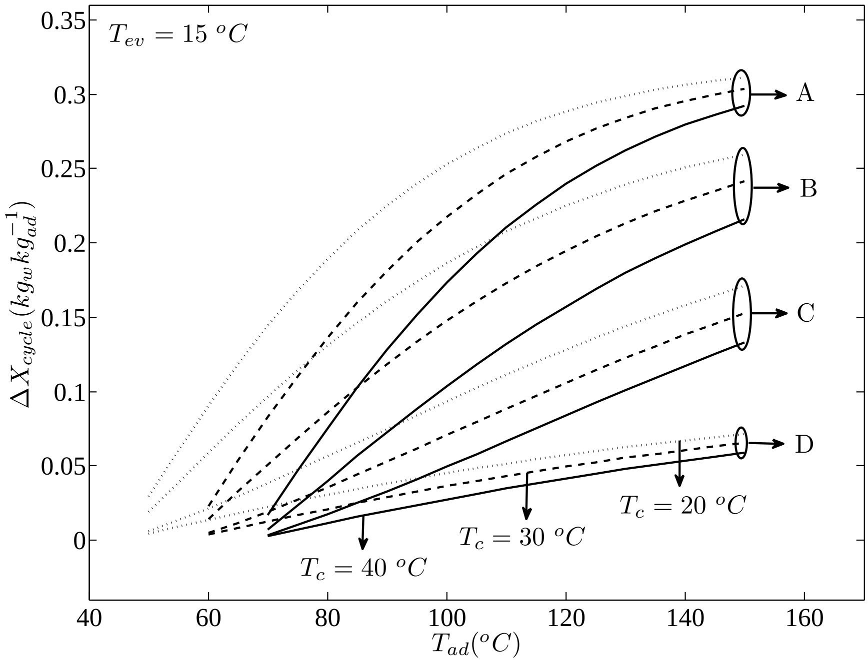

(a) $T_{ev} = 15\,°\mathrm{C}$

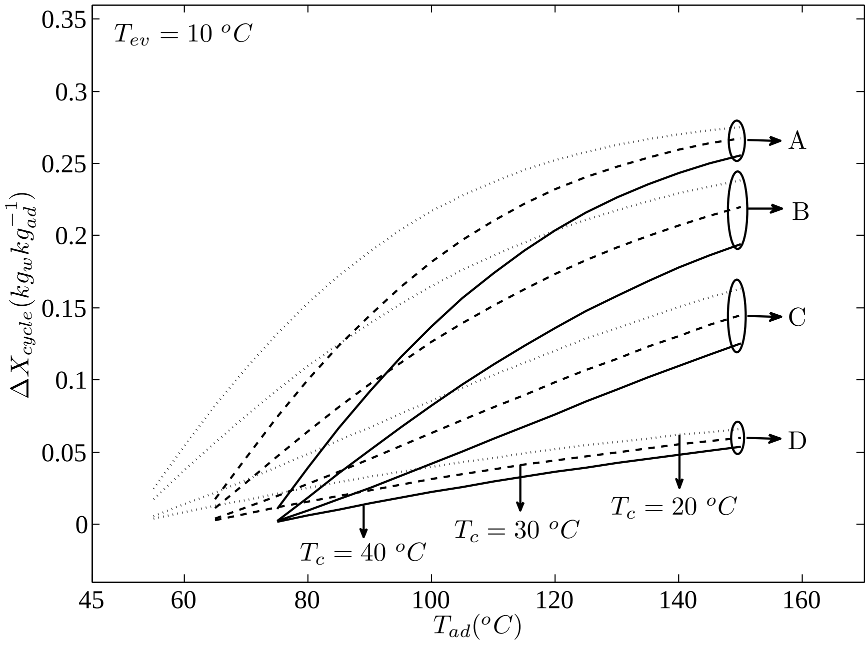

(b) $T_{ev} = 10\,°\mathrm{C}$

Figure 2.8: Cyclic adsorption capacities of adsorbent-refrigerant working pairs (A = Activated Carbon-Methanol; B = Silica gel-Water; C= Zeolite13X-Water; D= Natural zeolite-Water).

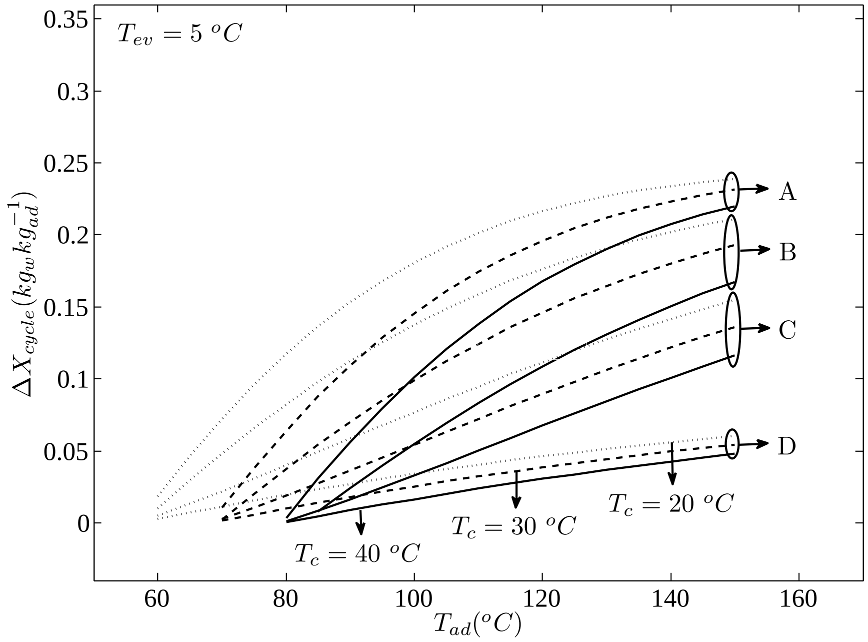

(b) $T_{ev} = 5\,^\circ$C

Figure 2.8: Cyclic adsorption capacities of adsorbent-refrigerant working pairs (A = Activated Carbon-Methanol; B = Silica gel-Water; C= Zeolite13X-Water; D= Natural zeolite-Water)(cont).

the adsorbent-refrigerant working pairs investigated increases with increasing of evaporator and regeneration temperatures and with a decreasing condenser temperature. The activated carbon-methanol pair has higher cyclic adsorption capacity swings than the other pairs at the same working conditions and the natural zeolite-water pair has the lowest cyclic adsorption capacity swing. Regeneration temperatures of the activated carbon-methanol and silica gel-water are lower than that of the natural zeolite-water and zeolite 13X- water pairs, since the cyclic adsorption capacity swings of these pairs is increases little for regeneration temperature increases above 140 °C. However, for natural zeolite-water and zeolite13X- water pairs, the cyclic adsorption capacity swing increases with increasing regeneration temperature. The cyclic adsorption capacity swing of the natural zeolite-water and zeolite 13X-water is not affected considerably by changing the evaporator temperature but the other pairs are, especially for activated carbon-methanol. Also, the cyclic adsorption capacity swing of the activated carbon-methanol, silica gel-water is very sensitive to the variation of the condenser temperatures.

2.4.4 Uncertainty Analysis

The experimental uncertainties related to adsorption capacities were calculated by using the Gauss' error propagation law. According to this law, if a result R is to be calculated by a function $R = f(x_1, x_2, x_3 \ldots x_n)$ from a single set of values of the input data x_n, then the uncertainty in R is given by:

$$w_R = \left[\left(\frac{\delta R}{\delta x_1} w_1 \right)^2 + \left(\frac{\delta R}{\delta x_2} w_2 \right)^2 + \ldots + \left(\frac{\delta R}{\delta x_n} w_n \right)^2 \right]^{0.5} \tag{2.8}$$

where, w_n denotes the uncertainty in the nth independent variable.

The adsorption capacity of water on a natural zeolite for adsorption/desorption processes were calculated using the following equation corresponding to R in Gauss' error propagation law.

$$X = \frac{\rho_w \left(x_{e1} - x_{e2}\right) \left[\left(v_{c2} - v_{c1}\right) / \left(x_{c2} - x_{c1}\right)\right]}{m_{ad}} \frac{1}{10^6} \tag{2.9}$$

In the equation above, the terms $(v_{c2} - v_{c1}) / (x_{c2} - x_{c1})$ and $(x_{e1} - x_{e2})$ correspond to calibration constant of the evaporator/condenser and the change in the height of liquid water inside the evaporator/condenser, respectively. The density of water is assumed to be constant. x_{e1} is the reference point and thus, at this point, the adsorption capacity of the zeolite is zero.

The maximum expected uncertainties of the measured value of the height of liquid water (x), volume of liquid water (v) and mass of adsorbent (m_{ad}) are +/- 0.05 cm, +/-2 ml and +/-1 gr, respectively. Using Equation 2.8 together with the uncertainties of the independent variables, the uncertainty associated to (X) calculated was found to be in the range of +/- 0.0023 to +/- 0.0026 $\mathrm{kg_w/kg_{ad}}$. In addition, the water baths and oven temperatures were kept constant with an uncertainty of +/- 0.2 °C. The accuracy of the thermocouples and pressure gages are +/- 0.2 °C and 1% of reading, respectively.

CHAPTER 3

EXPERIMENTAL INVESTIGATION OF A NATURAL ZEOLITE-WATER ADSORPTION COOLING UNIT

3.1 INTRODUCTION

In this chapter, a thermally driven adsorption cooling unit using natural zeolite-water as the adsorbent-refrigerant pair has been built and the performance of the cooling unit at various evaporator temperatures has been investigated. The system proposed in this thesis is very simple and can be easily operated since there is no vacuum sealing problems. Additionally, the condenser developed for this cooling system is novel compared to the ones reported. The condenser has a large condensation surface area and this shortens the desorption process time when the refrigerant vapor pressure is low and non-condensible gases exist on the condensation surfaces [63]. In addition, the working principle of the adsorption cooling system proposed is quite different than those that were typically used in previous studies. This means that the adsorbent bed temperature, not the evaporator pressure, is constant during the adsorption process and the pressure inside the adsorbent bed is lower than that of the evaporator at the starting point of the cooling cycle.

This chapter is mainly based on the publication " Solmuş İ., Kaftanoğlu B., Yamalı C., Baker D., Experimental investigation of a natural zeolite-water adsorption cooling unit. Applied Energy 88 (2011) 4206-4213. "

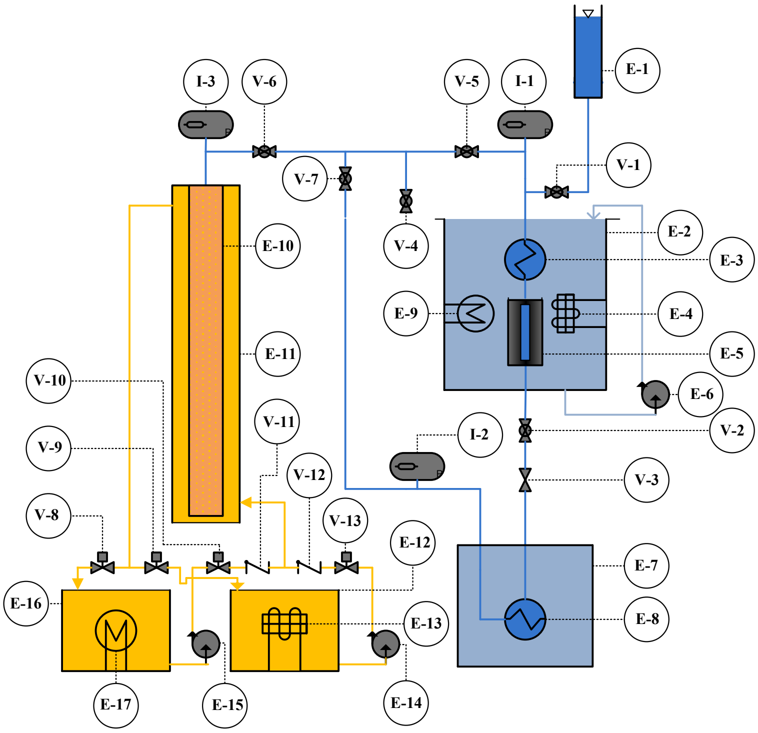

Figure 3.1: Schematic of the laboratory prototype [Feed water canister (E-1), Water bath (E-2), Condenser tube bundles (E-3), V-C cooling systems (E-4/13), Condenser canister (E-5), Circulation pumps (E-6/14/15), Refrigeration space (E-7), Evaporator (E-8), Electrical heater (E-9/17), Shell and tube adsorbent bed (E-10/11), Cooling and heating oil baths (E-12/16), Vacuum ball valves (V-1/2/4/5/6/7), Throttling valve with capillary tube (V-3), Solenoid valves (V-8/9/10/13), Check valves (V-11/12), Pressure transducers (I-1/2/3)].

3.2 DESCRIPTION OF THE PROTOTYPE ADSORPTION COOLING UNIT

A laboratory prototype of a natural zeolite-water adsorption cooling unit was designed and built, and its performance was analyzed experimentally under different working conditions. A schematic and photograph of the prototype are shown in Figure 3.1 and Figure 3.2, respectively. The primary components of the prototype are a shell and tube adsorbent bed, an evaporator, a condenser, heating and cooling baths, measurement instruments and supplementary system components. Detailed descriptions of each component are as follows.

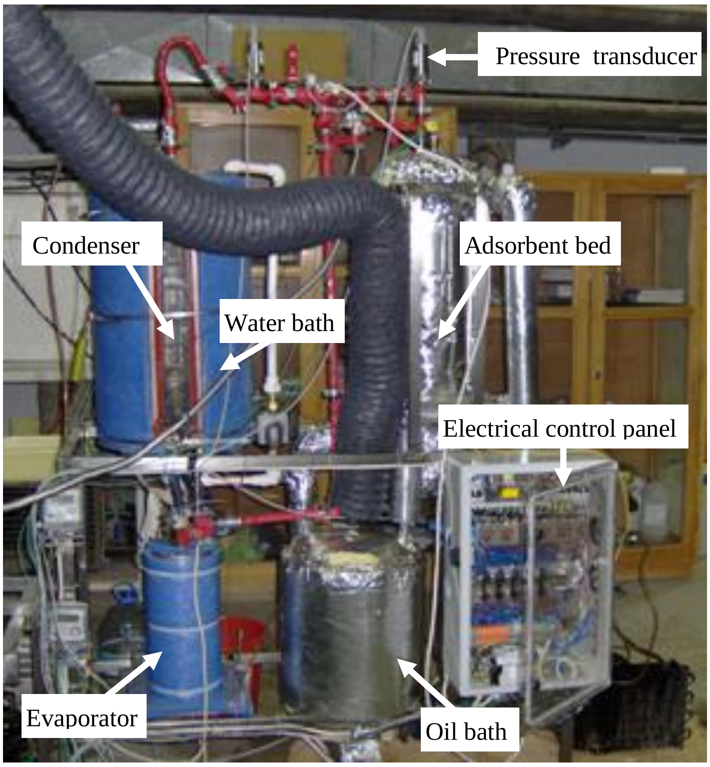

Figure 3.2: Photograph of the laboratory prototype.

3.2.1 Shell and Tube Adsorbent Bed

The adsorbent bed is the most important element of an adsorption cooling unit. Because of the poor thermal conductivity of the adsorbent materials used commonly in adsorption cooling units, the heat and mass transfer conditions in the adsorbent bed that affect the performance of the system should be considered carefully during the design of the bed. As a result, by taking into account these effects, the cycle time of the cooling unit and weight of the adsorbent bed can be reduced considerably.

In this study, the adsorbent bed is considered to enhance the bed's heat and mass transfer characteristics. The bed consists of an inner vacuum tube filled with zeolite (zeolite tube) inserted into a larger tubular shell. Thermo-physical properties of the natural zeolite used as an adsorbent in the bed are presented in Table 2.1. In this table, the definitions of the microporous and mesoporous are that the pore diameters of the material less than 2 nm and between 2 nm and 50 nm are called as microporous and mesoporous, respectively. The isosteric heat of

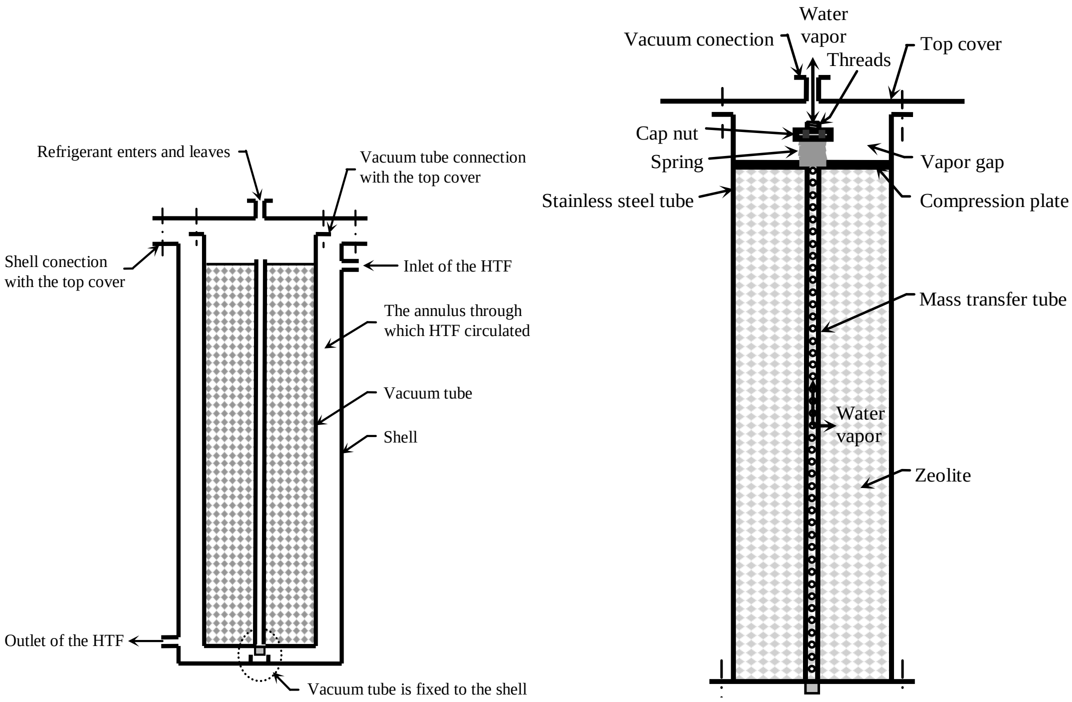

(a) Adsorbent bed (b) Vacuum tube

Figure 3.3: Schematics of the adsorbent bed and vacuum tube.

adsorption for water on natural zeolite as a function of equilibrium adsorption capacity is given in Chapter 2.

Schematics of the adsorbent bed and zeolite tube are shown in Figure 3.3, and a photograph of the adsorbent bed components is given in Figure 3.4. The zeolite tube is chosen to be a 73 mm diameter and 765 mm long stainless steel tube with top and bottom covers. The main reason behind this selection is based on the fact that the diameter of the tube is comparatively small according to its length and as a result of this, heat and mass transfer resistances in the radial direction as well. This means that the heat and mass transfer inside the adsorbent bed depend strongly on the radius. Therefore, the adsorbent bed thickness is kept as small as possible to improve the heat transfer conditions and as result, reduce the process time. Improving the heat transfer conditions makes it possible to reach the chemical equilibrium condition in a shorter time as well. The zeolite tube is filled approximately 9/10 full of zeolite with the remaining top 1/10 being a vapor gap. The tube is heated and cooled by circulating the heat transfer fluid (oil) between the shell and tube. Zeolite is a relatively poor thermal conductor and the zeolite used in this cooling unit consists of small grains, which when packed together

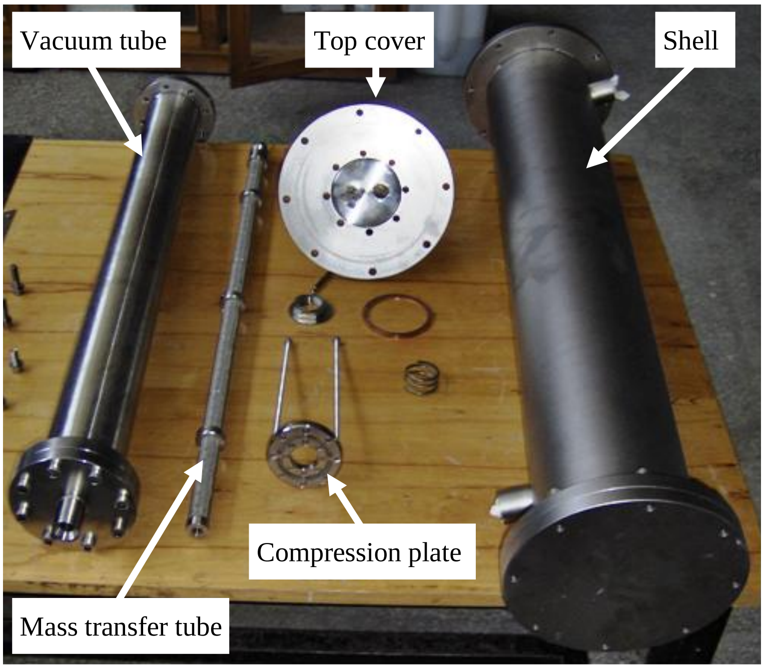

Figure 3.4: Photograph of the adsorbent bed components.

result in large contact resistances. To enhance heat transfer, and therefore reduce the thermal response time, the zeolite is compressed slightly using a spring loaded stainless steel disk, referred to as the compression plate. However, the compression should be limited within a range (for example: 20-25 kPa) to ensure that the mass transfer is not noticeably affected [64]. Refrigerant vapor enters and leaves the zeolite tube through the top cover by passing through the vapor gap. To enhance mass transfer between the vapor gap at the top of the zeolite tube and the packed zeolite, tightly spaced 3 mm mass transfer holes were drilled throughout the compression plate. Mass transfer to the lower levels of zeolite is enhanced through a mass transfer tube, 19 mm in diameter and 710 mm in height. One end of the mass transfer tube is fixed to the bottom cover of the zeolite tube while the other end passes through a hole in the compression plate and opens to the vapor gap. Numerous 3 mm mass transfer holes were drilled throughout the mass transfer tube, allowing refrigerant vapor to pass from the vapor gap, down the inside of the mass transfer tube, and then through the holes to the zeolite. To prevent the zeolite from passing through the small mass transfer holes in the compression plate and mass transfer tubes, a fine stainless mesh is used. Three thermocouples are distributed at equal axial distances along the mass transfer tube to obtain the temperature distribution inside the zeolite. The thermocouples penetrate the shell through a thermocouple feed through

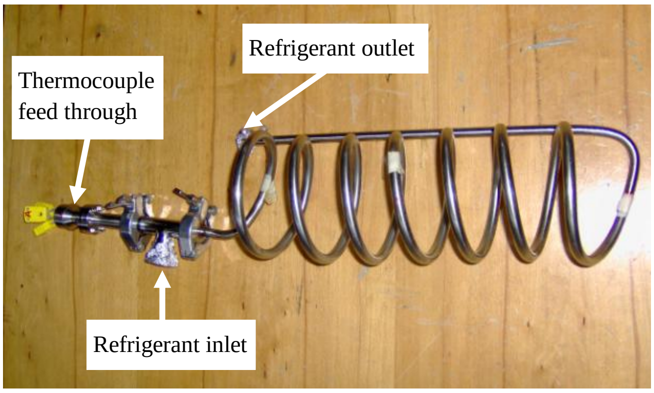

Figure 3.5: Photograph of the evaporator.

located on the top cover. The shell of the adsorber bed is a 136 mm diameter and 821 mm long stainless steel tube with top and bottom covers. The shell and zeolite tubes use the same top cover.

3.2.2 Evaporator

The evaporator consists of a 10 mm diameter and 3 m long stainless steel coil (E-8 in Figure 3.1) and a thermocouple feed through used to obtain the refrigerant temperatures at the bottom, middle and top of the coil. A photograph of the evaporator is shown in Figure 3.5. The evaporator is immersed in a well-insulated cylindrical water bath (cooling space). The volume of the water bath is 5 liters. To obtain a homogeneous temperature distribution inside the water bath, a small circulation pump (28 W) is used. Three thermocouples are equally distributed in the axial direction to measure the temperature distribution inside the water bath.

3.2.3 Condenser

The condenser consists of a condenser tube bundle and condenser canister as shown in Figure 3.6. The tube bundle consists of 22 8 mm diameter and 13.5 mm long stainless tubes (E-3 in Figure 3.1) used to condense the refrigerant. The condenser canister is a 58 mm inner diameter and 300 mm long stainless steel tube (E-5 in Figure 3.1) and is used to collect the liquid refrigerant. The height of liquid water inside the condenser canister is measured

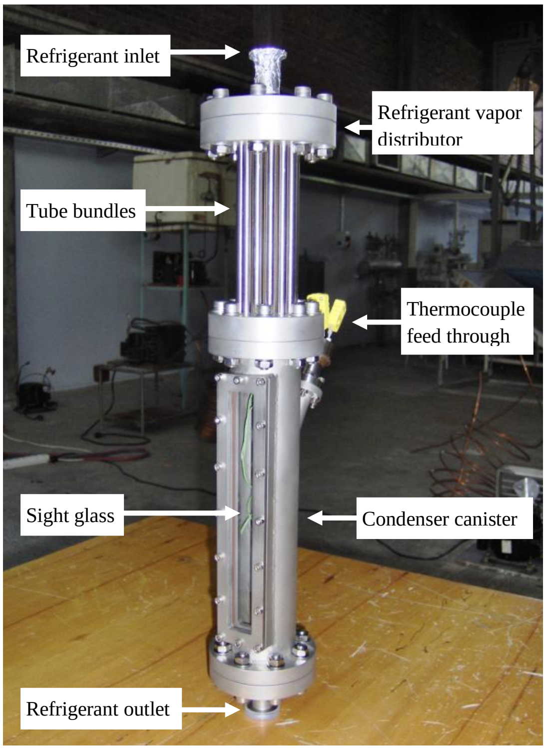

Figure 3.6: Photograph of the condenser.

visually through a glass covered 30 mm wide slot cut axially through one side of the cylinder. The change in the height of liquid water indicates nearly the change in mass of liquid water inside the condenser, and therefore the change in water adsorbed and desorbed on the zeolite. Three thermocouples are inserted using a thermocouple feed through in the condenser to measure the refrigerant liquid and vapor temperatures. To adjust the condenser pressure to a specific value, the condenser is submersed in a temperature controlled water bath containing a 1.5 kW electrical heater and an evaporator coil of a vapor compression cooling system. A water circulation pump is used to achieve uniform temperatures.

3.2.4 Heating and Cooling Baths

The temperature controlled heat exchange fluid (oil) in the heating and cooling baths is circulated by a pump between the shell and tube of the adsorbent bed to alternately heat and cool the zeolite. The volume of the heating and cooling baths is 28 liters. The heating bath used to regenerate the zeolite has two 1.5 kW electrical heaters. The cooling bath contains the evaporator of a vapor compression cooling system. The temperatures of the heating and cooling baths are measured by a thermocouple.

3.2.5 Measurement Instruments

Thermocouples: All the thermocouples used in the experimental prototype are K-type. The thermocouples used to measure the refrigerant's and zeolite's temperatures were passed through a vacuum chamber wall to the DAQ system using three Kurt J. Lesker (type K push on CF flange, single-ended) thermocouple feed troughs.

Pressure gauges: The refrigerant vapor pressure inside the vacuum tube, evaporator and condenser are measured with three Kurt J. Lesker (910 type) pressure gages.

Watt hour meter: During the desorption process, the amount of energy supplied to the oil inside the heating bath are measured by a KÖHLER (AEL. MF.02 type) watt hour meter connected to the electrical heaters in the heating bed.

DAQ system: All the thermocouple and pressure gage measurements were recorded and some of the system components were controlled by the data acquisition system consists of a Datataker-DT800 connected to a computer. The software DeLogger is used to program the Datataker-DT800 and download and visualize the data. The data are collected every 5 seconds and stored on the computer's hard disk.

3.2.6 Supplementary System Components

The supplementary system components used to connect the adsorbent bed, condenser and evaporator are as follows.

Vacuum ball valves: Six BOC EDWARDS (IBV16MKS type) vacuum ball valves are used and their locations are shown in Figure 3.1.

Throttling valve: To drop the refrigerant pressure from the condenser to evaporator pressure, a BOC EDWARDS (LV10K type) throttling valve is used between the condenser and evaporator. Moreover, after the throttling valve, a capillary tube approximately 0.5 m long is used to obtain the required pressure drop.

Solenoid and check valves: The line through which heat exchange fluid is circulated contains four PVD (T-AU 204 type) solenoid and two check valves and their locations in the experimental prototype are given in Figure 3.1.

A two-stage Edwards RV-3 rotary vane vacuum pump is used to initially evacuate the system before introducing the refrigerant (water) into the system. Note that condensation will occur on any inside surface exposed to the water vapor and at a lower temperature than the saturated water in the evaporator/condenser. Therefore, the whole piping system is maintained at an elevated temperature using electrical heater tape.

3.3 EXPERIMENTAL PROCEDURE

Before starting the experiments, the laboratory prototype is prepared according to the procedure given in Chapter 2. A known mass and volume of zeolite is poured into the zeolite tube and the zeolite tube is sealed and placed into the shell. The mass and volume of the zeolite are 1.87 kg and 2.5 lt. The shell and tube adsorbent bed is connected to the evaporator-condenser line. With all valves in Figure 3.1 open except (V-1), the whole system is evacuated until the pressure inside the system is less than 0.1 kPa, at which point the system is assumed to be sufficiently evacuated. Subsequently, valve (V-4) is closed and the vacuum pump is turned off. The valves at the inlet and outlet of the condenser (V-5 and V-2) are closed, the water intake valve (V-1) is slowly cracked and de-ionized water is allowed to flow into the condenser canister (E-5). After a certain period of time (approximately 10 seconds), valve (V-1) is closed. The temperatures of the evaporator and condenser baths are set to desired values.

The laboratory prototype cools intermittently since only one adsorbent bed is used. A complete adsorption cooling cycle (ideal cycle) that consists of adsorption (evaporation + cooling) and desorption (condensation + heating) processes can be explained with the help of the Dühring diagram given in Figure 3.7. The cycle starts at point A, where the temperature and pressure of the adsorbent bed are equal to T_{ad-c} and P_{ad}, respectively and the adsorption capacity of the zeolite is minimum. At this point, all valves are closed and the amount of water in the condenser canister is recorded. Then valves (V-6) and (V-7) are opened and valve (V-2) is cracked to start the adsorption process. The evaporator pressure (P_{ev-i}) corresponding to the saturation pressures of water at T_{ev-i} is higher than that in the adsorbent bed (P_{ad}). The

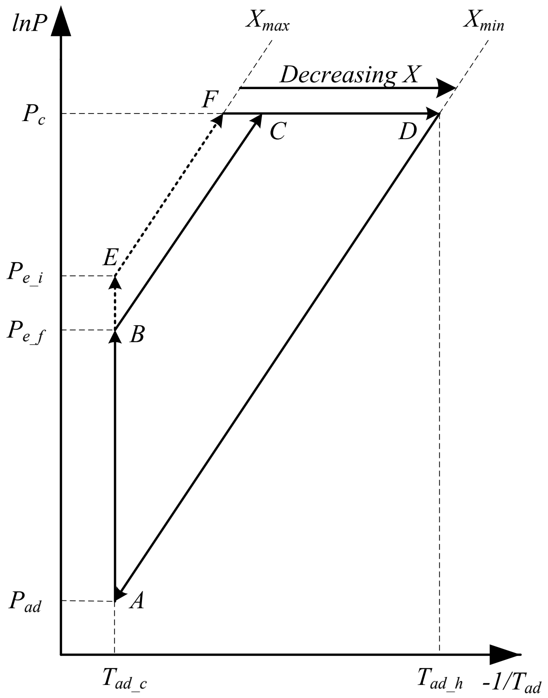

Figure 3.7: Dühring diagram of a water/zeolite adsorption process

refrigerant passing through the throttling valve (V-2) and capillary tube (V-3) is transferred to the evaporator coil before being adsorbed. Cold oil is circulated through the annulus of the bed to maintain the adsorbent bed at a constant temperature (T_{ad-c}). While the adsorption capacity of the zeolite increases gradually, the system pressure decreases from P_{ev-i} to P_{ev-f}. The reason behind the pressure drop between point E and B is due to the cooling of the evaporator bath from T_{ev-i} to T_{ev-f}. The adsorption process ends at point B, where the adsorption capacity of the zeolite is maximum. At point B, all valves except (V-6) are closed and the amount of water in the condenser canister is recorded again. The temperature of the bath containing the hot oil is set to T_{ad-h} and the heated oil is circulated through the annulus of the adsorbent bed. Heating of the zeolite isosterically increases the pressure from P_{ev-f} to P_c (C); i.e. the adsorption capacity of the zeolite is constant during this process. The condenser pressure (P_c) is the saturated pressure of the water corresponding to the water bath temperature of the condenser; i.e. T_c. Further heating of the zeolite starts the desorption process and valve (V-5) is opened to allow the water vapor to flow through the condenser tube bundles where condensation takes place. Heating of the zeolite from point C to D at a constant pressure decreases the amount of water adsorbed. At point D, the adsorption capacity of the zeolite is minimum. All valves are then closed and the adsorbent bed is left to the cool down from D to A through the night to complete the cycle. Overnight the adsorbent bed cools isosterically, and the pressure and temperature decrease from P_c to P_{ad} and from T_{ad-h} to T_{ad-c}. The cooling capacity of the laboratory prototype can be evaluated by comparing the level of water in the condenser canister at points A and B and the water's enthalpy of evaporation. The cycle time is only considered between the points A and D in the anticlockwise direction. Data were not recorded during the first cycle.

3.4 RESULTS AND DISCUSSIONS

The performance of the laboratory prototype has been investigated experimentally under various evaporator temperatures. The amount of energy supplied to the system during the desorption process by the electrical heaters inside the oil bath were measured using a watt hour meter. The energy consumed is due mainly to heat losses to the ambient from the adsorbent bed, oil bath and piping system through which oil circulated, heat capacities of the metal and oil, sensible heating of the zeolite, and the latent and sensible heating of the refrigerant. The performance of the cooling system was evaluated using two different methods. For the first method, all heat losses to the ambient, the heat capacities of the metal components and heat transfer fluid were neglected when the energy consumption of the cooling system during the desorption process was computed. This first method represents a theoretical limiting (ideal) case which an actual system can approach but never achieve. For this method, an empty adsorbent bed (i.e. no zeolite) was heated and the amount of energy consumed was recorded as a function of time. The amount of energy consumed by the prototype when the adsorbent bed is empty was subtracted from the amount of energy supplied to the prototype during the desorption process and the difference between these two values yields the net amount of energy (Q_u) to regenerate the zeolite. For the second method the amount of energy supplied to the system during the desorption process is equal to the energy supplied to the heaters indicated by the watt hour meter (Q_i) and accounts for all heat losses to the ambient and the heat capacities of the metal components and heat transfer fluid. The deviation between these performance measures indicates at least theoretical opportunities to improve the performance of the system through improved design.

The refrigeration capacity of the laboratory prototype was evaluated using the following equation.

$$Q_r = m_{ad} L (X_{max} - X_{min}) \tag{3.1}$$

In Equation 3.1, Q_r is the refrigeration capacity (kJ), m_{ad} is the mass of the adsorbent (kg) and L is the latent heat of the refrigerant (kJkg^{-1}). The adsorption capacity of the natural zeolite for both X_{max} and X_{min} are calculated using D-A equations with the experimental constants for adsorption and desorption processes given in Chapter 2.

The following equations are used to calculate the coefficient of the performance (COP), average volumetric specific cooling power density (SCP_v) and average mass specific cooling power density (SCP) of the experimental prototype for different evaporator temperatures.

Operating conditions and results of the experiments are given in Table 3.1.

$$COP_1 = \frac{Q_r}{Q_u} \tag{3.2}$$

$$COP_2 = \frac{Q_r}{Q_i} \tag{3.3}$$

$$SCP_v = \frac{Q_r}{t_{cy} V_{ad}} \tag{3.4}$$

$$SCP = \frac{Q_r}{t_{cy} m_{ad}} \tag{3.5}$$

In Equations above, Q_u is the net amount of energy supplied to the system (kJ), Q_i is the energy supplied to the heaters (kJ), t_{cy} is the cycle time of the system (min) and V_{ad} is the volume of the adsorbent material used.

In this study, a limited number of experimental data have been presented since the effect of the system parameters on the system performance is negligibly small because of the low ad-

Table 3.1: Operating conditions and experimental results.

	T_{ev} = 10 °C	T_{ev} = 15 °C	T_{ev} = 22.5 °C
t_a (min)	200	210	220
t_d (min)	190	180	180
t_{cy} (min)	390	390	400
T_{ad-h} (°C)	150	150	150
T_{ad-c} (°C)	50	45	45
T_c (°C)	30	30	30
T_{ev-i} (°C)	10	15	22.5
T_{ev-f} (°C)	10	12.5	17.5
Q_i (kJ)	10512	10440	10548
Q_l (kJ)	9576	9288	9288
Q_u (kJ)	936	1152	1260
Q_r (kJ)	253	285	314
COP_1	0.27	0.24	0.24
COP_2	0.024	0.027	0.029
SCP_v (kW/m^3)	4.3	4.8	5.2
SCP (W/kg)	5.7	6.5	7

sorption capacity of the natural zeolite-water working pair and the large amount of energy consumed by the system during the desorption process. We have previously studied the equilibrium adsorption capacity of water on a natural zeolite at different zeolite temperatures (40-150 °C) and water vapor pressures (0.87-7.38 kPa) for use in an adsorption cooling system in Chapter 2. Within this range of conditions, the maximum adsorption capacity of natural zeolite is nearly 0.12 kg_w/kg_{ad} for 40 °C and 7.38 kPa. The the cyclic adsorption capacity for bed temperature swings between 45 and 150 °C, maximum vapor pressure of 4.25 kPa and minimum vapor pressures of 2.73, 1.71 and 1.23 kPa varies between 0.055 and 0.067 kg_w/kg_{ad}. This amount is comparatively low according to other possible working pairs [63], and this is one of the reasons resulting in a low SCP for the adsorption cooling system using this natural zeolite/water working pair.

It can be seen in Table 3.1 that the adsorption process lasts slightly longer than the desorption process. The reason behind this behavior is that the adsorption process occurs at a relatively low pressure compared to the desorption process, mass transfer occurs more slowly, and hence, the adsorption rate is comparatively slower than the desorption rate. Additionally, the duration of the adsorption process at a constant evaporator temperature (i.e, pressure), is shorter than that of the adsorption processes with a decreasing evaporator temperature. The evaporator temperature (or pressure) decreases during the adsorption process due to the evaporative cooling effect in the evaporator. Therefore, the evaporator pressure becomes lower than the adsorbent bed pressure, which results in slow mass transfer of vapor and an overall slow process. The mean cycle time of the experimental prototype is 395 min and it is comparatively high relative to some of the previous studies in the literature such as [26] and [30]. This is mainly due to the existing limitations in heat transfer (low thermal conductivity of the natural zeolite) and mass transfer (intraparticle and interparticle) inside the adsorbent bed. Therefore, these types of limitations have to be eliminated to shorten the cycle time of the experimental prototype and this is our main target for the follow-up studies.

The cooling capacities of the experimental prototype at 10, 15 and 22.5 °C initial evaporator temperatures are 253, 285 and 314 kJ, respectively. The cooling capacity of the prototype increases as the initial evaporator temperature is increased. This is due to the increasing adsorption capacity of the adsorbent material used in the bed as a result of the increasing adsorption pressure. However, the cooling capacity of the experimental prototype is very limited especially at low pressures because of the low adsorption capacity of the natural zeolite-water adsorption pair used in the system. Although, the natural zeolite has a low adsorption capacity, it is very cheap as when compared to the other adsorbents since it is naturally mined and locally available. These characteristics make it attractive to use as an adsorbent material in adsorption cooling systems.

The COP value of experimental prototype is approximately 0.25 at 45 °C adsorption temperature, 150 °C desorption temperature, 30 °C condenser temperature and evaporator temperatures of 22.5, 15 and 10 °C when the heat losses from the system and heat capacities of the metal components and heat transfer fluid are neglected. However, the average COP value of the system nearly 0.027 under the same operating conditions when those neglected are considered. The COP value of the experimental prototype is a weak function of the evaporator temperature for the conditions investigated. It can be stated that a large amount of energy is wasted during the regeneration process to heat up the massive metal mass and heat transfer fluid and hence the thermal mass of these items needs to be considered carefully during the design of an adsorbent bed. However, the cooling system works under vacuum condition and thus, the thickness of some of the metal components has to be sufficiently large to maintain vacuum condition over long time periods. This is the one of the reasons that results in a massive metal mass but the problem can be partially reduced by using an adsorbent- refrigerant pair that works at nearly atmospheric pressure. The mean volumetric cooling power density per m^3 adsorbent (SCP_v) and mass specific cooling power density per kg adsorbent (SCP) of the experimental unit are 4.8 kW/m^3 and 6.4 W/kg, respectively. SCP_v and SCP values of the experimental prototype increase with increasing evaporator temperature and this is due to the increasing adsorption capacity of the adsorbent with increasing evaporator temperature.

The variation of the zeolite's temperature and refrigerant's pressure during the adsorption and desorption processes on the Duhring diagram are shown in Figure 3.8 for the upper and lower values of the initial evaporator temperature. It can be seen in Figure 3.8 that, unlike for the ideal cycle, the adsorbent bed temperature is not constant during the adsorption process. This temporal variation in temperature is due to the rate at which the heat of adsorption is released during the adsorption process being faster than the rate of heat transfer from the bed to the ambient due to heat transfer limitations such as poor thermal conductivity of the adsorbent material. As a result, the temperature inside the adsorbent bed rises and this causes the temperature to deviate from the ideal case. This temperature deviation is quite obvious for the $T_{ev,i}$ = 22.5 °C case since the adsorption capacity of the adsorbent material at that

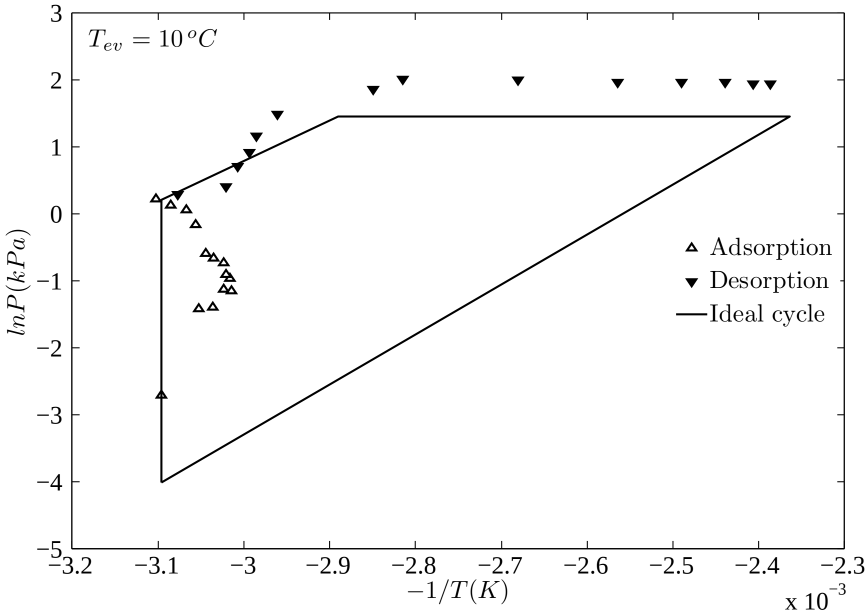

(a) $T_{ev,i}$ = 10 °C

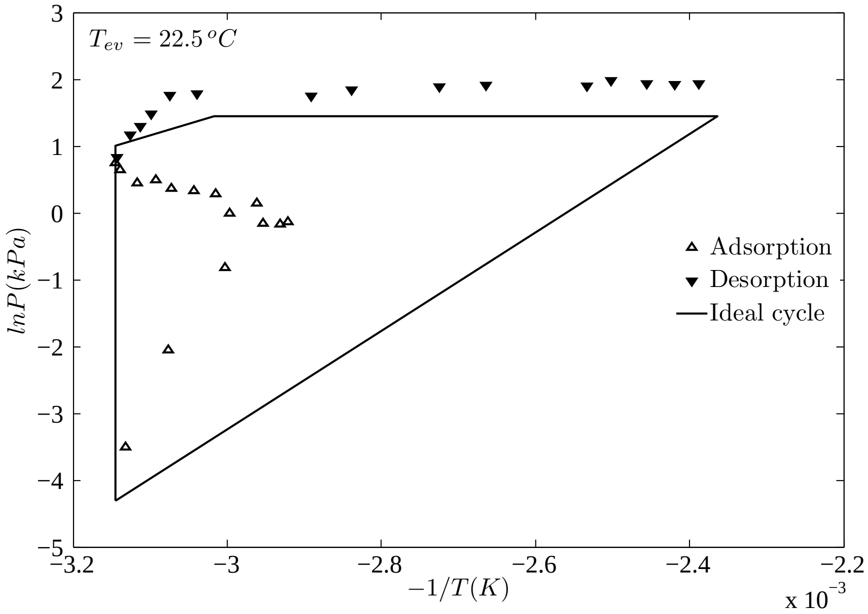

(b) $T_{ev,i}$ = 22.5 °C

Figure 3.8: The variation of the zeolite's temperature and refrigerant's pressure during the adsorption and desorption processes

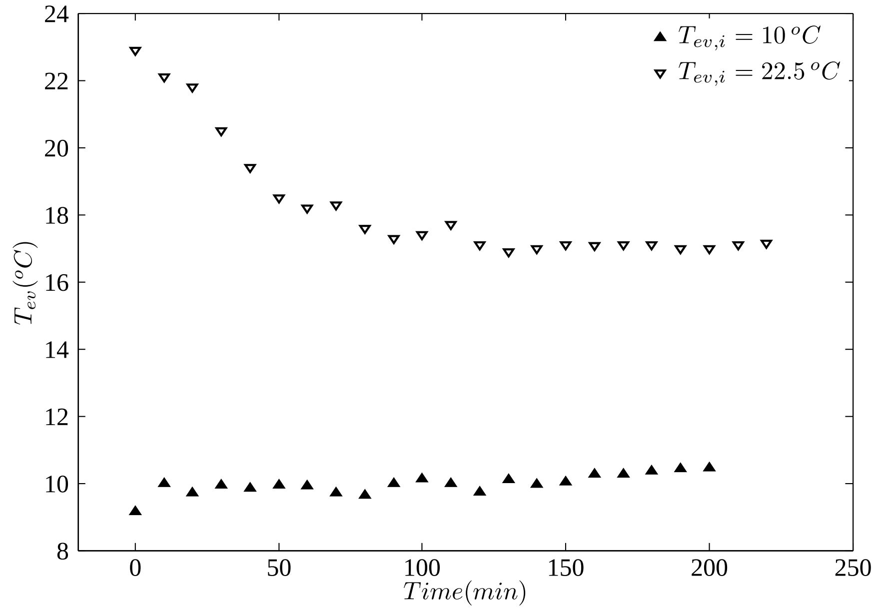

Figure 3.9: The transient variation of the evaporator bath temperature.

temperature is comparatively high and hence, the rate heat is generated is quite large as well. The pressure measured during the desorption process is slightly higher than that theoretically computed. This may be due to errors while reading the pressure measurement device and errors of the device itself.

The transient variation of the evaporator bath (cooling space) temperature is illustrated in Figure 3.9 for the upper and lower values of the initial evaporator temperature. The ambient temperature was higher than the initial evaporator temperature when the experiments were conducted. As a result, there was a net heat transfer from the ambient to the evaporator bath. The temperature of the evaporator bath decreased approximately from 22.5 to 17.5 °C after 80 min due to the high initial adsorption rate and then it becomes almost constant up to end of the process. However, the evaporator bath temperature only varies slightly when its initial temperature is almost equal to 10 °C because the cooling rate at 10 °C is almost equal to the rate of heat gain from the ambient and this keeps the temperature nearly constant. After 150 min, the evaporator bath temperature starts to increase because of the decreasing adsorption rate.

Table 3.2: Experimental uncertainties associated with the performance parameters of the cooling system.

$T_{ev,i}$ (°C)	COP_1	COP_2	SCP_v (kW/m^3)	SCP (W/kg)
10	+/- 0.0626	+/- 0.0011	+/- 0.1964	+/- 0.2617
15	+/- 0.0465	+/- 0.0011	+/- 0.1964	+/- 0.2617
22.5	+/- 0.0425	+/- 0.0011	+/- 0.1916	+/- 0.2552

3.4.1 Error Analysis

The experimental uncertainties associated to performance parameters of the system given in Table 3.1 were evaluated by using the Gauss' error propagation law and the results are presented in Table 3.2. The details of this method and the experimental uncertainties related to adsorption capacity of the zeolite can be found in Chapter 2. The accuracy of the thermocouples, watt-hour meter and pressure gages are +/- 0.2 °C, +/- 1.5 % of reading and 10^{-5}-1.3 kPa +/- 10 % of reading, 1.3-133.3 kPa +/- 1 % of reading, respectively. The maximum expected uncertainties of the measured volume (V_{ad}) and mass (m_{ad}) of the zeolite are +/- 5 ml and +/- 1 gr, respectively. The water's enthalpy of evaporation is considered to be constant when experimental error limits of the Q_r was computed.

CHAPTER 4

DERIVATION OF THE GOVERNING CONSERVATION EQUATIONS

4.1 INTRODUCTION

The overall performance of thermal powered adsorption cooling (TPAC) systems is typically limited by heat and mass transfer limitations inside the adsorbent bed due to the poor thermal conductivity of the solid adsorbent, and internal (intraparticle) and external (interparticle) mass transfer resistances. The external mass transfer resistance can be minimized by using packed beds with high permeability and the internal mass transfer resistance can be reduced by using the small particles size and/or particles with large pores [37]. The heat transfer in the adsorbent bed can be enhanced by applying the pressure on adsorbent particles and/or decreasing the particles diameter, which leads to decrease in contact resistance between the adsorbent particles and hence, increase in heat transfer rate [38]. However, minimizing the heat transfer limitations in the bed by means of decreasing the contact resistance between the particles tends to cause an increase in mass transfer resistance or in other words, decrease in bed permeability. On the other hand, any improvement in the bed permeability tends to result in poor heat transfer rate through the bed [45]. Therefore, it is necessary to optimize the heat and mass transfer properties of the adsorbent bed in order to improve its performance. For that reason, a mathematical model of the adsorbent bed needs to be developed to understand coupled heat and mass transfer mechanism in the bed and this model can be used to design and optimize a new and efficient adsorbent bed.

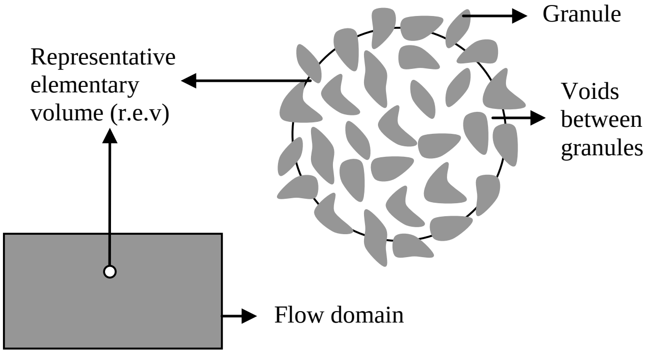

Figure 4.1: The representative elementary volume (r.e.v.).

4.1.1 Definition of a Porous Medium

The term porous medium defines a material consisting of a solid matrix with an interconnected void. The solid matrix is supposed to be either rigid (the usual situation) or it undergoes small deformation. The flow of one or more fluids through the material is provided by the interconnectedness of the void (the pores). In the simplest situation (single-phase flow) the void is saturated by a single fluid. In two-phase flow a liquid and a gas share the void space. A natural porous medium such as beach sand, sandstone, limestone, rye bread, wood, and the human lung, shows irregular distribution in terms of shape and size of the pores. On the pore scale (the microscopic scale) the flow quantities (velocity, pressure, etc.) will be clearly irregular. But in typical experiments the quantities of interest are measured over areas that cross many pores, and such space-averaged (macroscopic) quantities change in a regular manner with respect to space and time, and hence are amenable to theoretical treatment [59].

The usual way of deriving the laws governing the macroscopic variables is to begin with the standard equations obeyed by the fluid and to obtain the macroscopic equations by averaging over volumes or areas containing many pores. There are two ways to do the averaging: spatial and statistical. In the spatial approach, a macroscopic variable is defined as an appropriate mean over a sufficiently large representative elementary volume (r.e.v.); this operation yields the value of that variable at the centroid of the r.e.v. (Figure 4.1). In the statistical approach, the averaging is over an ensemble of possible pore structures that are macroscopically equivalent [59]. In this study, spatial approach was employed to do averaging over volumes. The porosity and permeability are commonly used to characterize a porous medium. The porosity

φ of a porous medium is defined as the fraction of the total volume of the medium that is occupied by void space and thus, 1-φ is the fraction that is occupied by solid. For an isotropic medium, the surface porosity (the fraction of void area to total area of a typical cross section) is generally considered to be equal to φ. The definition of permeability is a measure of mass transfer resistance for an adsorbate gas flow through the void between the solid adsorbent particles. The permeability is independent of the nature of the fluid but it depends on the geometry of the medium. The permeability of an isotropic medium is evaluated as a scalar.

4.2 MATHEMATICAL MODELING

4.2.1 Multiphase Flow

A representative elementary volume V is composed of the liquid, gas, and solid, and the interfaces of these three phases may move with time. The local volume averaged equations (macroscopic equations) for this three phase system can be obtained by applying the following equations and theorems to the pore size equations (microscopic equations).

The phase average and the intrinsic phase averages of some quantity ψ_α is defined as, respectively

$$\langle \psi_\alpha \rangle = V^{-1} \int_V \psi_\alpha \, dV \tag{4.1}$$

$$\langle \psi_\alpha \rangle^\alpha = V_\alpha^{-1} \int_{V_\alpha} \psi_\alpha \, dV \tag{4.2}$$

where, ψ_α is the value of ψ in the α phase and it is zero for the other phases. Thus, Equation 4.2 can be rewritten as follows

$$\langle \psi_\alpha \rangle^\alpha = V_\alpha^{-1} \int_V \psi_\alpha \, dV \tag{4.3}$$

The following equality can be obtained by comparing Equation 4.1 and Equation 4.3.

$$\langle \psi_\alpha \rangle = \epsilon_\alpha \langle \psi_\alpha \rangle^\alpha \tag{4.4}$$

ϵ_α is the volume fraction of the α-phase defined according to

$$\epsilon_\alpha = V_\alpha / V \tag{4.5}$$

In terms of the porosity φ of the medium, we can write

$$\epsilon_\alpha + \epsilon_\beta = \varphi \quad \text{and} \quad \epsilon_\varphi = 1 - \varphi \tag{4.6}$$

The deviations from the respective average values, for the α phase can be defined as

$$\widetilde{\psi_\alpha} \cong \psi_\alpha - \langle \psi_\alpha \rangle^\alpha \quad \text{and} \quad \widetilde{x_\alpha} \cong x_\alpha - \langle x_\alpha \rangle^\alpha \tag{4.7}$$

It can be also shown that

$$\langle \psi_\alpha x_\alpha \rangle^\alpha = \langle \psi_\alpha \rangle^\alpha \langle x_\alpha \rangle^\alpha + \left\langle \widetilde{\psi_\alpha} \widetilde{x_\alpha} \right\rangle^\alpha \quad \text{and} \quad \langle \psi_\alpha x_\alpha \rangle = \epsilon_\alpha \langle \psi_\alpha \rangle^\alpha \langle x_\alpha \rangle^\alpha + \left\langle \widetilde{\psi_\alpha} \widetilde{x_\alpha} \right\rangle \tag{4.8}$$

The following theorems are established by integration over an averaging volume.

Averaging theorem:

$$\langle \nabla \psi_\alpha \rangle = \nabla \langle \psi_\alpha \rangle + V^{-1} \int_{A_\alpha} \psi_\alpha n_\alpha \, dS \tag{4.9}$$

Modified averaging theorem:

$$\langle \nabla \psi_\alpha \rangle = \epsilon_\alpha \nabla \langle \psi_\alpha \rangle^\alpha + V^{-1} \int_{A_\alpha} \widetilde{\psi_\alpha} n_\alpha \, dS \tag{4.10}$$

Transport theorem:

$$\left\langle \frac{\partial \psi_\alpha}{\partial t} \right\rangle = \frac{\partial \langle \psi_\alpha \rangle}{\partial t} - V^{-1} \int_{A_\alpha} \psi w_\alpha . n_\alpha \, dS \tag{4.11}$$

where, A_α represents interface area between the α phase and other phases, w_α is the velocity vector of the interface, and n_α is the unit normal vector pointing outward from the α phase.

4.2.2 Governing Conservation Equations

Adsorption is the binding of atoms or molecules on the surface of a material. This process creates a film of the adsorbate (the molecules or atoms being accumulated) on the adsorbent's surface and pores. In addition, in a porous adsorbent there is a continues progression from multilayer adsorption to capillary condensation in which the smaller pores become completely filled with liquid adsorbate. Capillary condensation takes place because of the decreasing saturation vapor pressure in a small pore due to the effect of surface tension. However, capillary condensation is significant only an adsorbent having quite small pores [66].

In this study, it was assumed that there is no phase change onto adsorbent's surface and pores. As a consequence, the system is modeled as consisting of vapor adsorbate, adsorbed adsorbate, and solid adsorbent, termed hereafter the vapor (or gaseous) phase, adsorbed phase, and adsorbent, respectively, for conciseness. The adsorbed phase is modeled as being immobile and in thermal equilibrium with the adsorbent, and its volume fraction is assumed negligible. The combination of the adsorbed phase and adsorbent are modeled as a single solid and are referred to collectively as the solid phase. The resulting model is therefore two-phase (vapor and solid) with single phase flow (vapor).

In a porous medium, the properties of the vapor adsorbate (velocity, pressure, etc.) change irregularly on the pore scale (the microscopic scale). However, these quantities change in a smooth manner with respect to space and time if they are averaged over a representative elementary volume (the macroscopic scale) and this makes it possible to treat such quantities theoretically [59]. In the present study, the local volume averaging method, which has been utilized extensively in developing models for transport processes in porous media [65], was used to derive the governing macroscopic conservation equations from the microscopic ones.

The details of this method are found in references [58, 59]. The model is primarily based on the assumptions and simplifications presented as follows:

- the size of the adsorbent particles and the bed porosity are spatially uniform;
- the adsorbate's vapor phase is assumed to be an ideal gas;
- radiative heat transfer, viscous dissipation and the work done by pressure changes are neglected;
- the surface porosity is considered to be equal to the total porosity;
- physical properties such as thermal conductivities, specific heat capacities and viscosity are not a function of temperature;

The following is the derivation of vectorial forms of the volume averaged governing conservation equations.

4.2.2.1 Mass Conservation Equation

The pore scale mass conservation equations for the adsorbate gas are described as follows. Gas and solid phases are labeled by the subscripts g and s, respectively.

$$\frac{\partial \rho_g}{\partial t} + \nabla . \rho_g v_g = 0 \tag{4.12}$$

The interface condition at the gas-solid interface can be written as

$$n_{gs} . \rho_g v_g = C_g \quad \text{at} \quad A_{gs} \tag{4.13}$$

Taking the integral of the equation above over an elementary volume leads to

$$\left\langle \frac{\partial \rho_g}{\partial t} \right\rangle + \left\langle \nabla . \rho_g v_g \right\rangle = 0 \tag{4.14}$$

Application of the transport theorem and averaging theorem to the equation above, with the aid of Equation 4.8 yields to

$$\frac{\partial\left(\epsilon_g \left\langle\rho_g\right\rangle^g\right)}{\partial t} + \nabla.\left\langle\rho_g\right\rangle^g \left\langle v_g\right\rangle + \nabla.\left\langle\widetilde{\rho_g}\widetilde{v_g}\right\rangle + V^{-1}\int_{A_{gs}} n_{gs}.\rho_g\left(v_g - w_{gs}\right) dS = 0 \tag{4.15}$$

The third term, dispersive transport, in the equation above is generally considered to be small compared to the convective term which is based on the order of magnitude estimates given by [67]

$$\widetilde{v_g} = O\left(\left\langle v_g\right\rangle\right) \quad \text{and} \quad \widetilde{\rho_g} << \left\langle\rho_g\right\rangle^g \tag{4.16}$$

and thus, it can be omitted. Using the boundary condition given in Equation 4.13 together with the zero gas-solid interface velocity, the last term in the Equation 4.15 can be expressed as

$$V^{-1}\int_{A_{gs}} n_{gs}.\rho_g\left(v_g - w_{gs}\right) dS = a_v\left\langle C_g\right\rangle_{gs} \tag{4.17}$$

Here, we have defined the area averaged adsorption rate as

$$\left\langle C_g\right\rangle_{gs} = A_{gs}^{-1}\int_{A_{gs}} C_g\, dS \tag{4.18}$$

Final form of the continuity equation is expressed as

$$\frac{\partial\left(\epsilon_g \left\langle\rho_g\right\rangle^g\right)}{\partial t} + \nabla.\left\langle\rho_g\right\rangle^g \left\langle v_g\right\rangle + a_v\left\langle C_g\right\rangle_{gs} = 0 \tag{4.19}$$

In the equation above, the term first, second and third represent the rate of change of the mass of the adsorbate gas within the per unit control volume, net mass flux in the per unit control volume by convection and mass rate of adsorption into the per unit control volume, respectively. Some of the previous studies [39, 46], the mass rate of adsorption is defined according to

$$a_v \left\langle C_g \right\rangle_{gs} \cong (1 - \epsilon_t) \rho_s \frac{\partial X}{\partial t} \tag{4.20}$$

Substituting the equation above into the Equation 4.19 leads to

$$\frac{\partial \left(\epsilon_g \left\langle \rho_g \right\rangle^g \right)}{\partial t} + \nabla . \left\langle \rho_g \right\rangle^g \left\langle v_g \right\rangle + (1 - \epsilon_t) \rho_s \frac{\partial X}{\partial t} = 0 \tag{4.21}$$

The volume fraction of the gas phase ϵ_g is assumed to be equal to the total porosity ϵ_t that can be evaluated by

$$\epsilon_t = \epsilon_b + (1 - \epsilon_b) \epsilon_p \tag{4.22}$$

$\left\langle v_g \right\rangle$ is the superficial or Darcy's velocity. The density of the gas phase was assumed not to vary significantly within the averaging volume [58]. Thus, the point density ρ_g is used instead of the intrinsic phase average density when the above equation was derived. Finally, macroscopic continuity equation for the adsorbate gas can be written as follow

$$\epsilon_t \frac{\partial \rho_g}{\partial t} + \nabla . \rho_g v_g + (1 - \epsilon_t) \rho_s \frac{\partial X}{\partial t} = 0 \tag{4.23}$$

4.2.2.2 Momentum Conservation Equation

The velocity field of adsorbate gas in the adsorbent bed can be determined by using the following Ergun's equation

$$v + \frac{\rho_g}{\mu_g} K_E v \left| v \right| = - \frac{K_a}{\mu_g} \nabla P \tag{4.24}$$

or Darcy's equation

$$v = - \frac{K_d}{\mu_g} \nabla P \tag{4.25}$$

4.2.2.3 Energy Conservation Equations

During energy transport inside the adsorbent bed, it was assumed that significant temperature gradients exist between the vapor and solid phases; i.e., local thermal equilibrium was not assumed. Therefore, two different energy conservation equations are developed to determine the separate temperature fields of the gas and solid adsorbent phases.

a) Energy conservation equation for the gas phase

The macroscopic equations for the gas and solid adsorbent phases are obtained by applying the local volume averaging method to the pore scale equations. The pore scale energy conservation equation for the gas phase can be written as

$$\frac{\partial\left(\rho_g c_{pg} T_g\right)}{\partial t} + \nabla.\left(\rho_g v_g c_{pg} T_g\right) = \nabla.\left(k_g \nabla T_g\right) \tag{4.26}$$

The interface conditions at the gas-solid phase are given by

$$T_g = T_s \quad \text{and} \quad n_{gs}.k_g \nabla T_g = n_{gs}.k_s \nabla T_s \quad \text{at} \quad A_{gs} \tag{4.27}$$

which implies that both the temperature and the normal component of the heat flux are continues at the solid-gas interface. The local volume average energy equation for the gas phase can be expressed as

$$\left\langle \frac{\partial\left(\rho_g c_{pg} T_g\right)}{\partial t} \right\rangle + \left\langle \nabla.\left(\rho_g v_g c_{pg} T_g\right)\right\rangle = \left\langle \nabla.\left(k_g \nabla T_g\right)\right\rangle \tag{4.28}$$

The order of integration and differentiation can be interchanged for the first term of the equation above since the limits of integration are independent of time. The variation of the heat capacity within the averaging volume is very small and thus it can be neglected.

$$\frac{\partial\left\langle \rho_g c_{pg} T_g\right\rangle}{\partial t} = c_{pg} \frac{\partial\left\langle \rho_g T_g\right\rangle}{\partial t} \tag{4.29}$$

The integral in the right hand side of the equation can be decomposed by using the Equation

4.8 as follow

$$\frac{\partial \left\langle \rho_g c_{pg} T_g \right\rangle}{\partial t} = c_{pg} \frac{\partial \left(\epsilon_g \left\langle \rho_g \right\rangle^g \left\langle T_g \right\rangle^g \right)}{\partial t} + c_{pg} \frac{\partial \left\langle \widetilde{\rho_g} \widetilde{T_g} \right\rangle}{\partial t} \tag{4.30}$$

The second term in the right hand side of this equation can be neglected since it was assumed that the temperature deviation within the averaging volume is very small as it is compared to the phase average temperature. The length scale constraint associated with this simplification is given by J. Hager et al. [67] as follow

$$l_g / L << 1 \tag{4.31}$$

where, l_g and L represent the phase length scale and the distance over which significant changes in volume averaged quantities occur, respectively.

Application of the averaging theorem to the second term in the left hand side of the volume averaged energy equation leads to

$$\left\langle \nabla . \left(\rho_g v_g c_{pg} T_g \right) \right\rangle = \nabla . \left\langle \rho_g v_g c_{pg} T_g \right\rangle + V^{-1} \int_{A_{gs}} n_{gs} . \rho_g v_g c_{pg} T_g \, dS \tag{4.32}$$

The velocity, temperature and density can be decomposed according to Equation 4.7

$$\rho_g = \left\langle \rho_g \right\rangle^g + \widetilde{\rho_g} \quad v_g = \left\langle v_g \right\rangle^g + \widetilde{v_g} \quad T_g = \left\langle T_g \right\rangle^g + \widetilde{T_g} \tag{4.33}$$

Substitution of these decompositions into the first term on the right hand side of the Equation 4.32 yields to

$$\begin{aligned} \nabla . \left\langle \rho_g v_g c_{pg} T_g \right\rangle =& \nabla . \left\langle \left\langle \rho_g \right\rangle^g \left\langle v_g \right\rangle^g c_{pg} \left\langle T_g \right\rangle^g \right\rangle + \nabla . \left\langle \left\langle \rho_g \right\rangle^g \widetilde{v_g} c_{pg} \left\langle T_g \right\rangle^g \right\rangle + \nabla . \left\langle \left\langle \rho_g \right\rangle^g \left\langle v_g \right\rangle^g c_{pg} \widetilde{T_g} \right\rangle \\ &+ \nabla . \left\langle \left\langle \rho_g \right\rangle^g \widetilde{v_g} c_{pg} \widetilde{T_g} \right\rangle + \nabla . \left\langle \widetilde{\rho_g} \left\langle v_g \right\rangle^g c_{pg} \left\langle T_g \right\rangle^g \right\rangle + \nabla . \left\langle \widetilde{\rho_g} \widetilde{v_g} c_{pg} \left\langle T_g \right\rangle^g \right\rangle \\ &+ \nabla . \left\langle \widetilde{\rho_g} \left\langle v_g \right\rangle^g c_{pg} \widetilde{T_g} \right\rangle + \nabla . \left\langle \widetilde{\rho_g} \widetilde{v_g} c_{pg} \widetilde{T_g} \right\rangle \end{aligned} \tag{4.34}$$

J. Hager et al. [67] pointed out that all terms with a single deviation can be discarded provided that averages can be taken outside the integrals. The term containing three deviations can also be discarded because of having a negligible effect as it is compared to the remaining terms. Finally, the velocity deviation is on the order of the average velocity while the temperature and density deviations are comparatively small according to that of the average values. As a consequence, the term including the product of deviations that contains velocity deviation should be taken into account and this results in

$$\begin{aligned}\nabla . \left\langle \rho_g v_g c_{pg} T_g \right\rangle =& \nabla . \left\langle \left\langle \rho_g \right\rangle^g \left\langle v_g \right\rangle^g c_{pg} \left\langle T_g \right\rangle^g \right\rangle + \nabla . \left\langle \left\langle \rho_g \right\rangle^g \widetilde{v_g} c_{pg} \widetilde{T_g} \right\rangle \\ &+ \nabla . \left\langle \widetilde{\rho_g} \widetilde{v_g} c_{pg} \left\langle T_g \right\rangle^g \right\rangle \end{aligned} \tag{4.35}$$

Here we have used the fact that

$$\left\langle \left\langle v_g \right\rangle^g \right\rangle^g = \left\langle v_g \right\rangle^g \tag{4.36}$$

and this leads to

$$\begin{aligned}\nabla . \left\langle \rho_g v_g c_{pg} T_g \right\rangle =& \nabla . \left(\left\langle \rho_g \right\rangle^g \left\langle v_g \right\rangle c_{pg} \left\langle T_g \right\rangle^g \right) + \nabla . \left(\left\langle \rho_g \right\rangle^g c_{pg} \left\langle \widetilde{v_g} \widetilde{T_g} \right\rangle \right) \\ &+ \nabla . \left(\left\langle \widetilde{\rho_g} \widetilde{v_g} \right\rangle c_{pg} \left\langle T_g \right\rangle^g \right) \end{aligned} \tag{4.37}$$

where, averaged values are taken outside the integrals.

Using the differential relations, first term on the right hand side of the Equation 4.37 is written as

$$\nabla . \left(\left\langle \rho_g \right\rangle^g \left\langle v_g \right\rangle c_{pg} \left\langle T_g \right\rangle^g \right) = c_{pg} \left\langle T_g \right\rangle^g \nabla . \left\langle \rho_g \right\rangle^g \left\langle v_g \right\rangle + c_{pg} \left\langle \rho_g \right\rangle^g \left\langle v_g \right\rangle . \nabla \left\langle T_g \right\rangle^g \tag{4.38}$$

and third term on the right hand side of the Equation 4.37 is written as

$$\nabla.\left(\left\langle\widetilde{\rho_g}\widetilde{v_g}\right\rangle c_{pg}\left\langle T_g\right\rangle^g\right) = c_{pg}\left\langle T_g\right\rangle^g \nabla.\left\langle\widetilde{\rho_g}\widetilde{v_g}\right\rangle + c_{pg}\left\langle\widetilde{\rho_g}\widetilde{v_g}\right\rangle.\nabla\left\langle T_g\right\rangle^g \tag{4.39}$$

Substitution of the Equation 4.38 and Equation 4.39 into the Equation 4.37 results in

$$\begin{aligned}\nabla.\left\langle\rho_g v_g c_{pg} T_g\right\rangle =& c_{pg}\left\langle T_g\right\rangle^g \nabla.\left\langle\rho_g\right\rangle^g\left\langle v_g\right\rangle + c_{pg}\left\langle\rho_g\right\rangle^g\left\langle v_g\right\rangle.\nabla\left\langle T_g\right\rangle^g + \nabla.\left(\left\langle\rho_g\right\rangle^g c_{pg}\left\langle\widetilde{v_g}\widetilde{T_g}\right\rangle\right)\\ &+ c_{pg}\left\langle T_g\right\rangle^g \nabla.\left\langle\widetilde{\rho_g}\widetilde{v_g}\right\rangle + c_{pg}\left\langle\widetilde{\rho_g}\widetilde{v_g}\right\rangle.\nabla\left\langle T_g\right\rangle^g\end{aligned} \tag{4.40}$$

We can now focus on the last term in the Equation 4.32 and this term can be rewritten as follow with aid of the boundary condition given in Equation 4.13

$$V^{-1}\int_{A_{gs}} n_{gs}.\rho_g v_g c_{pg} T_g \, dS = V^{-1}\int_{A_{gs}} C_g c_{pg} T_g \, dS \tag{4.41}$$

Using the boundary condition given by Equation 4.27, the right hand side of Equation 4.41 can be rewritten as

$$V^{-1}\int_{A_{gs}} C_g c_{pg} T_g \, dS = \frac{A_{gs}}{V}\frac{1}{A_{gs}}\int_{A_{gs}} C_g c_{pg} T_s \, dS \tag{4.42}$$

The intrinsic interfacial area average is defined according to

$$\langle\psi_\alpha\rangle_{\alpha\beta} = \frac{1}{A_{\alpha\beta}}\int_{A_{\alpha\beta}} \psi_\alpha \, dS \tag{4.43}$$

and using this definition, Equation 4.42 can be expressed as

$$\frac{A_{gs}}{V}\frac{1}{A_{gs}}\int_{A_{gs}} C_g c_{pg} T_s \, dS = a_v c_{pg}\left\langle C_g T_s\right\rangle_{gs} \tag{4.44}$$

If the adsorption rate and the temperature are decomposed using the Gray decompositions, right hand side of the Equation 4.44 takes the following form

$$a_v c_{pg} \left\langle C_g T_s \right\rangle_{gs} = a_v c_{pg} \left\langle C_g \right\rangle_{gs} \langle T_s \rangle_{gs} + a_v c_{pg} \left\langle \widetilde{C_g} \widetilde{T_s} \right\rangle_{gs} \tag{4.45}$$

In the following development, although the last term in the right hand side of Equation 4.45, called as dispersive term, is ignored, J. Hager et al. [67] reported that further studies has to be done to validate this simplification.

We can now direct our attention to the conductive term in Equation 4.28. Application of the averaging theorem to this term yields to

$$\left\langle \nabla . k_g \nabla T_g \right\rangle = \nabla . \left\langle k_g \nabla T_g \right\rangle + V^{-1} \int_{A_{gs}} n_{gs} . k_g \nabla T_g \, dS \tag{4.46}$$

Using the averaging theorem, the first term on the right hand side of Equation 4.46 is rewritten as

$$\nabla . \left\langle k_g \nabla T_g \right\rangle = \nabla . \left[k_g \nabla \left\langle T_g \right\rangle + \frac{k_g}{V} \int_{A_{gs}} T_g n_{gs} \, dS \right] \tag{4.47}$$

Here, it was assumed that thermal conductivity of the gas phase is constant over the averaging volume. Equation 4.47 can also be expressed as

$$\nabla . \left\langle k_g \nabla T_g \right\rangle = \nabla . \left[k_g \epsilon_g \nabla \left\langle T_g \right\rangle^g + \frac{k_g}{V} \int_{A_{gs}} \left\langle T_g \right\rangle^g n_{gs} \, dS + \frac{k_g}{V} \int_{A_{gs}} \widetilde{T_g} n_{gs} \, dS \right] \tag{4.48}$$

The second term on the right hand side of Equation 4.48 is proved to be equal to zero provided that average temperature is taken outside the integral [68]. The final form of the Equation 4.46 can be given by

$$\left\langle \nabla . k_g \nabla T_g \right\rangle = \nabla . \left(k_g \epsilon_g \nabla \left\langle T_g \right\rangle^g \right) + \nabla . \left(\frac{k_g}{V} \int_{A_{gs}} \widetilde{T_g} n_{gs} \, dS \right) + V^{-1} \int_{A_{gs}} n_{gs} . k_g \nabla T_g \, dS \tag{4.49}$$

At this point, energy conservation equation for the gas phase takes the following form.

$$\begin{aligned}
c_{pg}\frac{\partial\left(\epsilon_g\left\langle\rho_g\right\rangle^g\left\langle T_g\right\rangle^g\right)}{\partial t} = & -c_{pg}\left\langle T_g\right\rangle^g\nabla.\left\langle\rho_g\right\rangle^g\left\langle v_g\right\rangle - c_{pg}\left\langle\rho_g\right\rangle^g\left\langle v_g\right\rangle.\nabla\left\langle T_g\right\rangle^g \\
& -\nabla.\left(\left\langle\rho_g\right\rangle^g c_{pg}\left\langle\widetilde{T_g}\widetilde{v_g}\right\rangle\right) - c_{pg}\left\langle T_g\right\rangle^g\nabla.\left\langle\widetilde{\rho_g}\widetilde{v_g}\right\rangle \\
& -c_{pg}\left\langle\widetilde{\rho_g}\widetilde{v_g}\right\rangle.\nabla\left\langle T_g\right\rangle^g - a_v c_{pg}\left\langle C_g\right\rangle_{gs}\left\langle T_s\right\rangle_{gs} \\
& +\nabla.\left(k_g\epsilon_g\nabla\left\langle T_g\right\rangle^g\right) + \nabla.\left(\frac{k_g}{V}\int_{A_{gs}}\widetilde{T_g}n_{gs}\,dS\right) \\
& +V^{-1}\int_{A_{gs}} n_{gs}.k_g\nabla T_g\,dS
\end{aligned} \tag{4.50}$$

Multiplying the all terms in Equation 4.19 by the heat capacity and intrinsic temperature of the gas phase and subtracting the result obtained from the Equation 4.50 lead to following simple form of the equation above.

$$\begin{aligned}
\epsilon_g c_{pg}\left\langle\rho_g\right\rangle^g\frac{\partial\left\langle T_g\right\rangle^g}{\partial t} = & -c_{pg}\left\langle\rho_g\right\rangle^g\left\langle v_g\right\rangle.\nabla\left\langle T_g\right\rangle^g - \nabla.\left(\left\langle\rho_g\right\rangle^g c_{pg}\left\langle\widetilde{T_g}\widetilde{v_g}\right\rangle\right) \\
& -c_{pg}\left\langle\widetilde{\rho_g}\widetilde{v_g}\right\rangle.\nabla\left\langle T_g\right\rangle^g - a_v c_{pg}\left\langle C_g\right\rangle_{gs}\left(\left\langle T_s\right\rangle_{gs} - \left\langle T_g\right\rangle^g\right) \\
& +\nabla.\left(k_g\epsilon_g\nabla\left\langle T_g\right\rangle^g\right) + \nabla.\left(\frac{k_g}{V}\int_{A_{gs}}\widetilde{T_g}n_{gs}\,dS\right) \\
& +V^{-1}\int_{A_{gs}} n_{gs}.k_g\nabla T_g\,dS
\end{aligned} \tag{4.51}$$

The third term on the right hand side of the Equation 4.51 is assumed to be very small as it is compared to the convective term and this assumption is based on the idea that is given by Equation 4.16. Therefore, it is not taken into account.

Here, we face to very complex closure problem including velocity and temperature deviations.

In order to solve this problem, we need appropriate representations for the deviation variables. This can be achieved by developing the governing differential equations and boundary conditions for the deviations variables. However, this is not easy task and hence, in this study, commonly used functional forms for the conduction, dispersion and inter facial flux will be employed instead of developing the closure problem.

$$\epsilon_g c_{pg} \left\langle \rho_g \right\rangle^g \frac{\partial \left\langle T_g \right\rangle^g}{\partial t} = - c_{pg} \left\langle \rho_g \right\rangle^g \left\langle v_g \right\rangle . \nabla \left\langle T_g \right\rangle^g - a_v c_{pg} \left\langle C_g \right\rangle_{gs} \left(\langle T_s \rangle_{gs} - \left\langle T_g \right\rangle^g \right)$$

$$+ \nabla . \left(\lambda_{ge} \nabla \left\langle T_g \right\rangle^g \right) + V^{-1} \int_{A_{gs}} n_{gs} . k_g \nabla T_g \, dS \tag{4.52}$$

where, λ_{ge} is the effective thermal conductivity of the gas in the presence of the solid adsorbent and it is the sum of the stagnant thermal conductivity and thermal dispersion tensor. Stagnant thermal conductivity tensor (due to the molecular diffusion) is defined as

$$\epsilon_g k_g \nabla \left\langle T_g \right\rangle^g + \frac{k_g}{V} \int_{A_{gs}} \widetilde{T_g} n_{gs} \, dS = \lambda_{gs} . \nabla \left\langle T_g \right\rangle^g \tag{4.53}$$

and thermal dispersion tensor (due to mechanical dispersion) is expressed in reference [59] as

$$\left\langle \rho_g \right\rangle^g c_{pg} \left\langle \widetilde{T_g} \widetilde{v_g} \right\rangle = -\lambda_{gd} . \nabla \left\langle T_g \right\rangle^g \tag{4.54}$$

We can now focus on the last term on the right hand side of Equation 4.52 that is called as interfacial heat flux. Application of the modified averaging theorem to the conductive term in Equation 4.28 leads to

$$\left\langle \nabla . k_g \nabla T_g \right\rangle = \epsilon_g \nabla . k_g \left\langle \nabla T_g \right\rangle^g + V^{-1} k_g \int_{A_{gs}} n_{gs} . \nabla \widetilde{T_g} \, dS \tag{4.55}$$

Imposing the modified averaging theorem to the intrinsic phase average of the temperature gradient and using the differential relation, equation above is written as

$$\left\langle \nabla . k_g \nabla T_g \right\rangle = \nabla . \left(\epsilon_g k_g \nabla \left\langle T_g \right\rangle^g + \frac{1}{V} \int_{A_{gs}} n_{gs} k_g \widetilde{T_g} \, dS \right) - \nabla \epsilon_g . k_g \nabla \left\langle T_g \right\rangle^g$$

$$+ V^{-1} \int_{A_{gs}} n_{gs} k_g \nabla \widetilde{T_g} \, dS \tag{4.56}$$

As this equation is compared to the Equation 4.51, it can be clearly seen that interfacial heat flux is equal to

$$V^{-1} \int_{A_{gs}} n_{gs} k_g \nabla T_g \, dS = -\nabla \epsilon_g . k_g \nabla \left\langle T_g \right\rangle^g + V^{-1} \int_{A_{gs}} n_{gs} k_g \nabla \widetilde{T_g} \, dS \tag{4.57}$$

The first term on the right hand side of the equation above is negligible since volume fraction of the gas phase is assumed to be constant and hence, interfacial heat flux takes the following form

$$V^{-1} \int_{A_{gs}} n_{gs} k_g \nabla T_g \, dS = V^{-1} \int_{A_{gs}} n_{gs} k_g \nabla \widetilde{T_g} \, dS \tag{4.58}$$

This result shows that the spatial deviation temperature controls the interfacial heat flux and it can be calculated by using the following relation. The derivation of this relationship is explicitly given by J.Hager et al. [67].

$$-V^{-1} \int_{A_{gs}} n_{gs} . k_g \nabla T_g \, dS = a_v h_{gs} \left(\left\langle T_g \right\rangle^g - \langle T_s \rangle_{gs} \right) \tag{4.59}$$

Final form of the energy equation for the gas phase is given by

$$\epsilon_g c_{pg} \rho_g \frac{\partial T_g}{\partial t} + c_{pg} \rho_g v_g . \nabla T_g + (1 - \epsilon_t) \rho_s \frac{\partial X}{\partial t} c_{pg} \left(T_s - T_g \right) = - a_v h_{gs} \left(T_g - T_s \right)$$

$$+ \nabla . \left(\lambda_{ge} \nabla T_g \right) \tag{4.60}$$

Here, the area averaged temperatures is represented by the volume averaged temperatures [67] and the intrinsic phase averages of density and temperature is represented by point density and temperature since variation of density and temperature over the averaging volume is considered to be very small [59].

b) Energy conservation equation for the solid phase

Here, solid adsorbent and gas phase molecules binding on the surface of the solid adsorbent are considered as a single solid phase, i.e., there is local thermal equilibrium between the adsorbent and adsorbed adsorbate and volume fraction of the adsorbed adsorbate is neglected. The microscopic energy conservation equation for the solid phase is

$$\frac{\partial\left(\rho_s c_{ps} T_s\right)}{\partial t} = \nabla.\left(k_s \nabla T_s\right) + \dot{Q}_s \tag{4.61}$$

The local volume averaged macroscopic energy conservation equation for the solid phase is derived in the same way as for the gas phase without any further development. It is given by

$$\epsilon_s c_{ps} \langle \rho_s \rangle^s \frac{\partial \langle T_s \rangle^s}{\partial t} = \nabla.\left(\lambda_{se} \nabla \langle T_s \rangle^s\right) + V^{-1} \int_{A_{sg}} n_{sg} k_s \nabla T_s \, dS + \left\langle \dot{Q}_s \right\rangle \tag{4.62}$$

Using the boundary condition given in Equation 4.27, second term on the right hand side of the Equation 4.62 can be rewritten as

$$V^{-1} \int_{A_{sg}} n_{sg} k_s \nabla T_s \, dS = -V^{-1} \int_{A_{gs}} n_{gs} k_g \nabla T_g \, dS = a_v h_{gs} \left(\left\langle T_g \right\rangle^g - \langle T_s \rangle_{gs} \right) \tag{4.63}$$

Substitution of the result above into the Equation 4.62 yields to

$$\epsilon_s c_{ps} \langle \rho_s \rangle^s \frac{\partial \langle T_s \rangle^s}{\partial t} = \nabla.\left(\lambda_{se} \nabla \langle T_s \rangle^s\right) + a_v h_{gs} \left(\left\langle T_g \right\rangle^g - \langle T_s \rangle_{gs} \right) + \left\langle \dot{Q}_s \right\rangle \tag{4.64}$$

The last term on the right hand side of Equation 4.64 is the heat generation during the adsorption process and given according to [46, 47] as below

$$\left\langle \dot{Q}_s \right\rangle = (1 - \epsilon_t) \rho_s \frac{\partial X}{\partial t} Q_{ad} \tag{4.65}$$

Finally, the governing energy conservation equations for the solid phase becomes

$$\epsilon_s c_{ps} \rho_s \frac{\partial T_s}{\partial t} = \nabla.\left(\lambda_{se} \nabla T_s\right) + a_v h_{gs} \left(T_g - T_s\right) + \left(1 - \epsilon_t\right) \rho_s \frac{\partial X}{\partial t} Q_{ad} \tag{4.66}$$

where, $\epsilon_s c_{ps} \rho_s = \rho_s \left(1 - \epsilon_t\right) \left[c_{ps} + X c_{pg}\right]$

CHAPTER 5

ONE-DIMENSIONAL NUMERICAL ANALYSIS OF HEAT AND MASS TRANSFER DURING ADSORPTION PROCESS IN AN ADSORBENT BED

5.1 INTRODUCTION

In this chapter, the influence of several design parameters such as diameter of the adsorbent particles, the bed thickness, the total porosity and the thermal conductivity of the adsorbent material on the transient distributions of temperature, pressure and amount adsorbed in the radial direction of a cylindrical adsorbent bed of a solid sorption cooling unit using silica-gel/water as working pair have been investigated numerically. Additionally, validity of the thermal equilibrium model assumption has been shown under the given boundary and design conditions. For the conditions investigated, the validity of the local thermal equilibrium and spatially isobaric bed assumptions have been confirmed. To improve the performance of the bed considered, efforts should be focused on reducing heat transfer resistances and intra-particle (interior) mass transfer resistances but not inter-particle (exterior) mass transfer resistances.

This chapter is mainly based on the publication "Solmuş İ., Rees D. Andrew S., Yamalı C., Baker D., Kaftanoğlu B., Numerical Investigation of couple heat and mass transfer inside the adsorbent bed of an adsorption cooling unit. International Journal of Refrigeration, doi:10.1016/j.ijrefrig.2011.12.006."

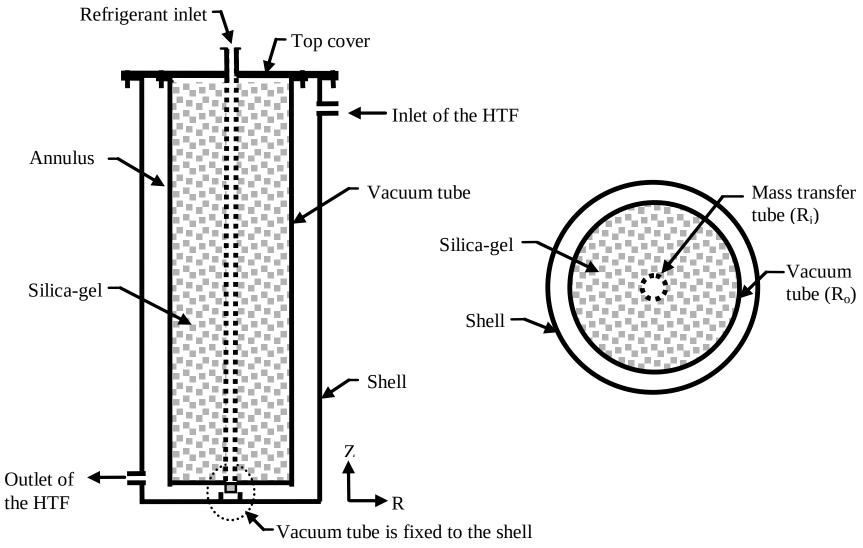

Figure 5.1: A schematic view of the cylindrical adsorbent bed.

5.2 DESCRIPTION OF THE ADSORBENT BED

A schematic of the cylindrical adsorbent bed under consideration is shown in Figure 5.1. In this study, silica-gel/water is used as an adsorbent-adsorbate (or adsorbent-refrigerant) working pair and their thermo-physical properties are presented in Table 5.1. The bed consists of an inner vacuum tube, 36.5 mm in radius (R_o), a mass transfer tube, 9.5 mm in radius (R_i) and a larger tubular shell. The annulus between the vacuum and mass transfer tubes is filled with silica-gel granules. The vacuum tube is inserted into the larger tubular shell and cooled by a heat transfer fluid circulated between the shell and tube. Refrigerant vapour enters the vacuum tube through the top of the mass transfer tube and flows from the inner surface of the annulus to the annulus's outer surface. Both ends of the vacuum tube are well insulated and therefore heat and mass transfer are assumed to take place only in the radial direction.

5.3 MATHEMATICAL MODELING

5.3.1 Mass Conservation Equation

The macro scale mass conservation equation for the adsorbate gas can be written as:

$$\epsilon_t \frac{\partial \rho_g}{\partial t} + \frac{1}{r}\frac{\partial\left(r\rho_g v_r\right)}{\partial r} + (1-\epsilon_t)\,\rho_s \frac{\partial X}{\partial t} = 0 \tag{5.1}$$

The volume fraction of the gas phase, ϵ_g, is assumed to be equal to the total porosity, ϵ_t, and may be evaluated using,

$$\epsilon_t = \epsilon_b + (1-\epsilon_b)\,\epsilon_p \tag{5.2}$$

The rate that adsorbate vapor passes from the outside of an adsorbent particle to an adsorbed state inside the particle is assumed to be limited by the internal mass transfer resistances associated with vapor flow through the particle's internal pores. This means that the mass transfer resistance within the adsorbent particles is taken into account, i.e., adsorption equilibrium is not assumed. The Linear Driving Force (LDF) model is used to describe the adsorption rate or internal mass transfer. The LDF model is expressed as follows:

$$\frac{\partial X}{\partial t} = k_m\,(X_\infty - X) \tag{5.3}$$

where k_m is the internal mass transfer coefficient given by

$$k_m = 15 D_e / r_p^2 \tag{5.4}$$

and D_e is the equivalent diffusivity in the adsorbent particles which may be expressed as [69]

$$D_e = D_o \exp\left(-E_a / R T_s\right) \tag{5.5}$$

The equilibrium adsorption capacity of the adsorbent to the adsorbent's temperature and the adsorbate's pressure, i.e., $X = f(P_v, T_s)$, may be evaluated using the following modified Dubinin-Astakhov (D-A) equation [69].

$$X_\infty = 0.346 \exp\left[-5.6\,(T_s/T_{sat} - 1)^{1.6}\right] \tag{5.6}$$

5.3.2 Momentum Equation

The pressure in the adsorbent bed is not assumed to be uniform and hence the external mass transfer resistances are considered. The velocity of the adsorbate gas in the radial direction is determined by using the following Ergun's equation [47]. This equation is more general than Darcy's equation since it not only includes viscous effects but also inertial effects. However, Darcy's law can also be used if the flow speed is very low (creeping flow). Ergun's equation is,

$$v + \frac{\rho_g}{\mu_g} K_E v \left| v \right| = -\frac{K_a}{\mu_g} \nabla P \tag{5.7}$$

The parameter, K_E, which is usually called the Forchheimer coefficient, that appears in Ergun's equation accounts for the inertial effects and is defined as follows:

$$K_E = \frac{1.75 d_p}{150 \left(1 - \epsilon_b\right)} \tag{5.8}$$

The adsorbate gas (assumed an ideal gas) flowing between the adsorbent particles inside the adsorbent bed includes Poiseuille flow (viscous flow), Knudsen flow (diffusion flow) and surface flow. Surface flow can be neglected because of the very low concentration of adsorbed substance on the macro pore surfaces [40]. The parameter K_a is the apparent permeability that takes into account diffusion and viscous flow, and described in [46] as:

$$K_a = K_d + \frac{D_g \mu_d}{P} \tag{5.9}$$

where K_d is the real permeability which can be calculated by the following the semi-empirical Blake-Kozeny equation,

$$K_d = \frac{d_p^2 \epsilon_b^3}{150 \left(1 - \epsilon_b\right)^2} \tag{5.10}$$

The diffusivity of the adsorbate gas D_g, which involves Knudsen and molecular diffusions, was evaluated by the following relation [47, 70]

$$D_g = \left(\frac{1}{D_m} + \frac{1}{D_k}\right)^{-1} \frac{\epsilon}{\tau} \tag{5.11}$$

Where,

$$D_m = 0.02628 \frac{\sqrt{T^3/M}}{P\sigma^2\Omega} \quad \text{and} \quad D_k = 48.5 d_{pore} \left(T/M\right)^{0.5} \tag{5.12}$$

5.3.3 Energy Conservation Equations

5.3.3.1 Energy Conservation Equation for the Gas Phase

The macro scale energy conservation equation for the gas phase is written as:

$$c_{pg}\rho_g \left[\epsilon_t \frac{\partial T_g}{\partial t} + v_r \frac{\partial T_g}{\partial r}\right] + (1-\epsilon_t)\rho_s \frac{\partial X}{\partial t} c_{pg} \left(T_s - T_g\right) = \frac{1}{r}\frac{\partial}{\partial r}\left(r\lambda_{ge}\frac{\partial T_g}{\partial r}\right) + a_v h_{gs}\left(T_s - T_g\right) \tag{5.13}$$

5.3.3.2 Energy Conservation Equation for the Solid Phase

The local volume-averaged macroscopic energy conservation equation for the solid phase is given by

$$\rho_s (1-\epsilon_t)\left[c_{ps} + X c_{pg}\right] \frac{\partial T_s}{\partial t} = \frac{1}{r}\frac{\partial}{\partial r}\left(r\lambda_{se}\frac{\partial T_s}{\partial r}\right) - a_v h_{gs}\left(T_s - T_g\right) + (1-\epsilon_t)\rho_s \frac{\partial X}{\partial t} Q_{ad} \tag{5.14}$$

The effective thermal conductivity for the solid and gas phases can be defined as follow [59]

$$\lambda_{se} = (1-\epsilon_t) k_s \quad \text{and} \quad \lambda_{ge} = \epsilon_t k_g \tag{5.15}$$

The vapor -solid specific surface area for spherical particles is determined by [39]

$$a_v = 6\left(1 - \epsilon_t\right)/d_p \tag{5.16}$$

The interfacial heat transfer coefficient for the spherical particle is evaluated by [39]

$$Nu_d = 2 + 1.8Pr^{0.33}Re_d^{0.5} \tag{5.17}$$

Where,

$$Re_d = \frac{\rho_g v_r d_p}{\mu_g}, \quad Nu_d = \frac{h_{gs} d_p}{k_g} \quad \text{and} \quad Pr = \frac{\mu_g c_{pg}}{k_g} \tag{5.18}$$

The isosteric heat of adsorption Q_{ad} for the silica-gel/water working pair is determined by using the following equations [71].

$$Q_{ad} = 3500 - 13400X \quad \text{for} \quad X \leq 0.05$$

$$Q_{ad} = 2950 - 1400X \quad \text{for} \quad X > 0.05 \tag{5.19}$$

The equation of state for the adsorbate vapor phase is written as:

$$P = \rho_g R_g T_g \tag{5.20}$$

5.3.4 Initial and Boundary Conditions

The temperatures (solid and gas), pressure and amount-adsorbed distributions in the radial direction inside the adsorbent bed are initially considered to be uniform.

$$T_g\left(0, r\right) = T_s\left(0, r\right) = T_i, \quad P\left(0, r\right) = P_i \quad \text{and} \quad X\left(0, r\right) = X_i \tag{5.21}$$

At the inner surface of the annulus, it is assumed that the adsorbate gas pressure is equal to the evaporator pressure, and the temperature gradients for both the solid and gas phases are zero.

$$P\left(t,R_i\right) = P_{ev} \quad \text{and} \quad \frac{\partial T_g}{\partial r}\left(t,R_i\right) = \frac{\partial T_s}{\partial r}\left(t,R_i\right) = 0 \tag{5.22}$$

At the solid wall (i.e. the outer surface of the annulus), there is a zero pressure gradient because the wall is impermeable, and the temperatures of the solid and gas phases are equal to a prescribed boundary temperature. Moreover, there is local thermal equilibrium between the phases at this boundary.

$$\frac{\partial P}{\partial r}\left(t,R_o\right) = 0 \quad \text{and} \quad T_g\left(t,R_o\right) = T_s\left(t,R_o\right) = T_b \tag{5.23}$$

5.4 METHOD OF SOLUTION

The coupled governing partial differential equations were solved numerically due to their complexity and nonlinearity. The finite difference technique was used to convert these equations to a system of algebraic equations and a fully implicit scheme was chosen to eliminate possible numerical instabilities. The unsteady, diffusion, and convective terms were discretized using forward difference, central difference, and first order upwind schemes, respectively. Additionally, in order to eliminate the imaginary points, the spatial derivatives on the inner and outer boundaries (derivative type boundary conditions) were discretized by forward or backward difference whichever appropriate. The first order upwind scheme is given by

$$v_r\frac{\partial u}{\partial x} = \left(1-a\right)v_r\frac{u_i-u_{i-1}}{\Delta x} + av_r\frac{u_{i+1}-u_i}{\Delta x} \quad \text{for} \quad v_r > 0 \quad a = 0$$

$$\text{for} \quad v_r < 0 \quad a = 1 \tag{5.24}$$

Adopting the appropriate finite difference scheme for each derivative in the governing conservation equations results in the followings:

Mass conservation equation:

$$\epsilon_t \frac{\left(\rho_i^{n+1} - \rho_i^{n}\right)}{\Delta t} + \frac{\rho_i^{n+1} v_{r_i}^{n+1}}{r_i} + \rho_i^{n+1} \frac{\left(v_{r_{i+1}}^{n+1} - v_{r_{i-1}}^{n+1}\right)}{2\Delta r} + v_{r_i}^{n+1}\left[(1-a)\frac{\rho_i^{n+1} - \rho_{i-1}^{n+1}}{\Delta r} + a\frac{\rho_{i+1}^{n+1} - \rho_i^{n+1}}{\Delta r}\right]$$

$$+ (1-\epsilon_t)\rho_s k_{m_i}^{n+1}\left(X_{\infty_i}^{n+1} - X_i^{n+1}\right) = f_1 \tag{5.25}$$

Momentum equation:

$$v_{r_i}^{n+1} + \frac{\rho_i^{n+1}}{\mu_g} K_E \left(v_{r_i}^{n+1}\right)^2 + \frac{K_a}{\mu_g}\left[\frac{P_{i+1}^{n+1} - P_{i-1}^{n+1}}{2\Delta r}\right] = f_2 \tag{5.26}$$

Energy conseravtion equation for the gas phase:

$$c_{pg}\rho_g\epsilon_t \frac{T_{g_i}^{n+1} - T_{g_i}^{n}}{\Delta t} + c_{pg}\rho_g v_{r_i}^{n+1}\left[(1-a)\frac{T_{g_i}^{n+1} - T_{g_{i-1}}^{n+1}}{\Delta r} + a\frac{T_{g_{i+1}}^{n+1} - T_{g_i}^{n+1}}{\Delta r}\right]$$

$$- \lambda_{ge}\left[\frac{T_{g_{i+1}}^{n+1} - T_{g_{i-1}}^{n+1}}{r_i\,(2\Delta r)} + \frac{T_{g_{i+1}}^{n+1} - 2T_{g_i}^{n+1} + T_{g_{i-1}}^{n+1}}{\Delta r^2}\right] - a_v h_{gs_i}^{n+1}\left(T_{s_i}^{n+1} - T_{g_i}^{n+1}\right)$$

$$+ (1-\epsilon_t)\rho_s c_{pg} k_{m_i}^{n+1}\left(X_{\infty_i}^{n+1} - X_i^{n+1}\right)\left(T_{s_i}^{n+1} - T_{g_i}^{n+1}\right) = f_3 \tag{5.27}$$

Energy conseravtion equation for the solid phase:

$$c_{ms_i}^{n+1}\frac{T_{s_i}^{n+1} - T_{s_i}^{n}}{\Delta t} - \lambda_{se}\left[\frac{T_{s_{i+1}}^{n+1} - T_{s_{i-1}}^{n+1}}{r_i\,(2\Delta r)} + \frac{T_{s_{i+1}}^{n+1} - 2T_{s_i}^{n+1} + T_{s_{i-1}}^{n+1}}{\Delta r^2}\right]$$

$$+ a_v h_{gs_i}^{n+1}\left(T_{s_i}^{n+1} - T_{g_i}^{n+1}\right) - (1-\epsilon_t)\rho_s Q_{ad_i}^{n+1} k_{m_i}^{n+1}\left(X_{\infty_i}^{n+1} - X_i^{n+1}\right) = f_4 \tag{5.28}$$

The finite difference formulations of the parameters calculated at each grid points in the computational domain are given as below;

Equation of state for vapor phase:

$$P_i^{n+1} - \rho_{g_i}^{n+1} R T_{g_i}^{n+1} = f_5 \tag{5.29}$$

Saturation pressure of the refrigerant vapor:

$$T_{sat_i}^{n+1} - \left[\frac{1730.63}{8.0713 - \log_{10}\left(7.0063 P_i^{n+1}\right)} + 39.724\right] = f_6 \tag{5.30}$$

Equlibrium adsorption capacity:

$$X_{\infty_i}^{n+1} - 0.346 \exp\left[-5.6\left(T_{s_i}^{n+1}/T_{sat_i}^{n+1} - 1\right)^{1.6}\right] = f_7 \tag{5.31}$$

Internal mass transfer coefficent:

$$k_{m_i}^{n+1} - \frac{15}{r_p^2} D_o \exp\left(-E_a/RT_{s_i}^{n+1}\right) = f_8 \tag{5.32}$$

Amount adsorbed:

$$\frac{X_i^{n+1} - X_i^n}{\Delta t} - k_{m_i}^{n+1}\left(X_{\infty_i}^{n+1} - X_i^{n+1}\right) = f_9 \tag{5.33}$$

Specific heat of the solid-gas phase mixture:

$$c_{ms_i}^{n+1} - \rho_s\left(1 - \epsilon_t\right)\left[c_{ps} + X_i^{n+1} c_{pg}\right] = f_{10} \tag{5.34}$$

Reynolds number:

$$Re_{d_i}^{n+1} - \frac{\rho_i^{n+1} v_{r_i}^{n+1} d_p}{\mu_g} = f_{11} \tag{5.35}$$

Convective heat transfer coefficient between the phases:

$$h_{gs_i}^{n+1} - \frac{K_g}{d_p}\left(2 + 1.8Pr^{0.33}\left(Re_{d_i}^{n+1}\right)^{0.5}\right) = f_{12} \tag{5.36}$$

Heat of adsorption:

$$Q_{ad_i}^{n+1} - 3500 + 13400X_i^{n+1} = f_{13} \quad \text{for} \quad X_i^{n+1} \leq 0.05$$

$$Q_{ad_i}^{n+1} - 2950 + 1400X_i^{n+1} = f_{13} \quad \text{for} \quad X_i^{n+1} > 0.05 \tag{5.37}$$

These result in thirteen equations in thirteen unknowns, namely, ρ_g, v_r, T_g, T_s, P, T_{sat}, X_∞, k_m, X, c_{ms}, Re_d, h_{gs}, Q_{ad}. The Newton-Raphson iteration scheme and a block tridiagonal matrix algorithm (Thomas algorithm) were employed to solve the resulting highly nonlinear algebraic equations iteratively. Thirty five grid points including boundaries in the radial direction and a five seconds time step were chosen and these values were checked in terms of numerical accuracy. The Newton-Raphson iteration scheme is defined as follow for the solution of the set of nonlinear algebraic equations at each grid points [72].

$$f_1\left(x_1, x_2, \ldots x_{13}\right) = 0,$$

$$f_2\left(x_1, x_2, \ldots x_{13}\right) = 0,$$

$$\vdots$$

$$f_{13}\left(x_1, x_2, \ldots x_{13}\right) = 0. \tag{5.38}$$

If we denoted the k^{th} iterate of the j^{th} variable by x_j^k, and its associated error by δ_j^k, then the

Newton-Raphson iteration scheme becomes

$$\begin{pmatrix} \frac{\partial f_1}{\partial x_1} & \frac{\partial f_1}{\partial x_2} & \cdots & \frac{\partial f_1}{\partial x_{13}} \\ \frac{\partial f_2}{\partial x_1} & \frac{\partial f_2}{\partial x_2} & \cdots & \frac{\partial f_2}{\partial x_{13}} \\ \vdots & \vdots & \ddots & \vdots \\ \frac{\partial f_{13}}{\partial x_1} & \frac{\partial f_{13}}{\partial x_2} & \cdots & \frac{\partial f_{13}}{\partial x_{13}} \end{pmatrix} \begin{pmatrix} \delta_1^k \\ \delta_2^k \\ \vdots \\ \delta_{13}^k \end{pmatrix} = - \begin{pmatrix} f_1 \\ f_2 \\ \vdots \\ f_{13} \end{pmatrix}$$

The algebraic system resulting from the Newton-Raphson iteration scheme for the general point can be represented in the matrix form as

$$[A]\,\delta_{j,i-1}^k + [B]\,\delta_{j,i}^k + [C]\,\delta_{j,i+1}^k = F_i^k \tag{5.39}$$

The above matrix falls into a following block tridiagonal structure and can be expressed in the general form $[M][X] = [D]$, when the entire system of equations for a given problem is assembled and boundary conditions are taken into account. In the block tridiagonal structure, the individual submatrix blocks of the coefficent matrix $[M]$ are 13x13 matrices and each component of the column vectors $[X]$ and $[D]$ becomes the thirteen components of $\delta_{j,i}^k$ and F_i^k associated with the point i.

$$\begin{pmatrix} B1 & C1 & & & \\ A2 & B2 & C2 & & \\ & \ddots & \ddots & \ddots & \\ & & A_{N-1} & B_{N-1} & C_{N-1} \\ & & & A_N & B_N \end{pmatrix}^k \begin{pmatrix} X_1 \\ X_2 \\ \vdots \\ X_{N-1} \\ X_N \end{pmatrix}^k = - \begin{pmatrix} D_1 \\ D_2 \\ \vdots \\ D_{N-1} \\ D_N \end{pmatrix}^k$$

where the unknown variables at time level $(n+1)$ in the matrix and the right hand side vector are evaluated using the initial guess values for the first iterate or previously computed values for the next iterate.

Matrix $[M]$ is a tridiagonal matrix and can be solved with Thomas algorithm [73]. In this algorithm, the system of equations is first put into upper triangular form by replacing the diagonal elements B_i with

$$B_i - \frac{A_i}{B_{i-1}} C_{i-1} \quad \text{for} \quad i = 2....N \tag{5.40}$$

and the D_i with

$$D_i - \frac{A_i}{B_{i-1}} D_{i-1} \quad \text{for} \quad i = 2....N \tag{5.41}$$

The unknowns are then computed using back substitution starting with

$$X_N = \frac{D_N}{B_N} \tag{5.42}$$

and continuing with

$$X_i = \frac{D_i - C_i X_{i+1}}{B_i} \quad \text{for} \quad i = N-1, N-2, ...1 \tag{5.43}$$

A computer simulation program based on the numerical procedure above was written in Matlab to perform the parametric investigation. In the simulation program, at each time step, iterations were terminated when the calculated difference between two successive iterations of any dependent variable was less than 10^{-6}. This means that

$$\left| x_{j,i}^{k+1} - x_{j,i}^{k} \right| = \left| \delta_{j,i}^{k} \right| < 10^{-6} \tag{5.44}$$

The main simulation parameters used in the computer simulation program are given in Table 5.1. The initial temperatures for the gas and solid phases were calculated by means of the generation (hot) temperature of the adsorbent bed (T_h), condenser pressure (P_c), and evaporator pressure (P_{ev}). The adsorption capacity of the solid adsorbent was assumed to be constant as the pressure inside the adsorbent bed was decreased from the condenser to the evaporator pressure.

Table 5.1: Base case simulation parameters for 1-D study.

Parameter	Value	Unit	Reference
ϵ_b	0.37		[62]
ϵ_p	0.42		[62]
d_p	$3.2e^{-3}$	m	[38]
μ_g	$1.5e^{-5}$	$\mathrm{kgm^{-1}s^{-1}}$	[46]
ρ_s	670	$\mathrm{kgm^{-3}}$	[38]
c_{ps}	880	$\mathrm{Jkg^{-1}K^{-1}}$	[38]
c_{pg}	1840	$\mathrm{Jkg^{-1}K^{-1}}$	[39]
D_o	$2.54e^{-4}$	$\mathrm{m^2s^{-1}}$	[69]
E_a	$4.2e^4$	$\mathrm{Jmol^{-1}}$	[69]
k_g	0.0196	$\mathrm{Wm^{-1}K^{-1}}$	[38]
k_s	0.198	$\mathrm{Wm^{-1}K^{-1}}$	[38]
σ	2.641	A	[38]
Ω	2.236		[38]
d_{pore}	$2e^{-9}$	m	[38]
τ	3		[38]
R_o	36.5	mm	
R_i	9.5	mm	
P_{ev}	1.228	kPa	
P_c	4.246	kPa	
T_b	30	°C	
T_h	120	°C	

5.5 RESULTS AND DISCUSSION

The effects of the diameter of the adsorbent particles, bed thickness, total porosity and thermal conductivity of the adsorbent material on the transient distributions of the temperature difference between the gas and solid phases, the pressure, the amount adsorbed calculated from the equilibrium and LDF models with the internal mass transfer coefficient have been investigated numerically and the results are presented below.

5.5.1 Temperature difference between the solid and gas phases

Typically local thermal equilibrium between the vapor and solid phases has been assumed when investigating the dynamic behavior of the adsorbent bed of adsorption cooling systems without fully justifying the validity of this assumption. Therefore, one of the main objectives of this study is to investigate the validity of the single energy equation model that results from this assumption.

Transient temperature differences between the solid and gas phases in the radial direction are illustrated in Figure 5.2. For each plot in Figure 5.2, all parameters except for that given in the plot are equal to the base case values. Generally, the temperature difference between the two phases is negligibly small for all cases investigated. However, it may need to be taken into account in the early stages of the process. It is obvious in Figure 5.2 that, initially, there is a large temperature difference between the two phases near the outer boundary but not in the rest of the bed. However, this temperature difference decreases near the outer boundary and slightly increases in the rest of the bed up to a certain point in time and then it decreases gradually throughout the bed as time progresses. As a result, the temperature difference between the phases become less than 0.5 °C when the time is equal to 1860, 1680, 780 and 420 seconds for deviations from the base case conditions as $\epsilon_t = 0.826$, $d_p = 8$ mm, $k_s = 0.1$ Wm^{-1}K^{-1} and $R_o - R_i = 13.5$ mm, respectively. The reason behind this behavior may be explained by the fact that, unlike for the solid phase, the gas phase temperature undergoes a sudden drop near the outer boundary due to its low heat capacity, and this creates a large temperature difference between the two phases initially. After a short period of time, however, this temperature difference dies out.

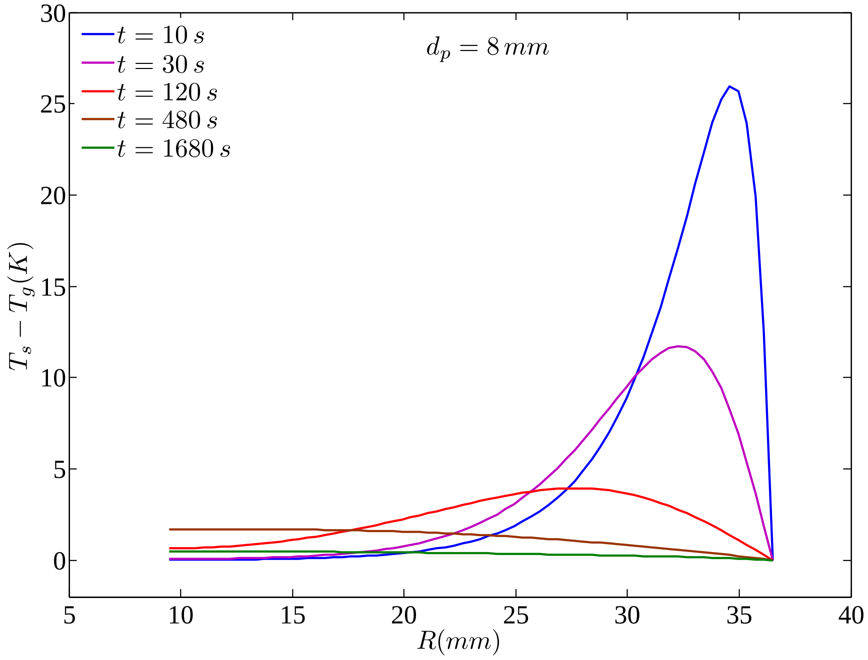

(a) d_p= 8 mm

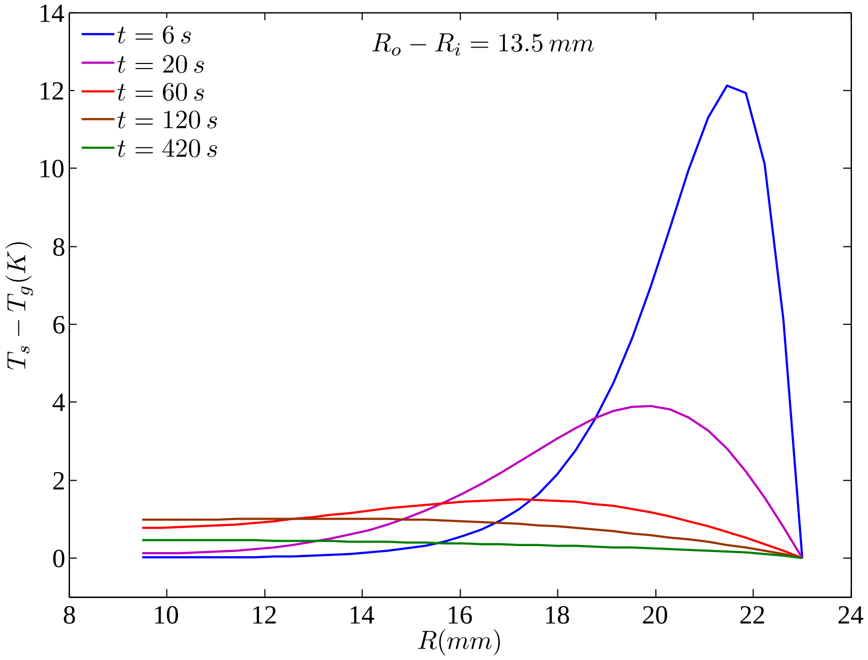

(b) $R_o - R_i$ = 13.5 mm

Figure 5.2: Transient temperature differences between the solid and gas phases in the radial direction.

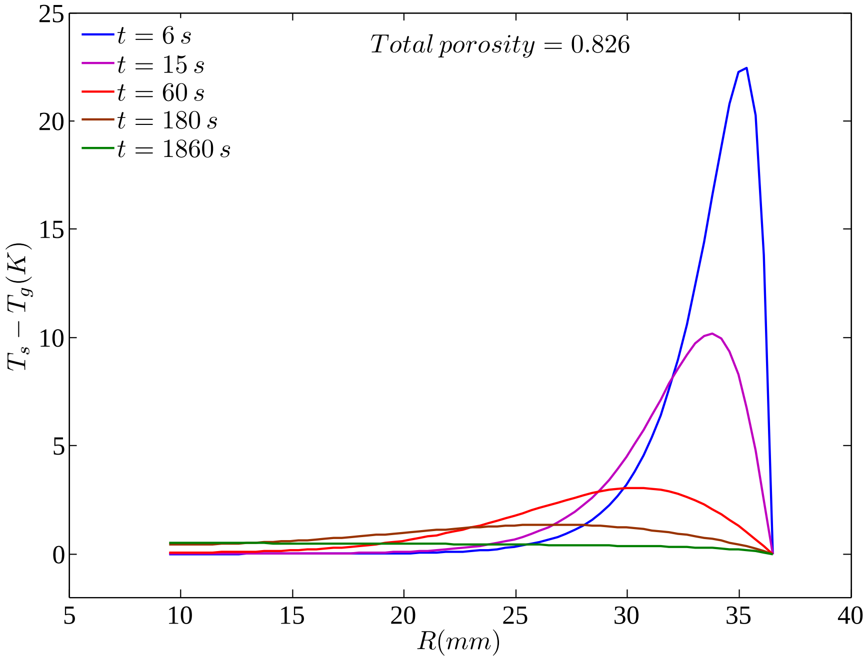

(c) Total porosity = 0.826

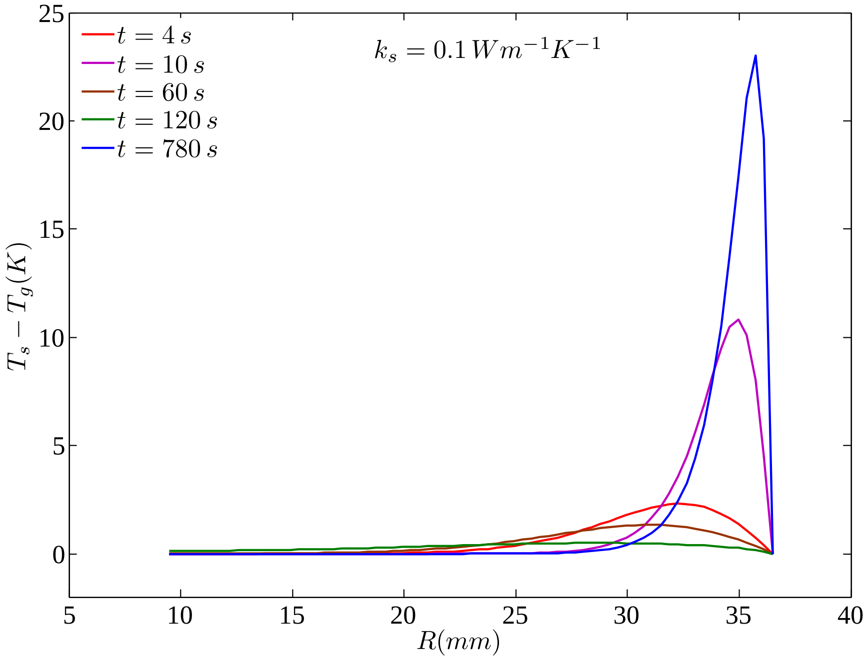

(d) k_s = 0.1 Wm^{-1}K^{-1}

Figure 5.2: Transient temperature differences between the solid and gas phases in the radial direction (cont.).

5.5.2 Effect of the adsorbent particle diameter

The effect of the diameter of the adsorbent particles on the transient solid and gas phase temperatures and pressure for the case (d_p = 8 mm, d_p = 4 mm and d_p = 2 mm) are presented in Figure 5.3. The values for all parameters except d_p are equal to their base case values given in Table 5.1. It can be seen from Figure 5.3 that the diameter of the adsorbent particles exerts considerable influence on the transient temperature distributions but only a slight influence on the pressure distribution under the given conditions. The temperature difference between the outer and inner boundaries decreases with time and this difference is comparatively high for the d_p = 2 mm case at the beginning of the process. As the particle diameter increases, the internal mass transfer resistances increases, and the adsorption rate decreases. Consequently, the rate of heat released and the temperature difference between the outer and inner boundaries decrease with increasing particle diameter. In addition, this temperature difference becomes less than 5 °C for times greater than 65, 291 and 225 minutes for particle diameter of 8, 4 and 2 mm, respectively.

At the start of the adsorption process the pressure near the outer boundary drops sharply and goes below the evaporator pressure due to the sudden temperature drop there. This outer boundary pressure then increases and eventually reaches the value of the evaporator pressure as vapor flows from the mass transfer tube to this region. The pressure gradients in the radial direction are very small and they decrease as the particle diameter increases. This result suggests that external mass transfer resistances become insignificant as the particle diameter is increased. In other words, the bed permeability is positively influenced by increasing particle diameter. The uniform pressure assumption is valid for all cases considered, especially when the particle diameter is greater than 2 mm.

Transient distributions of the amount adsorbed calculated using the equilibrium and LDF models with mass transfer coefficients through the bed for d_p = 8 mm, d_p = 4 mm and d_p = 2 mm are illustrated in Figure 5.4. It is obvious that the difference in the amount adsorbed between the equilibrium and LDF models decreases with decreasing particle diameter. The reason behind this behavior is that the internal mass transfer coefficient increases when the particle diameter is decreased and this causes an increase in the rate of adsorption according to the LDF model. In addition, the gradient in the amount adsorbed across the bed for both models increases with the decreasing particle diameter. As noted above and according to the

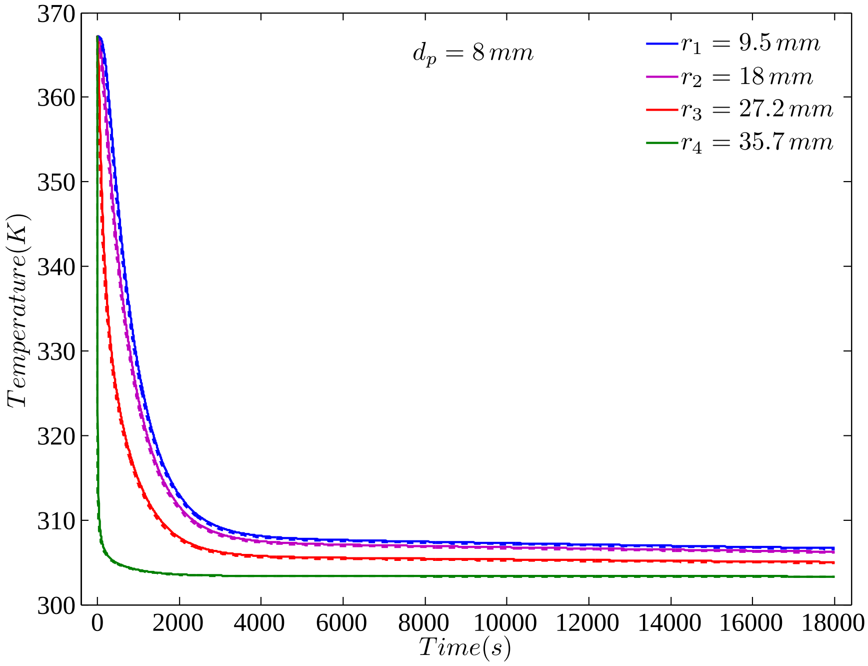

(a) d_p= 8 mm

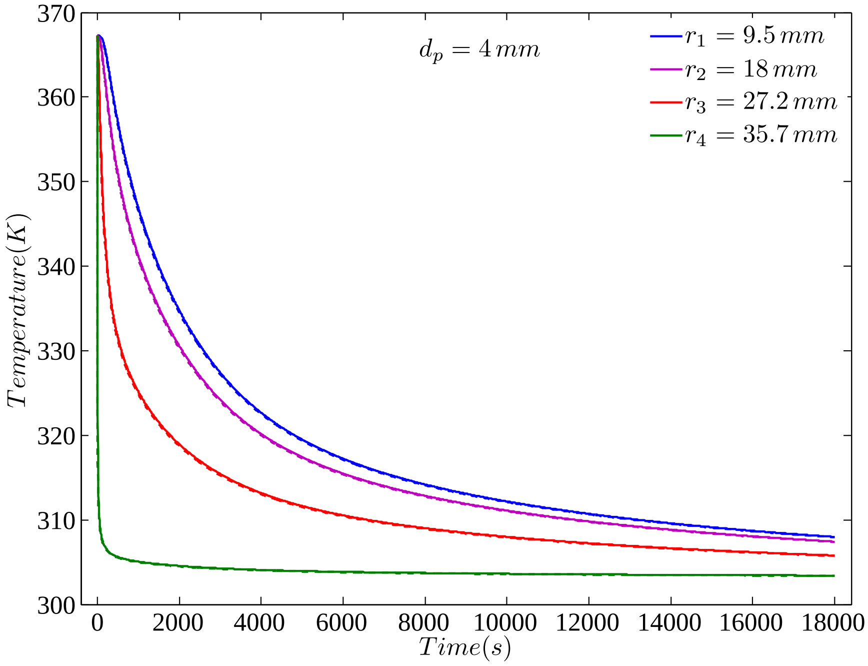

(b) d_p= 4 mm

Figure 5.3: Transient temperature of solid and gas phase and pressure distributions for various adsorbent particle diameters.(Temperature: solid lines = T_s; dashed lines = T_g. Pressure: solid lines for d_p = 2 mm; dashed lines for d_p = 4 mm; and, square dots d_p = 8 mm).

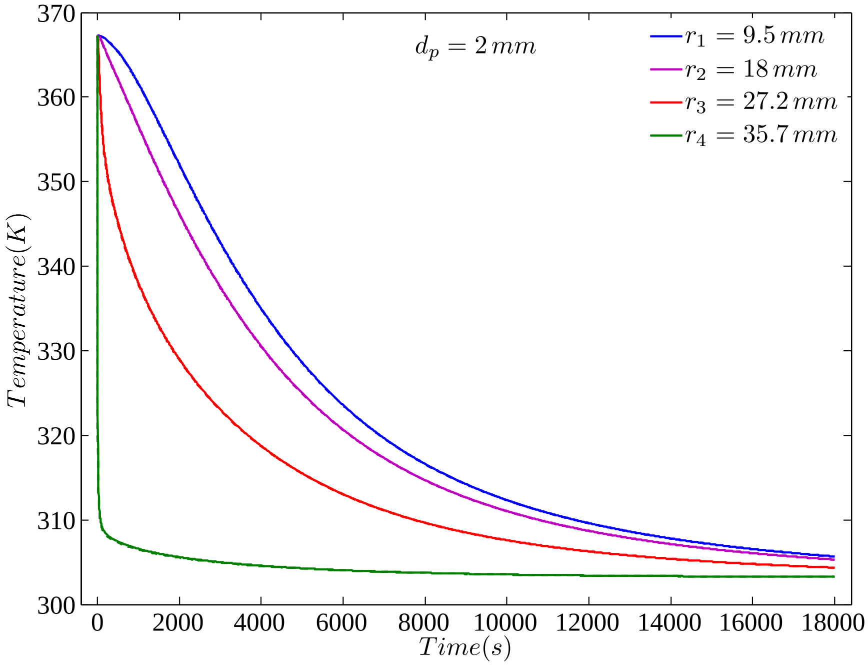

(c) d_p= 2 mm

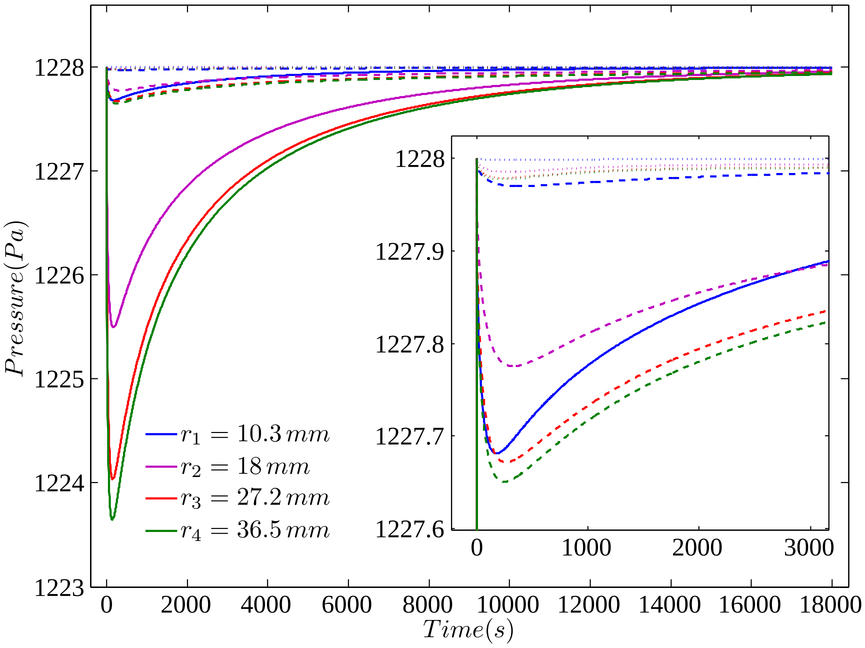

(d) Pressure

Figure 5.3: Transient temperature of solid and gas phase and pressure distributions for various adsorbent particle diameters.(Temperature: solid lines = T_s; dashed lines = T_g. Pressure: solid lines for d_p = 2 mm; dashed lines for d_p = 4 mm; and, square dots d_p = 8 mm)(cont.).

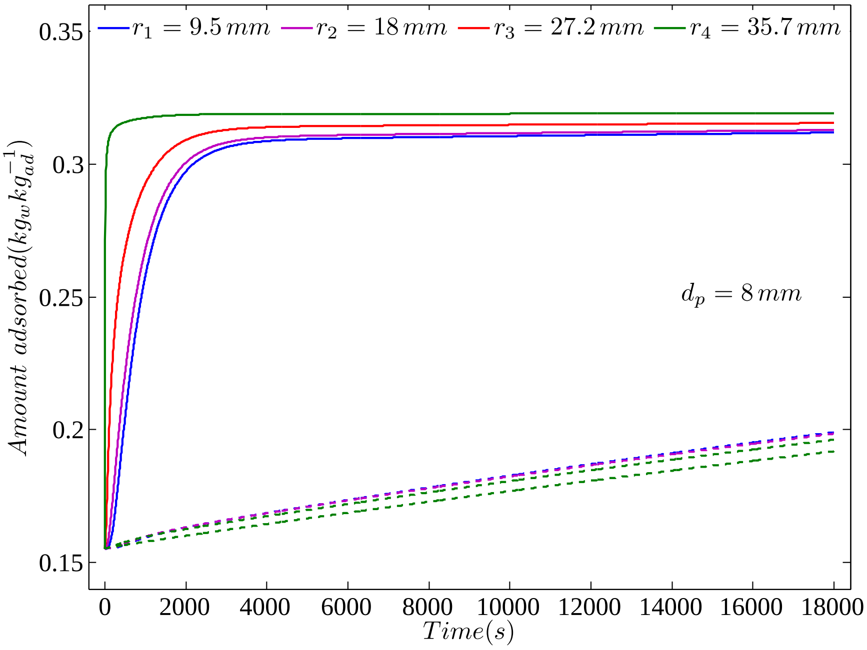

(a) d_p= 8 mm

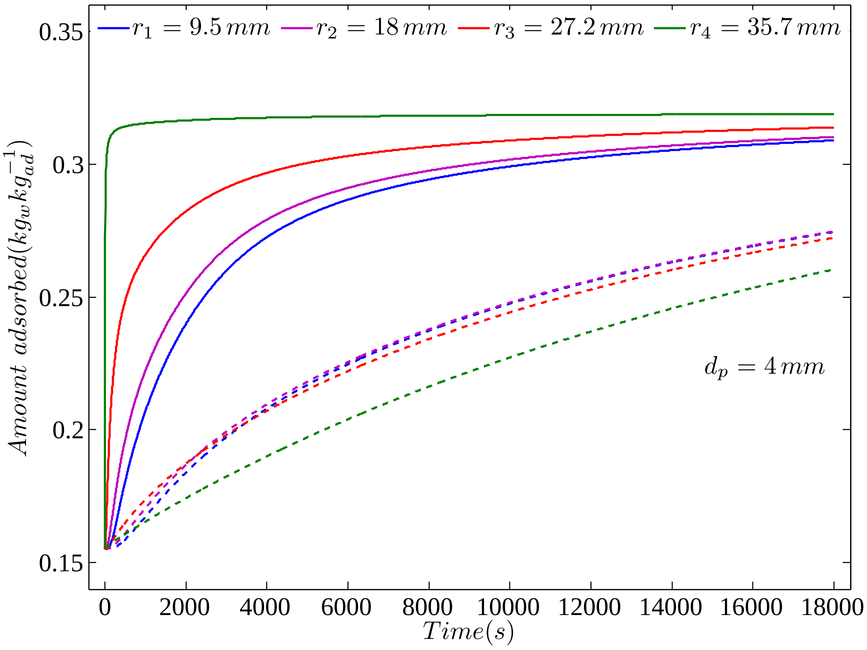

(b) d_p= 4 mm

Figure 5.4: Transient amount adsorbed and internal mass transfer coefficient distributions for various adsorbent particle diameters (Amount adsorbed: solid lines = X_∞; dashed lines = X. Internal mass transfer coefficient: solid lines for d_p = 2 mm; dashed lines for d_p = 4 mm; and, square dots for d_p = 8 mm).

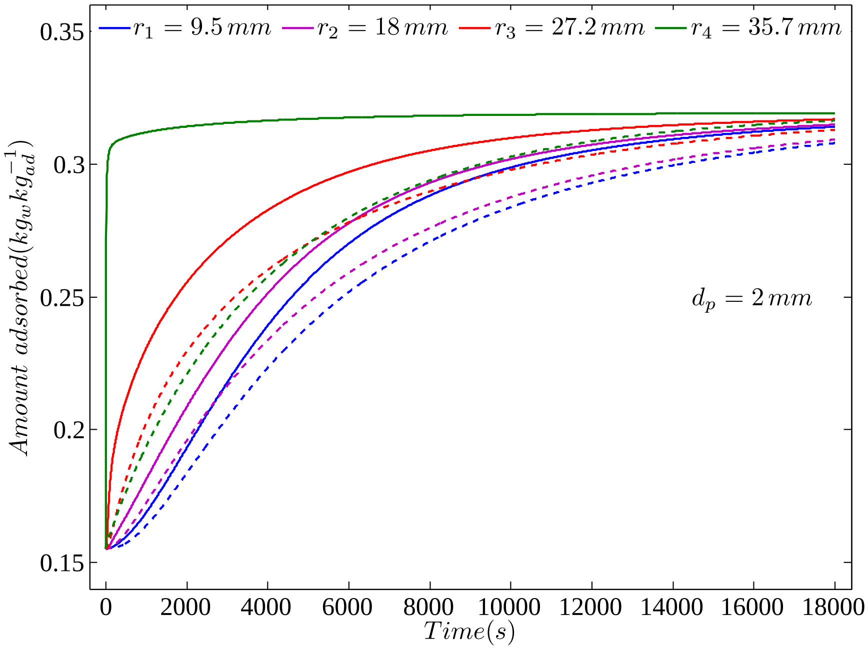

(c) d_p= 2 mm

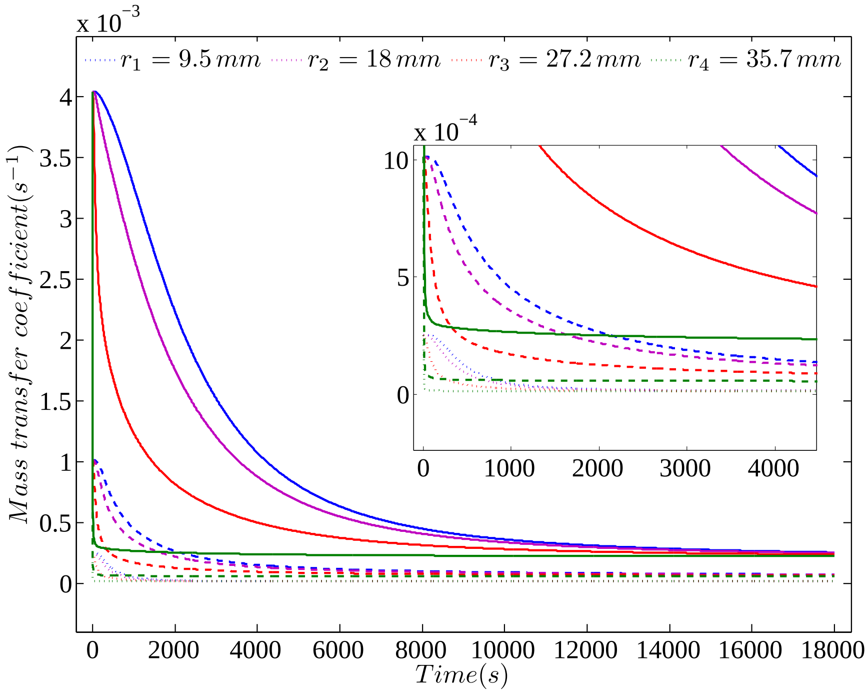

(d) Internal mass transfer coefficient

Figure 5.4: Transient amount adsorbed and internal mass transfer coefficient distributions for various adsorbent particle diameters (Amount adsorbed: solid lines = X_∞; dashed lines = X. Internal mass transfer coefficient: solid lines for d_p = 2 mm; dashed lines for d_p = 4 mm; and, square dots for d_p = 8 mm)(cont.).

LDF model, smaller particles have faster adsorption response rates, which results in these particles having higher rates of heat being released during adsorption, and larger temperature and pressure gradients. As the particle size becomes sufficiently small the adsorption rates become sufficiently fast that the predictions of the LDF model approach that of an equilibrium model. As a result, if the particle diameter is greater than 2 mm the use of the equilibrium model may lead to an overestimate in the amount adsorbed by the adsorbent bed. However, even when the particle diameter is equal to 2 mm, there can still be large difference between the two models, especially near the outer boundary where the internal mass transfer coefficient is comparatively low due to low temperatures. Consequently, the internal mass transfer resistance is very sensitive to variations in the particle diameter and it increases with increasing particle diameter. However, the limiting effect of the external mass transfer on the bed permeability is insignificant and this can also be seen from the pressure distributions in Figure 5.3.

5.5.3 Effect of the adsorbent bed thickness

The temperatures of the solid and gas phases, the pressure, the amount adsorbed, and the internal mass transfer coefficient in the radial direction have been investigated for adsorbent bed thicknesses of 13.5, 27 (base case) and 54 mm, and the results are presented in Figures 5.5 and 5.6.

It is shown in Figure 5.5 that the temperature distributions inside the bed become almost uniform after 80 and 265 min for the 13.5 and 27 mm bed thicknesses, respectively. However, the adsorbent bed having a 54 mm bed thickness needs more than 480 min to reach a uniform temperature distribution. It may be concluded that the heat transfer in the radial direction can be enhanced by decreasing the adsorbent bed thickness. The external mass transfer resistances increase with increasing bed thickness and this effect can be clearly seen from the pressure distributions in Figure 5.5. However for the conditions investigated, external mass transfer resistances do not result in significant pressure gradients and hence they may be ignored and a uniform pressure distribution throughout the bed can be assumed. The transient distribution of the amount adsorbed has been evaluated using the equilibrium and LDF models for 54, 27 and 13.5 mm bed thicknesses. It can be seen from Figure 5.6 that, for the 27 and 13.5 mm bed thicknesses, the difference in amount adsorbed between the two models at various locations

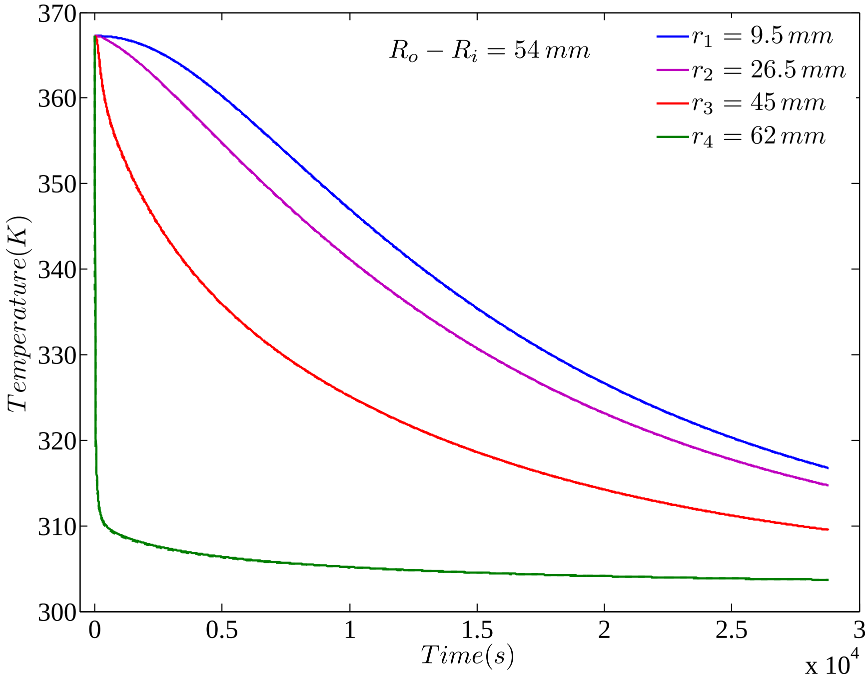

(a) $R_o - R_i$ = 54 mm

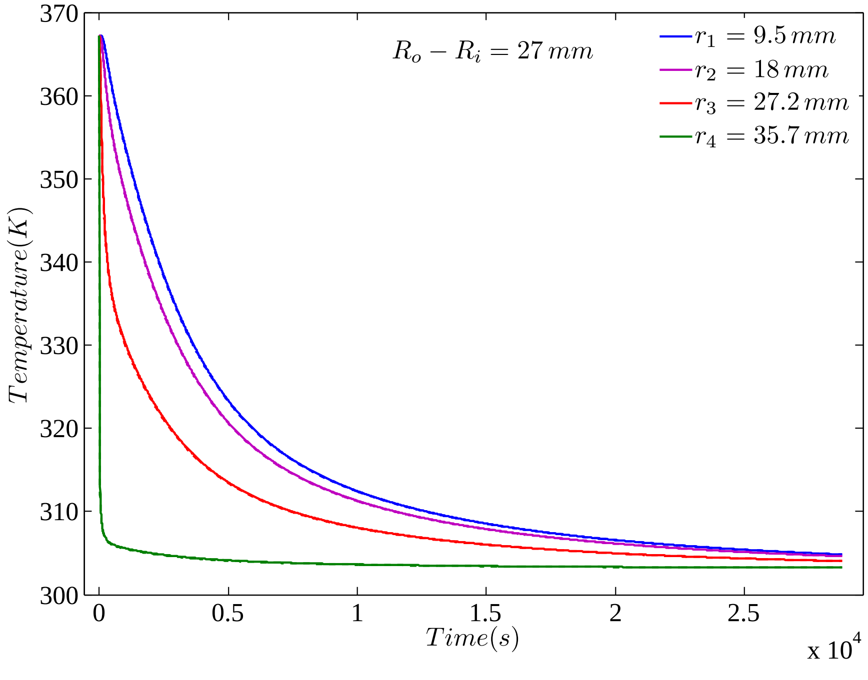

(b) $R_o - R_i$ = 27 mm

Figure 5.5: Transient temperature of solid and gas phase and pressure distributions for various adsorbent bed thicknesses (Temperature: solid lines = T_s; dashed lines = T_g. Pressure with same locations as the temperatures: solid lines for $R_o - R_i$ = 54 mm; dashed lines for $R_o - R_i$ = 27 mm; and, square dots for $R_o - R_i$ = 13.5 mm).

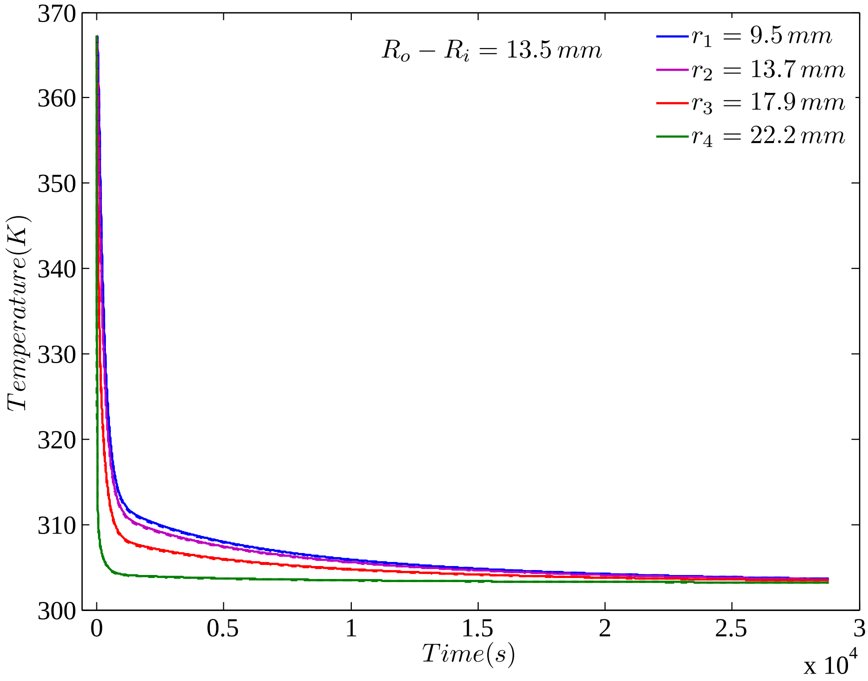

(c) $R_o - R_i = 13.5$ mm

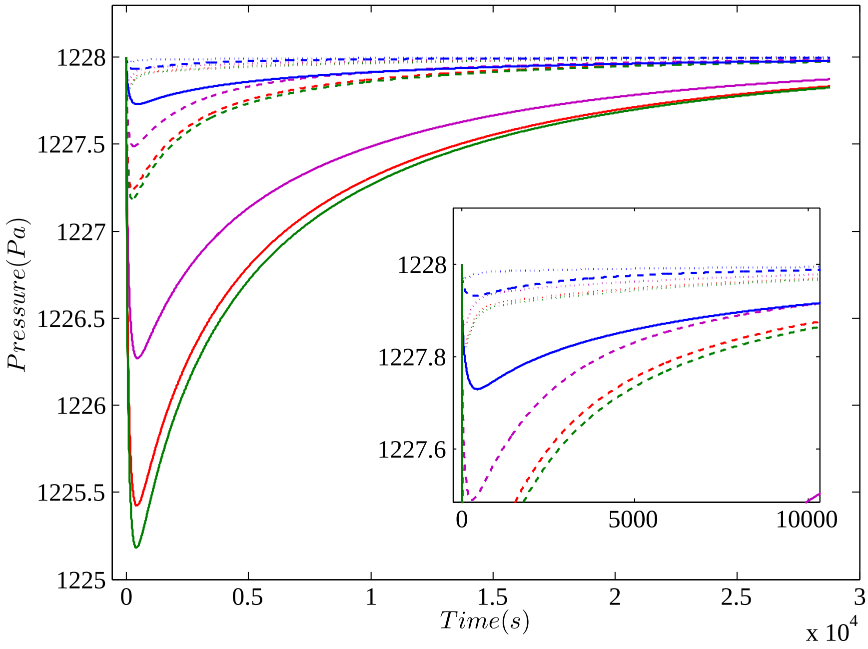

(d) Pressure

Figure 5.5: Transient temperature of solid and gas phase and pressure distributions for various adsorbent bed thicknesses (Temperature: solid lines = T_s; dashed lines = T_g. Pressure with same locations as the temperatures: solid lines for $R_o - R_i$ = 54 mm; dashed lines for $R_o - R_i$ = 27 mm; and, square dots for $R_o - R_i$ = 13.5 mm)(cont.).

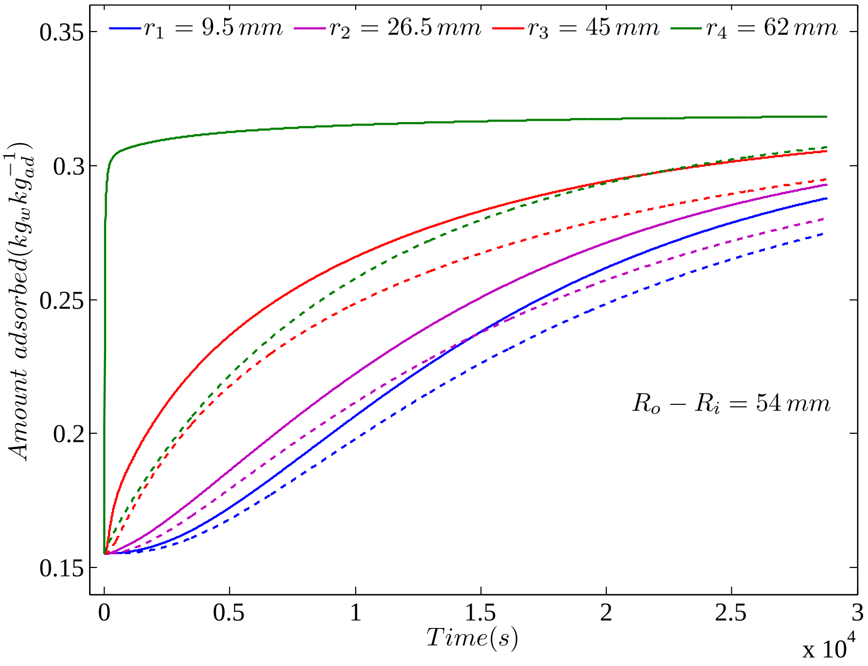

(a) $R_o - R_i = 54$ mm

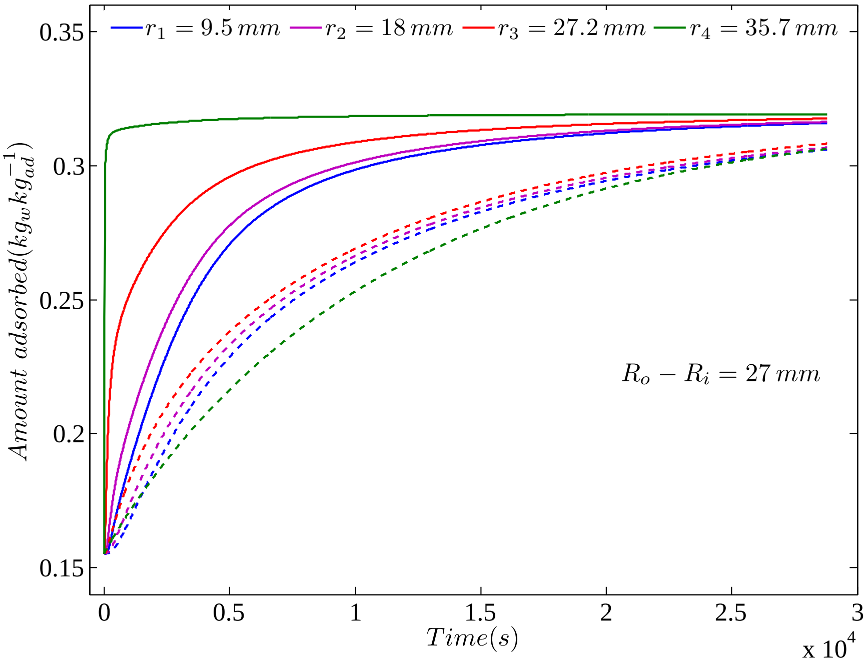

(b) $R_o - R_i = 27$ mm

Figure 5.6: Transient amount adsorbed and internal mass transfer coefficient distributions for various adsorbent bed thicknesses (Amount adsorbed: solid lines X_∞; dashed lines X. Internal mass transfer coefficient at same locations as temperature: solid lines for $R_o - R_i = 13.5$ mm; dashed lines for $R_o - R_i = 27$ mm; and, square dots for $R_o - R_i = 54$ mm).

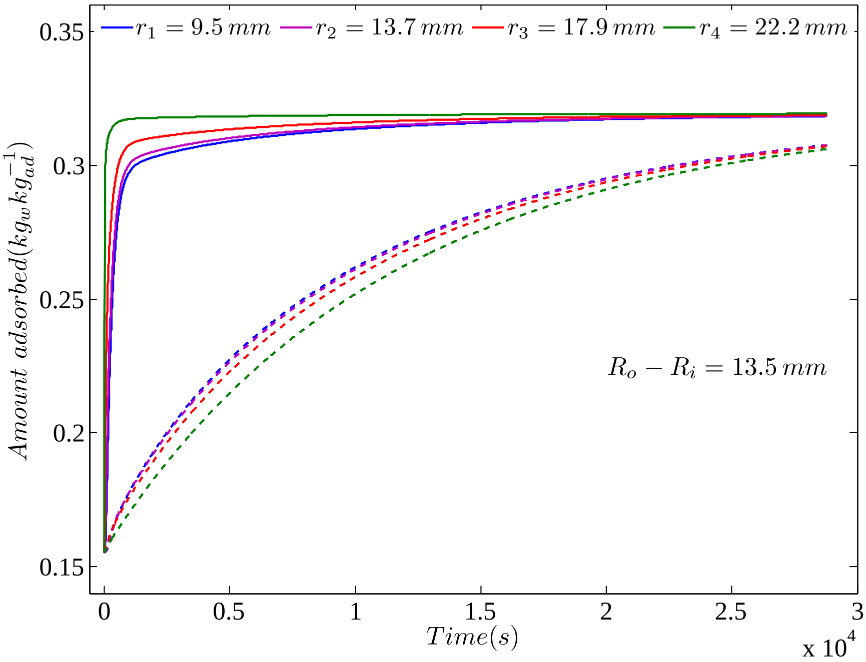

(c) $R_o - R_i$ = 13.5 mm

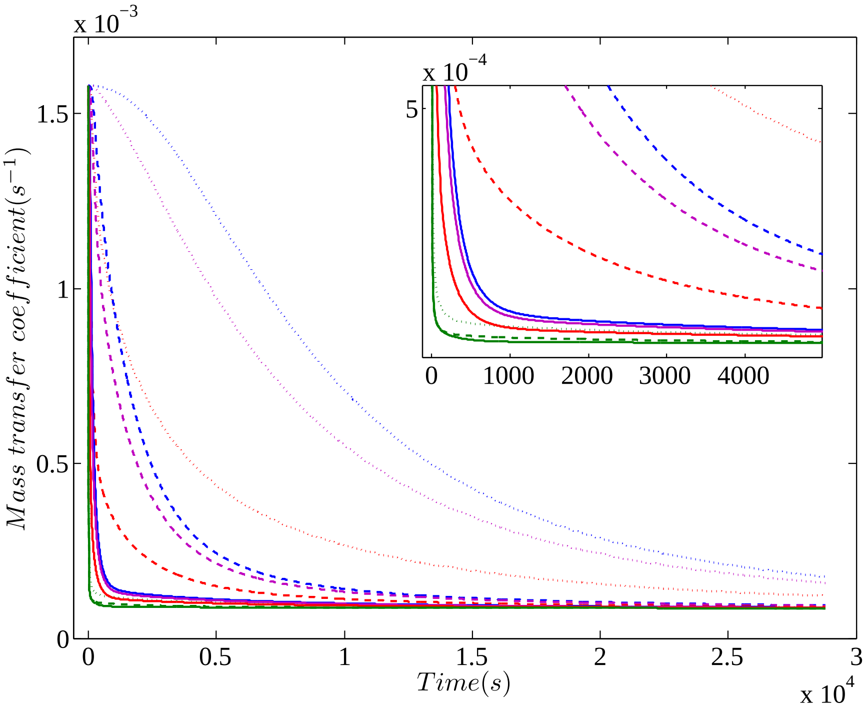

(d) Internal mass transfer coefficient

Figure 5.6: Transient amount adsorbed and internal mass transfer coefficient distributions for various adsorbent bed thicknesses (Amount adsorbed: solid lines X_∞; dashed lines X. Internal mass transfer coefficient at same locations as temperature: solid lines for $R_o - R_i$ = 13.5 mm; dashed lines for $R_o - R_i$ = 27 mm; and, square dots for $R_o - R_i$ = 54 mm)(cont.).

in the bed decreases as the process time increases and this difference becomes less than 0.02 $\mathrm{kg_w kg_{ad}^{-1}}$ after 480 min.; i.e. the adsorbent bed nearly reaches its equilibrium adsorption capacity. However, this difference increases slightly with increasing process time near the inner boundary of the bed having 54 mm bed thickness, which can be explained as follows. Initially, the two models give similar results near the inner boundary. However, when the temperature starts to decrease, the equilibrium adsorption capacity increases and the internal mass transfer coefficient decreases. As a result, the difference in rates of adsorption between the two models increases slightly. The transient distribution of amount adsorbed inside the bed for the LDF model becomes nearly uniform when the adsorbent bed thickness is decreased. It is clear in Figure 5.5 that, when the adsorbent bed thickness is decreased, the transient temperature and pressure distributions inside the bed become almost uniform in a short period of time and hence, equilibrium adsorption capacity as well. On the other hand, the LDF model is related to the equilibrium adsorption capacity and the internal mass transfer coefficient. At the same time, the internal mass transfer coefficient only varies with temperature for this case and it decreases with a decreasing temperature. As a result, the internal mass transfer coefficient and the equilibrium adsorption capacity are uniform and thus the LDF model predicts a uniform distribution of amount adsorbed when the adsorbent bed thickness is small. For large bed thicknesses the response of the bed is limited by external (interparticle) heat transfer resistances and adsorption equilibrium can be assumed at the particle level. However, for small bed thickness the response of the bed is limited by internal (intraparticle) mass transfer resistances and adsorption equilibrium cannot be assumed at the particle level. Finally, if the adsorbent bed thickness is less than 54 mm, then the use of the equilibrium adsorption model instead of the LDF model may lead to unrealistic simulation results. However, the equilibrium adsorption model may also exhibit large simulation errors near the outer boundary as the adsorbent bed thickness is greater than 54 mm for the given boundary conditions.

5.5.4 Effect of the total porosity

The transient variation of the solid and gas phase temperatures, the pressure and the amount adsorbed in the radial direction for three different values of the total porosity, 0.826, 0.652 and 0.478, are shown in Figure 5.7 and Figure 5.8. It may be seen from Figure 5.7 that adsorbent beds having a porosity of $\epsilon_t = 0.478$, $\epsilon_t = 0.652$ and $\epsilon_t = 0.826$ reaches a uniform temperature distribution (i.e the maximum temperature difference between the inner and outer boundaries is less than 4.5 °C) when the process time is equal to 300, 276, and 236 min, respectively. It can be concluded that the heat transfer conditions inside adsorbent bed are positively affected if the total porosity is increased. This is due to the fact that the total heat capacity of the solid phase decreases with an increasing total porosity and hence, the bed having a high total porosity takes less time to reach a uniform temperature distribution. However, at the same time, the heat transfer rate for the solid phase is adversely affected by an increasing total porosity due to the decrease in the bed's effective thermal conductivity. The opposite is true for the gas phase. The total porosity of the adsorbent bed has a strong influence on the bed permeability (external mass transfer resistance). The external mass transfer resistance increases strongly as the total porosity of the bed is decreased. In this case, the uniform pressure assumption through the bed may not be correct and it may result in significant errors. Therefore the external mass transfer resistance should be considered for this problem when the total porosity of the adsorbent bed is less than 0.652 or the bed permeability is less than the order of 10^{-8}.

The transient distribution of amount adsorbed evaluated using both the equilibrium adsorption and LDF models with internal mass transfer coefficient for various porosities of the adsorbent bed are illustrated in Figure 5.8. The total porosity of the adsorbent bed over the range investigated has only a small effect on the transient distribution of amount adsorbed for both models. The LDF model considers the equilibrium adsorption capacity and the internal mass transfer coefficient and thus, the amount adsorbed calculated using the LDF model is naturally affected by the distribution of the equilibrium adsorption capacity and the internal mass transfer coefficient. The LDF model predicts a relatively slow adsorption rate, and therefore relative slow rate of heat released due to adsorption. Thus, the thermal and mechanical (pressure) relaxation times of the bed are relatively fast relative to the adsorption relaxation time, which result in relatively uniform temperature and pressure distributions within the bed, and consequently relatively uniform distribution of amount adsorbed. The amount adsorbed from the inner boundary to the outer boundary increases for the equilibrium adsorption model because of significant temperature gradients. However, this is not true near the outer boundary for the LDF model because the internal mass transfer coefficient reaches its minimum value near the outer boundary due to the low temperature boundary condition and hence the amount adsorbed near the outer boundary is comparatively low. The amount adsorbed evaluated using the equilibrium adsorption model for $\epsilon_t = 0.478$ is lower than that for $\epsilon_t = 0.652$ and $\epsilon_t =$

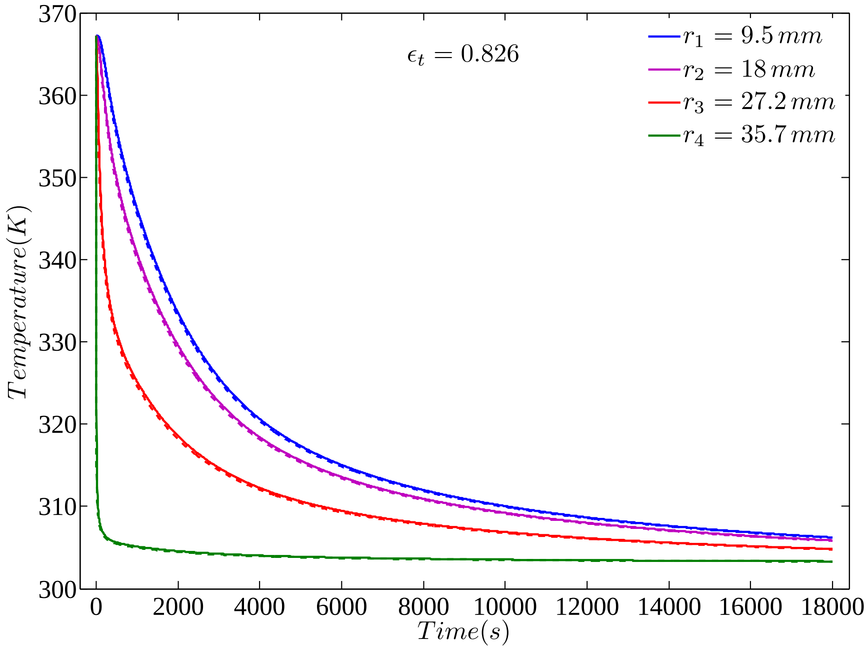

(a) $\epsilon_t = 0.826$

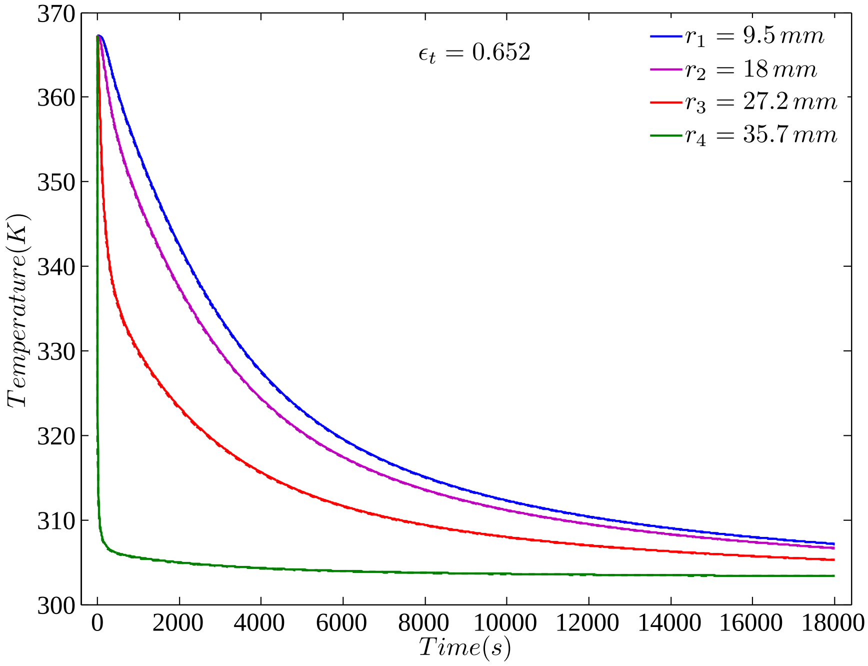

(b) $\epsilon_t = 0.652$

Figure 5.7: Transient temperature of solid and gas phase and pressure distributions for various total porosities of the adsorbent bed (Temperature: solid lines = T_s; dashed lines = T_g. Pressure: solid lines for $\epsilon_t = 0.478$; dashed lines for $\epsilon_t = 0.652$; and square dots for $\epsilon_t = 0.826$).

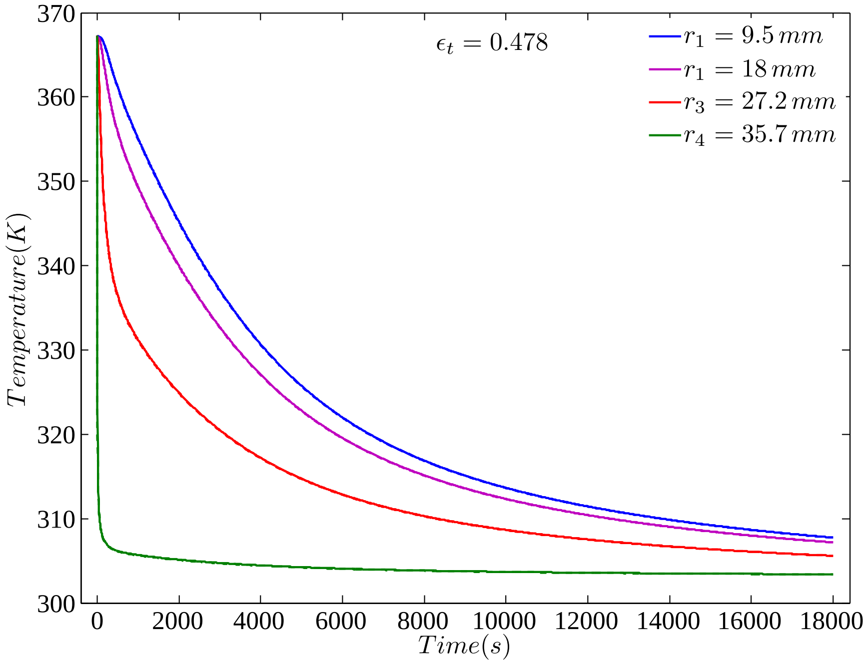

(c) $\epsilon_t = 0.478$

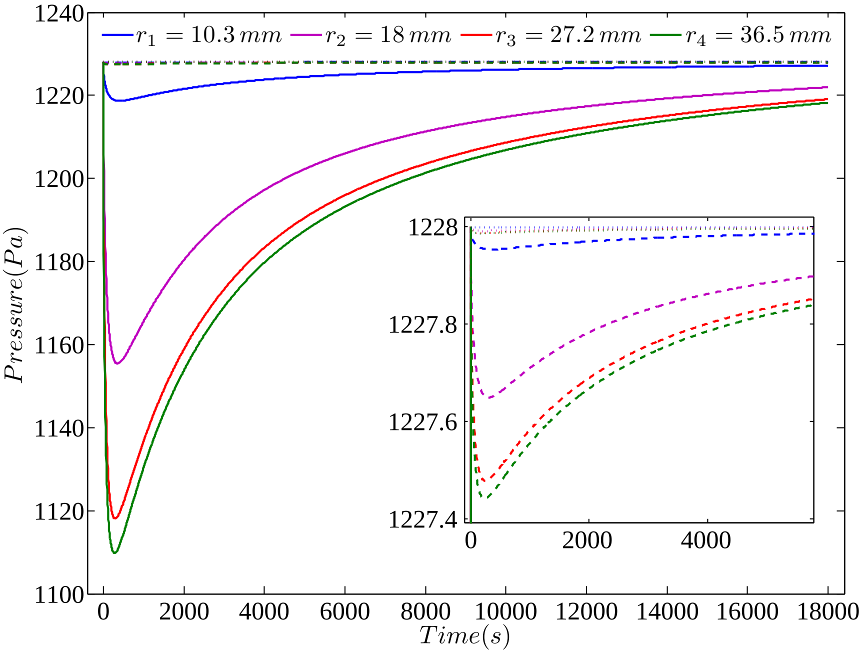

(d) Pressure

Figure 5.7: Transient temperature of solid and gas phase and pressure distributions for various total porosities of the adsorbent bed (Temperature: solid lines = T_s; dashed lines = T_g. Pressure: solid lines for ϵ_t = 0.478; dashed lines for ϵ_t = 0.652; and square dots for ϵ_t = 0.826)(cont.).

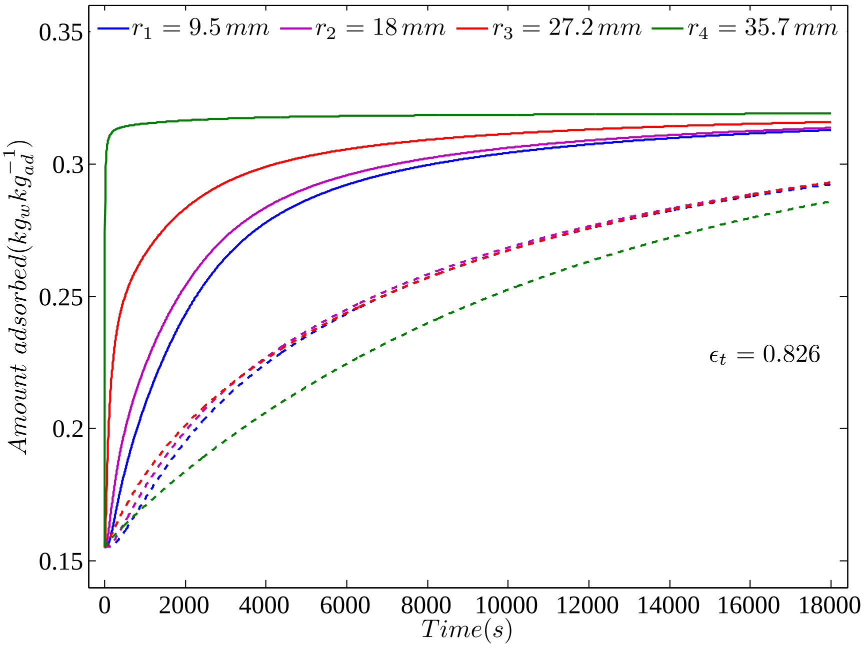

(a) $\epsilon_t = 0.826$

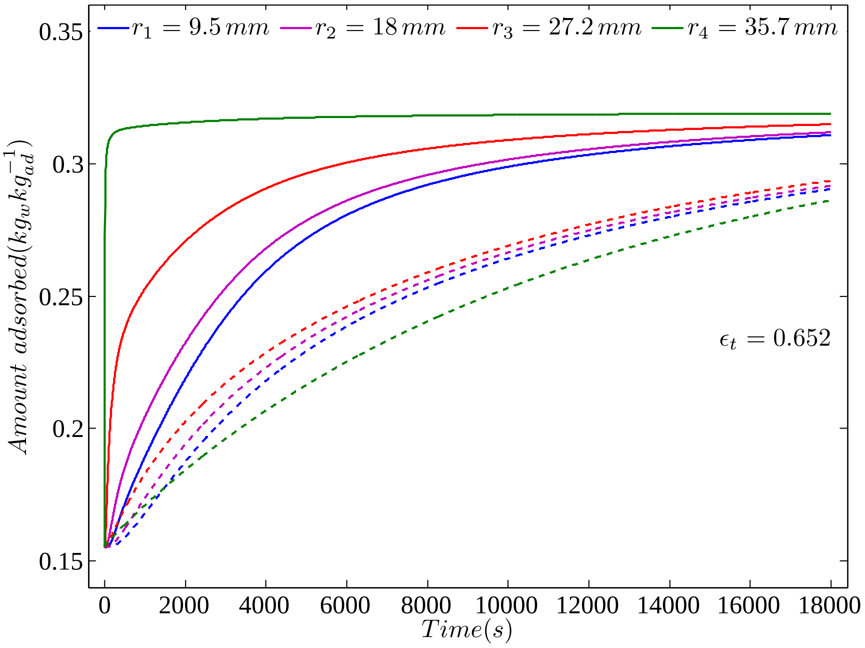

(b) $\epsilon_t = 0.652$

Figure 5.8: Transient amount adsorbed and internal mass transfer coefficient distributions for various adsorbent bed porosities (Amount adsorbed: solid lines = X_∞; dashed lines = X. Internal mass transfer coefficient: solid lines for ϵ_t = 0.478; dashed lines for ϵ_t = 0.652; and square dots for ϵ_t = 0.826).

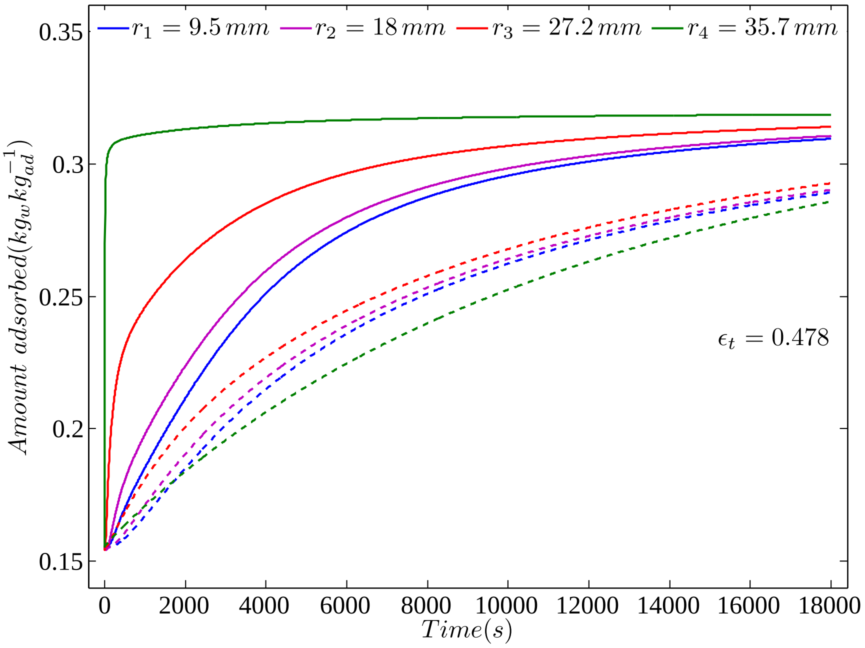

(c) $\epsilon_t = 0.478$

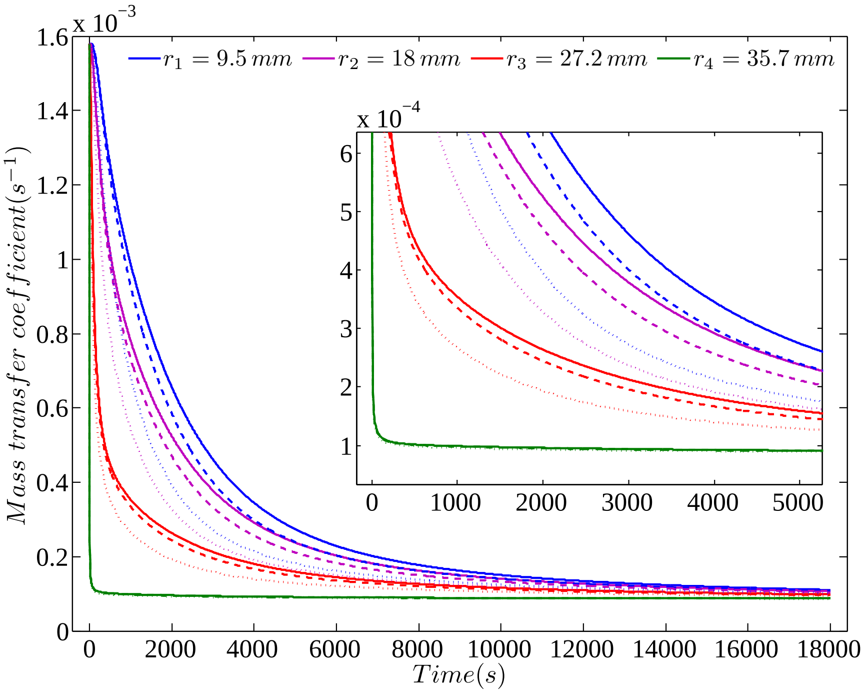

(d) Internal mass transfer coefficient

Figure 5.8: Transient amount adsorbed and internal mass transfer coefficient distributions for various adsorbent bed porosities (Amount adsorbed: solid lines = X_∞; dashed lines = X. Internal mass transfer coefficient: solid lines for $\epsilon_t = 0.478$; dashed lines for $\epsilon_t = 0.652$; and square dots for $\epsilon_t = 0.826$)(cont.).

0.826 due to the comparatively low pressures and large temperature gradients inside the bed. Consequently, the LDF model for $\epsilon_t = 0.478$ estimates the amount adsorbed as being slightly lower than for $\epsilon_t = 0.652$ and $\epsilon_t = 0.826$ even though its internal mass transfer resistance is relatively high. The adsorption rate predicted by the equilibrium model decreases with decreasing total bed porosity due to the increasing importance of external (interparticle) mass transfer resistances. According to the LDF model, internal mass transfer resistances are large relative to external mass transfer resistances, and therefore adsorption rates are relatively insensitive to changes in total bed porosity if the particle porosity is held constant. As result, the difference between these two models decreases as the total bed porosity decreases. However, for all cases investigated the difference between these two models is still high and thus internal mass transfer resistances should be taken into account.

5.5.5 Effect of the thermal conductivity of the solid phase

The effect of the thermal conductivity of the solid phase on the transient distributions of solid and gas phase temperatures and the amount adsorbed is shown in Figure 5.9 and Figure 5.10, respectively. The heat transfer rate inside the adsorbent bed is influenced strongly by the solid phase thermal conductivity. It is very obvious in Figure 5.9 that after 10 min the temperature difference between the inner and outer boundaries of the bed is less than 10 °C when $k_s = 1$ $\mathrm{Wm^{-1}K^{-1}}$. However, this time becomes 55 and 270 min when $k_s = 0.5$ $\mathrm{Wm^{-1}K^{-1}}$ and $k_s = 0.1$ $\mathrm{Wm^{-1}K^{-1}}$, respectively. Therefore, the heat transfer conditions of the bed can be improved considerably by reducing heat transfer resistances through the use of fins, highly conductive adsorbent materials or other heat transfer enhancement techniques. The pressure distributions for all cases are nearly uniform and thus the uniform pressure assumption is valid. That is, the effect of the thermal conductivity of the adsorbent material on the pressure distribution is negligible.

In Figure 5.10, the amount adsorbed calculated using the equilibrium adsorption model increases sharply to a maximum value (at T_b and P_{ev}) in a short period of time for $k_s = 1$ $\mathrm{Wm^{-1}K^{-1}}$ due to the high heat transfer rate and negligible pressure gradients. On the other hand, the adsorption rate for the LDF model is very slow due to the internal mass transfer resistances. Therefore, initially, there is a big difference between the equilibrium adsorption and LDF models and this difference decreases as time increases. In addition, the difference

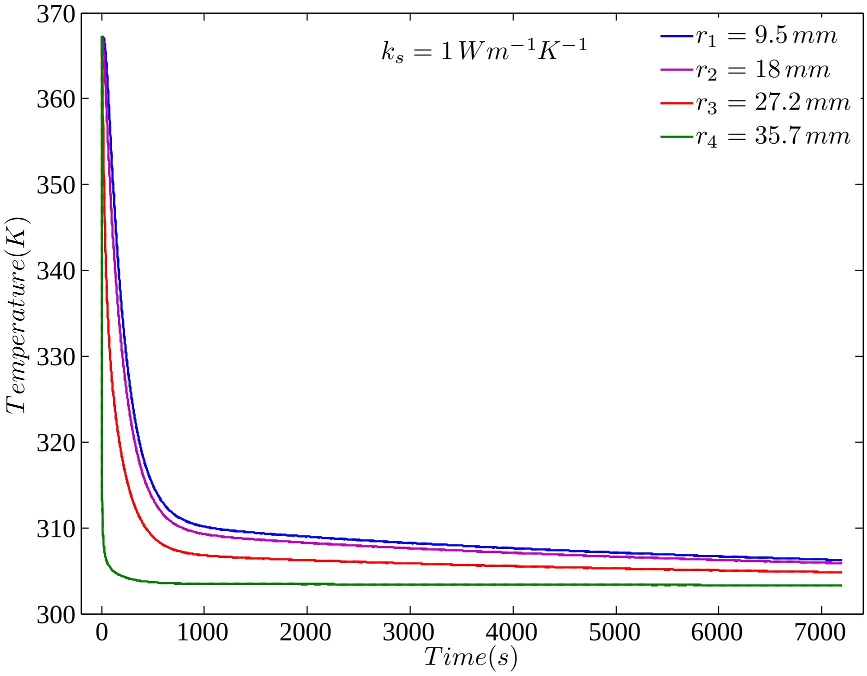

(a) k_s = 1 $\mathrm{Wm^{-1}K^{-1}}$

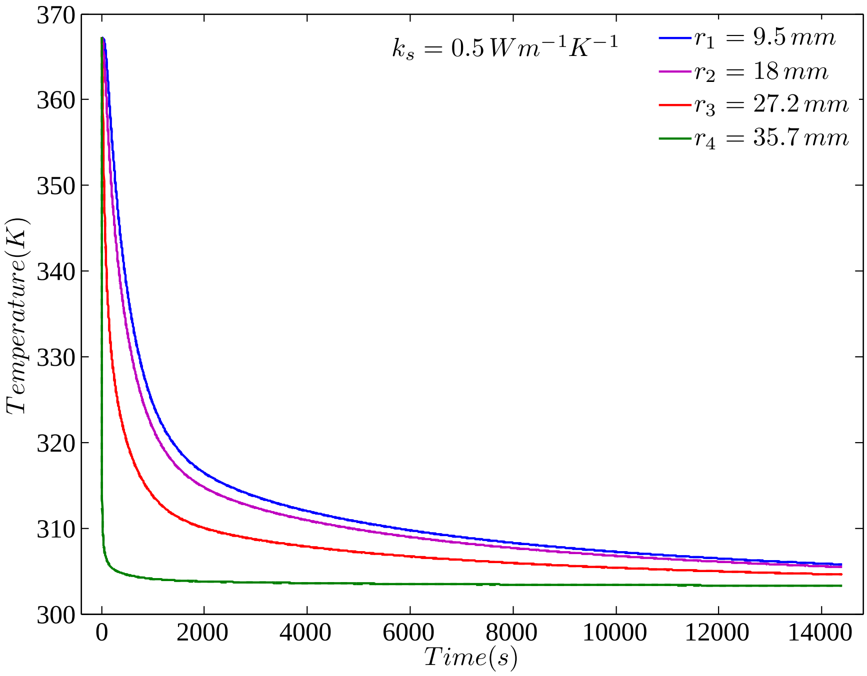

(b) k_s = 0.5 $\mathrm{Wm^{-1}K^{-1}}$

Figure 5.9: Transient temperature of solid and gas phase and pressure distributions for various thermal conductivity of the adsorbent material (Temperature: solid lines = T_s; dashed lines = T_g. Pressure: solid lines for k_s = 1 $\mathrm{Wm^{-1}K^{-1}}$; dashed lines for k_s = 0.5 $\mathrm{Wm^{-1}K^{-1}}$; and square dots for k_s = 0.1 $\mathrm{Wm^{-1}K^{-1}}$).

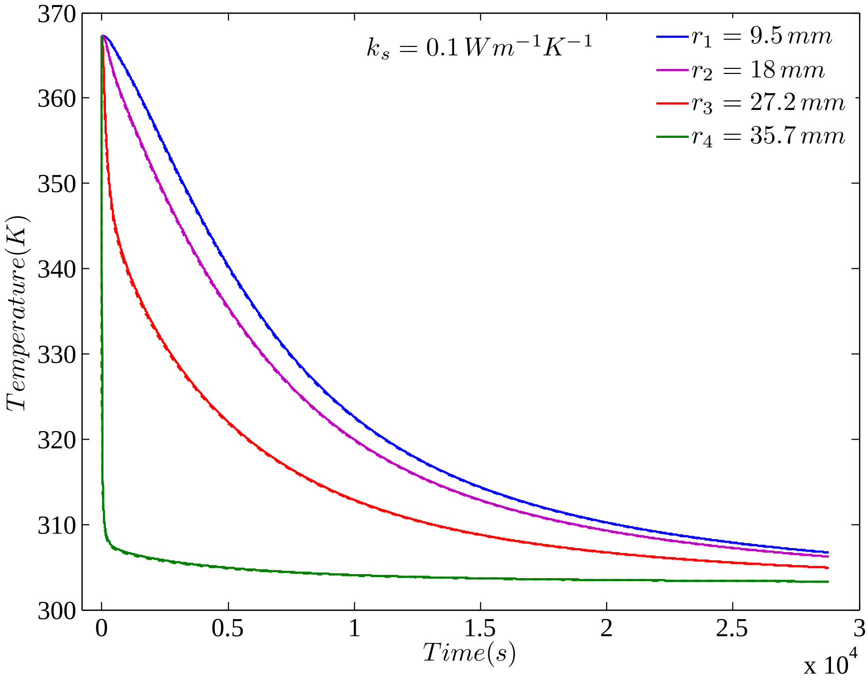

(c) $k_s = 0.1$ Wm^{-1}K^{-1}

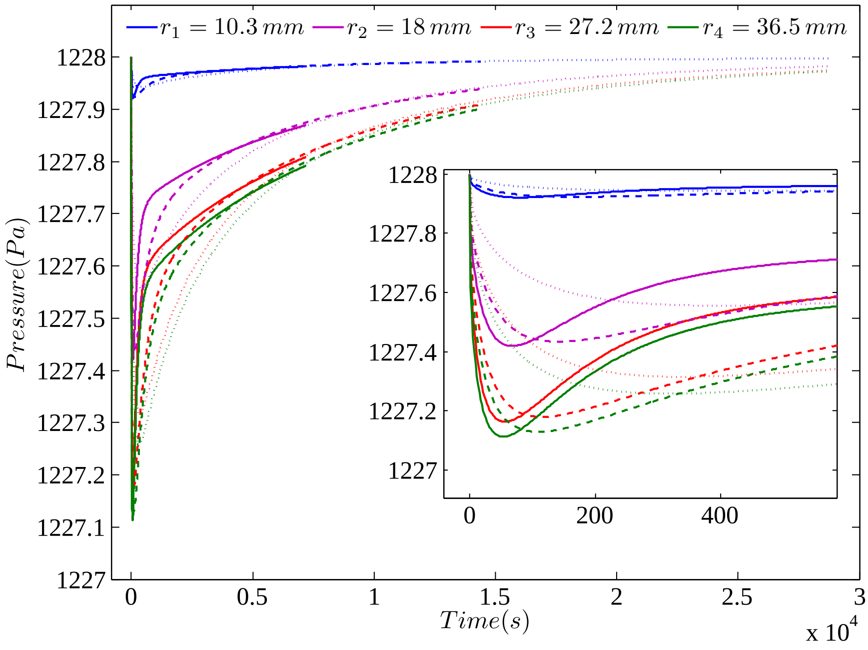

(d) Pressure

Figure 5.9: Transient temperature of solid and gas phase and pressure distributions for various thermal conductivity of the adsorbent material Temperature: solid lines = T_s; dashed lines = T_g. Pressure: solid lines for k_s = 1 Wm^{-1}K^{-1}; dashed lines for k_s = 0.5 Wm^{-1}K^{-1}; and square dots for k_s = 0.1 Wm^{-1}K^{-1})(cont.).

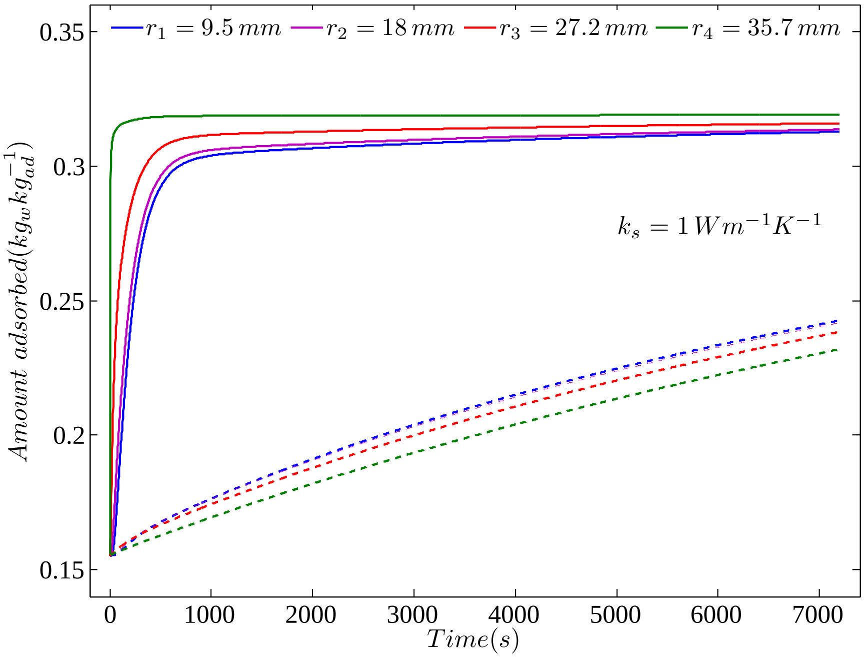

(a) k_s = 1 $\mathrm{Wm^{-1}K^{-1}}$

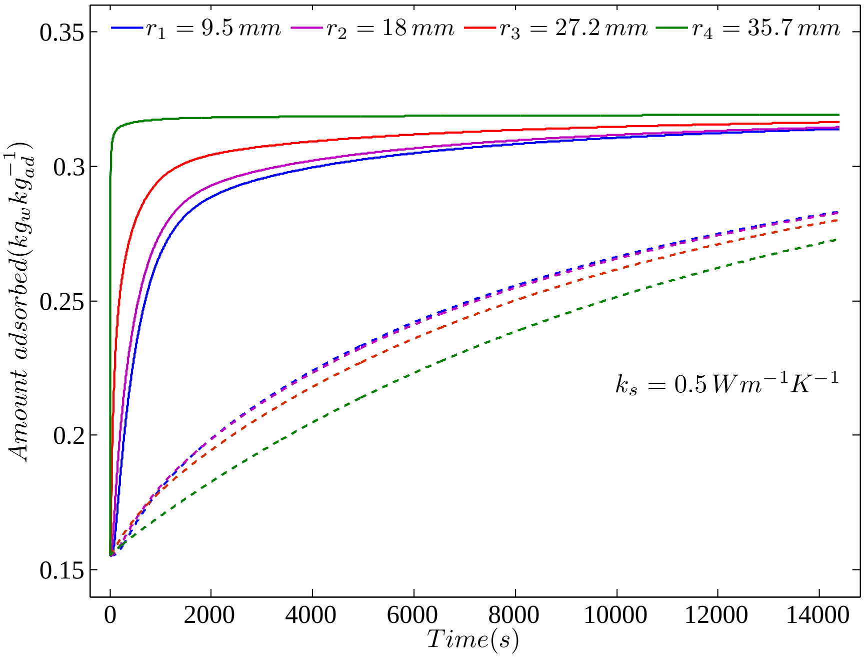

(b) k_s = 0.5 $\mathrm{Wm^{-1}K^{-1}}$

Figure 5.10: Transient amount adsorbed and internal mass transfer coefficient distributions for various thermal conductivity of the adsorbent material (Amount adsorbed: solid lines = X_∞; dashed lines = X. Internal mass transfer coefficient: solid lines for k_s = 1 $\mathrm{Wm^{-1}K^{-1}}$; dashed lines for k_s = 0.5 $\mathrm{Wm^{-1}K^{-1}}$; and square dots for k_s = 0.1 $\mathrm{Wm^{-1}K^{-1}}$).

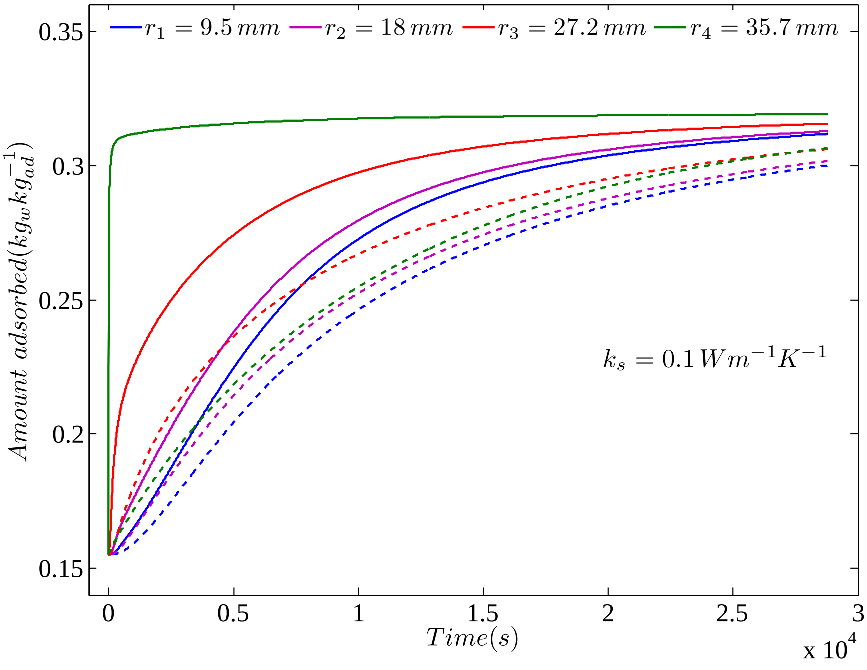

(c) k_s = 0.1 Wm^{-1}K^{-1}

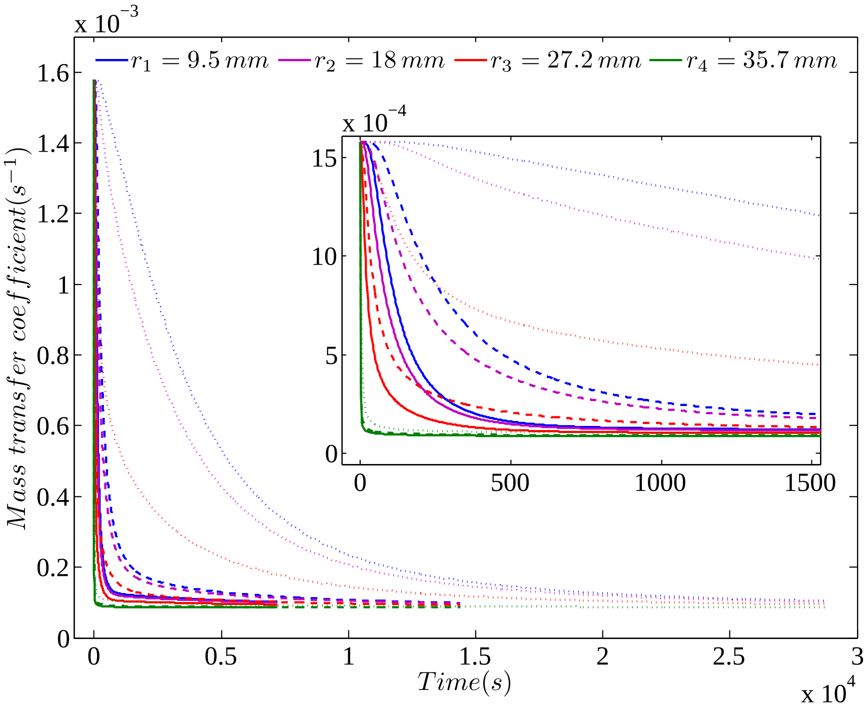

(d) Internal mass transfer coefficient

Figure 5.10: Transient amount adsorbed and internal mass transfer coefficient distributions for various thermal conductivity of the adsorbent material (Amount adsorbed: solid lines = X_∞; dashed lines = X. Internal mass transfer coefficient: solid lines for k_s = 1 Wm^{-1}K^{-1}; dashed lines for k_s = 0.5 Wm^{-1}K^{-1}; and square dots for k_s = 0.1 Wm^{-1}K^{-1})(cont.).

in the amount adsorbed between the two models decreases with decreasing thermal conductivity. However, this difference remains large near the outer boundary at the beginning of the process. It can be stated that when the thermal conductivity of adsorbent material is high, the temperature distribution becomes nearly uniform and the amount adsorbed for the equilibrium adsorption model reaches its maximum value after a short period of time, but the amount adsorbed for the LDF model takes a longer time to reach the equilibrium capacity at T_b and P_{ev}.

CHAPTER 6

TWO-DIMENSIONAL NUMERICAL STUDY ON THE DYNAMIC BEHAVIOR OF AN ADSORBENT BED

6.1 INTRODUCTION

In this chapter, the effect of the adsorbent bed dimension in R and Z directions, convective heat transfer coefficient between the cooling fluid and adsorbent bed and the thermal conductivity of the solid adsorbent material on the transient distributions of the solid and gas phase temperature difference, differences in the amount adsorbed predicted by the equilibrium and linear driving force (LDF) models, solid phase temperature, gas pressure and amount adsorbed inside the adsorbent bed of an solid sorption cooling system have been investigated numerically for a nearly isobaric adsorption process. A transient two-dimensional local thermal non-equilibrium model that takes into account both internal and external mass transfer resistances has been used. Silica gel/water is selected as the working pair. It has been found that generally, the effects of the parameters investigated on the transient distributions of the temperature difference between the phases, difference in amount adsorbed between the equilibrium and LDF models, and gas phase pressure gradients are negligible small. The thickness of the adsorbent bed for the given adsorbent bed length and thermal conductivity of the solid adsorbent material have a large influence on the transient distributions of the solid phase temperature and amount adsorbed. On the other hand, the transient temperature and amount adsorbed distributions are only slightly by the variation of the adsorbent bed length and convective heat transfer for the conditions studied.

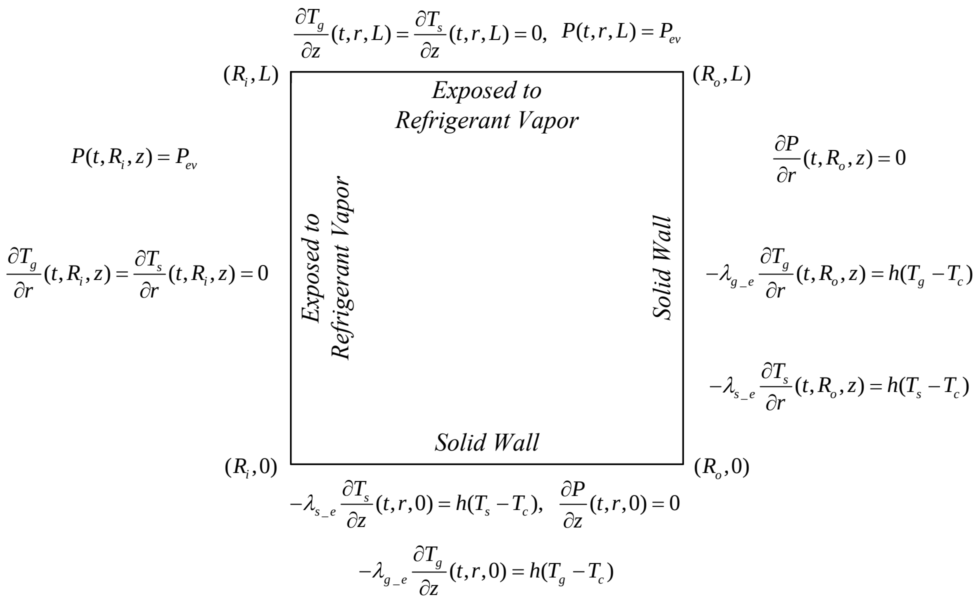

Figure 6.1: Modeling domain with the boundary conditions.

6.2 DESCRIPTION OF THE ADSORBENT BED

A schematic view of the adsorbent bed using the silica-gel/water working pair is shown in Figure 5.1. All the dimensions of the adsorbent bed and the thermo-physical properties of the silica-gel/water pair are presented in Table 6.1. The primary components of the adsorbent bed are an inner vacuum tube, a mass transfer tube, a larger tubular shell and a single top cover for the vacuum tube and the tubular shell. Silica-gel granules are packed in the annulus between the vacuum and mass transfer tubes and a vapor gap is left at the top of the vacuum tube to allow better vapor transfer in the axial direction. The vacuum tube is inserted into the larger tubular shell and a heat transfer fluid circulated between the shell and vacuum tube to cool down the adsorbent bed during the adsorption process. Refrigerant vapor enters the vacuum tube through the top cover and flows both in the radial and axial directions. The 2D domain modeled is labeled as Modeling domain with the boundary conditions in Figure 6.1 representing the plots in the results as well. The right and bottom edges are in thermal contact with the heat transfer fluid and are referred to as the heat transfer boundaries. The top and left edges are assumed to be well-insulated and are modeled as being adiabatic.

6.3 MATHEMATICAL MODELING

6.3.1 Mass Conservation Equation

The macro scale mass conservation equation for the adsorbate gas from the Equation 4.23 is written as:

$$\epsilon_t \frac{\partial \rho_g}{\partial t} + \frac{1}{r}\frac{\partial \left(r \rho_g v_r \right)}{\partial r} + \frac{\partial \left(\rho_g v_z \right)}{\partial z} + (1 - \epsilon_t) \rho_s \frac{\partial X}{\partial t} = 0 \qquad (6.1)$$

In the equation above, the volume fraction of the gas phase, ϵ_g, is assumed to be equal to the total porosity, ϵ_t, and it is evaluated using the Equation 5.2. Finite internal mass transfer rates are modeled using the LDF model given in Equation 5.3. The adsorption rate is assumed equal to this internal mass transfer and therefore adsorption equilibrium is not assumed. Dubinin-Astakhov (D-A) equation given in Equation 5.6 is used to evaluate the equilibrium adsorption capacity of the solid adsorbent material in the LDF model.

6.3.2 Momentum Equation

External mass transfer resistances are included in the present model, which can lead to significant bulk pressure gradients. Darcy's equation including only viscous effects is used to describe the velocity field of the vapor adsorbate in the computational domain. The inertial effects accounted for by Ergun's equation are ignored because of the very low speed of the vapor adsorbate flowing through the voids between the adsorbent particles.

$$v = -\frac{K_d}{\mu_g} \nabla P \qquad (6.2)$$

where K_d is the real permeability which can be calculated by Equation 5.10

6.3.3 Energy Conservation Equations

6.3.3.1 Energy Conservation Equation for the Gas Phase

The macro scale energy conservation equation for the gas phase from the Equation 4.60 is written as:

$$c_{pg}\rho_g\left[\epsilon_t\frac{\partial T_g}{\partial t}+v_r\frac{\partial T_g}{\partial r}+v_z\frac{\partial T_g}{\partial z}\right]=-(1-\epsilon_t)\rho_s\frac{\partial X}{\partial t}c_{pg}\left(T_s-T_g\right)+\frac{1}{r}\frac{\partial}{\partial r}\left(r\lambda_{ge}\frac{\partial T_g}{\partial r}\right)$$

$$+\frac{\partial}{\partial z}\left(\lambda_{ge}\frac{\partial T_g}{\partial z}\right)+a_v h_{gs}\left(T_s-T_g\right) \qquad (6.3)$$

6.3.3.2 Energy Conservation Equation for the Solid Phase

The macroscopic energy conservation equation for the solid phase from the Equation 4.66 is given by

$$\rho_s(1-\epsilon_t)\left[c_{ps}+Xc_{pg}\right]\frac{\partial T_s}{\partial t}=\frac{1}{r}\frac{\partial}{\partial r}\left(r\lambda_{se}\frac{\partial T_s}{\partial r}\right)+\frac{\partial}{\partial z}\left(\lambda_{se}\frac{\partial T_s}{\partial z}\right)-a_v h_{gs}\left(T_s-T_g\right)$$

$$+(1-\epsilon_t)\rho_s\frac{\partial X}{\partial t}Q_{ad} \qquad (6.4)$$

The effective thermal conductivity for the solid and gas phases, the vapor -solid specific surface area and the interfacial heat transfer coefficient for spherical particles and the equation of state for the adsorbate vapor phase are defined in Equations 5.15, 5.16, 5.17 and 5.20, respectively.

Using the assumptions that refrigerant is an ideal gas and its kinematic viscosity is constant and then, substituting the Equation 6.2 into the Equations 6.1 and 6.3 for simplicity of the calculation, Equations 6.1 and 6.3 take the following form, respectively.

$$\frac{\epsilon_t}{R_gT_g}\frac{\partial P}{\partial t}-\frac{P}{R_gT_g^2}\frac{\partial T_g}{\partial t}-\frac{K_d}{\nu_g}\frac{1}{r}\frac{\partial}{\partial r}\left(r\frac{\partial P}{\partial r}\right)-\frac{K_d}{\nu_g}\frac{\partial^2 P}{\partial z^2}+(1-\epsilon_t)\rho_s\frac{\partial X}{\partial t}=0 \qquad (6.5)$$

$$c_{pg}\rho_g\left[\epsilon_t\frac{\partial T_g}{\partial t}-\frac{K_d}{\mu_g}\frac{\partial P}{\partial r}\frac{\partial T_g}{\partial r}-\frac{K_d}{\mu_g}\frac{\partial P}{\partial z}\frac{\partial T_g}{\partial z}\right]=-\left(1-\epsilon_t\right)\rho_s\frac{\partial X}{\partial t}c_{pg}\left(T_s-T_g\right)+\frac{1}{r}\frac{\partial}{\partial r}\left(r\lambda_{ge}\frac{\partial T_g}{\partial r}\right)$$

$$+\frac{\partial}{\partial z}\left(\lambda_{ge}\frac{\partial T_g}{\partial z}\right)+a_v h_{gs}\left(T_s-T_g\right) \tag{6.6}$$

6.3.4 Initial and Boundary Conditions

Temperature, pressure and amount-adsorbed gradients are investigated where $T = T\left(t, R, Z\right)$, $P = P\left(t, R, Z\right)$, and $X = X\left(t, R, Z\right)$.

The temperatures (solid and gas), pressure and amount-adsorbed distributions in both directions inside the adsorbent bed are initially considered to be uniform.

$$T_g\left(0, R, Z\right) = T_s\left(0, R, Z\right) = T_i, \quad P\left(0, R, Z\right) = P_i \quad \text{and} \quad X\left(0, R, Z\right) = X_i \tag{6.7}$$

Referring to the analysis domain in Figure 6.1, at the $R = R_i$ (left) and $Z = L$ (top) boundaries it is assumed that the vapor pressure is equal to the evaporator pressure and the temperature gradients for both the solid and gas phases are zero (i.e., adiabatic boundaries).

$$P\left(t, R_i, Z\right) = P_{ev} \tag{6.8}$$

$$P\left(t, R, L\right) = P_{ev} \tag{6.9}$$

$$\frac{\partial T_g}{\partial r}\left(t, R_i, Z\right) = \frac{\partial T_s}{\partial r}\left(t, R_i, Z\right) = 0 \tag{6.10}$$

$$\frac{\partial T_g}{\partial z}\left(t, R, L\right) = \frac{\partial T_s}{\partial z}\left(t, R, L\right) = 0 \tag{6.11}$$

At the $R = R_o$ (right) and $Z = 0$ (bottom) boundaries the pressure gradient is zero since the walls are impermeable and a convective heat transfer boundary conditions exists for the solid and gas phases.

$$\frac{\partial P}{\partial r}(t, R_o, Z) = 0 \tag{6.12}$$

$$\frac{\partial P}{\partial z}(t, R, 0) = 0 \tag{6.13}$$

$$-\lambda_{ge}\frac{\partial T_g}{\partial r}(t, R_o, Z) = h\left(T_g - T_c\right) \tag{6.14}$$

$$-\lambda_{se}\frac{\partial T_s}{\partial r}(t, R_o, Z) = h\left(T_s - T_c\right) \tag{6.15}$$

$$-\lambda_{ge}\frac{\partial T_g}{\partial z}(t, R, 0) = h\left(T_g - T_c\right) \tag{6.16}$$

$$-\lambda_{se}\frac{\partial T_s}{\partial z}(t, R, 0) = h\left(T_s - T_c\right) \tag{6.17}$$

6.4 METHOD OF SOLUTION

The nonlinear coupled governing partial differential equations under consideration were solved numerically using the finite difference technique. The central difference, first order upwind scheme given in Equation 5.24, and forward difference approximations were used to discretize the second order spatial derivatives, convective, and unsteady terms, respectively. Additionally, the imaginary points were eliminated by using the forward or backward difference approximation (depending on the boundary where derivative type boundary conditions are defined).

The two-dimensional nature of the problem limits the number of numerical methods that can be utilized efficiently. Explicit methods begin to have strong stability restrictions and previously used implicit method in Chapter 5 no longer forms a tri-diagonal system of algebraic equations making the solution to the matrix computationally intense [74]. The problem with the two-dimensional implicit scheme can be overcome by splitting the system of algebraic equations into two half-steps to advance one time step. At each half-step, only terms associated with a particular coordinate direction are treated implicitly. Consequently, only three implicit terms appear and these can be grouped adjacent to the main diagonal. As a result, very efficient Thomas algorithm can be used to obtain the solution.

In this study, the alternating direction implicit (ADI) method that is the best known example of a splitting technique was used as an solution method for the two dimensional governing conservation equations [75]. ADI scheme for the first half-time step for the Equation 6.5, 6.4 and 6.6 can be written as follows, respectively.

Mass conservation equation:

$$\frac{\epsilon_t}{R_g T^{n+1}_{g_{i,j}}}\left[\frac{P^{n+1}_{i,j}-P^{n}_{i,j}}{\Delta t/2}\right]-\frac{P^{n+1}_{i,j}}{R_g\left(T^{n+1}_{g_{i,j}}\right)^2}\left[\frac{T^{n+1}_{g_{i,j}}-T^{n}_{g_{i,j}}}{\Delta t/2}\right]-\frac{K_d}{\nu_g}\left[\frac{P^{n}_{i,j+1}-2P^{n}_{i,j}+P^{n}_{i,j-1}}{\Delta z^2}\right]$$

$$-\frac{K_d}{\nu_g}\left[\frac{P^{n+1}_{i+1,j}-P^{n+1}_{i-1,j}}{2\Delta r\, r_i}+\frac{P^{n+1}_{i+1,j}-2P^{n+1}_{i,j}+P^{n+1}_{i-1,j}}{\Delta r^2}\right]$$

$$+(1-\epsilon_t)\rho_s k^{n+1}_{m_{i,j}}\left(X^{n+1}_{\infty_{i,j}}-X^{n+1}_{i,j}\right)=f_1 \tag{6.18}$$

Energy conservation equation for the solid phase:

$$c^{n+1}_{ms_{i,j}}\frac{T^{n+1}_{s_{i,j}}-T^{n}_{s_{i,j}}}{\Delta t/2}-\lambda_{se}\left[\frac{T^{n+1}_{s_{i+1,j}}-T^{n+1}_{s_{i-1,j}}}{2\Delta r\, r_i}+\frac{T^{n+1}_{s_{i+1,j}}-2T^{n+1}_{s_{i,j}}+T^{n+1}_{s_{i-1,j}}}{\Delta r^2}-\frac{T^{n}_{s_{i,j+1}}-2T^{n}_{s_{i,j}}+T^{n}_{s_{i,j-1}}}{\Delta z^2}\right]$$

$$+a_v h^{n+1}_{gs_{i,j}}\left(T^{n+1}_{s_{i,j}}-T^{n+1}_{g_{i,j}}\right)-(1-\epsilon_t)\rho_s Q_{ad} k^{n+1}_{m_{i,j}}\left(X^{n+1}_{\infty_{i,j}}-X^{n+1}_{i,j}\right)=f_3 \tag{6.19}$$

Energy conservation equation for the gas phase:

$$\begin{aligned}
&c_{pg}\rho^{n+1}_{g_{i,j}} \left[\epsilon_t \frac{T^{n+1}_{g_{i,j}} - T^{n}_{g_{i,j}}}{\Delta t/2} - \frac{K_d}{\mu_g}\frac{P^{n+1}_{i+1,j} - P^{n+1}_{i-1,j}}{2\Delta r}\left((1-J)\frac{T^{n+1}_{g_{i,j}} - T^{n+1}_{g_{i-1,j}}}{\Delta r} + J\frac{T^{n+1}_{g_{i+1,j}} - T^{n+1}_{g_{i,j}}}{\Delta r}\right)\right] \\
&- c_{pg}\rho^{n+1}_{g_{i,j}}\left[\frac{K_d}{\mu_g}\frac{P^{n}_{i,j+1} - P^{n}_{i,j-1}}{2\Delta z}\left((1-I)\frac{T^{n}_{g_{i,j}} - T^{n}_{g_{i,j-1}}}{\Delta z} + I\frac{T^{n}_{g_{i,j+1}} - T^{n}_{g_{i,j}}}{\Delta z}\right)\right] \\
&+ (1-\epsilon_t)\rho_s k^{n+1}_{m_{i,j}}\left(X^{n+1}_{\infty_{i,j}} - X^{n+1}_{i,j}\right) c_{pg}\left(T^{n+1}_{s_{i,j}} - T^{n+1}_{g_{i,j}}\right) - \lambda_{ge}\left[\frac{T^{n}_{g_{i,j+1}} - 2T^{n}_{g_{i,j}} + T^{n}_{g_{i,j-1}}}{\Delta z^2}\right] \\
&- \lambda_{ge}\left[\frac{T^{n+1}_{g_{i+1,j}} - T^{n+1}_{g_{i-1,j}}}{2\Delta r\, r_i} + \frac{T^{n+1}_{g_{i+1,j}} - 2T^{n+1}_{g_{i,j}} + T^{n+1}_{g_{i-1,j}}}{\Delta r^2}\right] - a_v h^{n+1}_{gs_{i,j}}\left(T^{n+1}_{s_{i,j}} - T^{n+1}_{g_{i,j}}\right) = f_2
\end{aligned} \tag{6.20}$$

Additionally, ρ_g, X_∞, k_m, X, c_{ms} and h_{gs} calculated during the first half-time step are formulated as follows;

Density of the gas phase:

$$\rho^{n+1}_{g_{i,j}} - \frac{P^{n+1}_{i,j}}{R_g T^{n+1}_{g_{i,j}}} = f_4 \tag{6.21}$$

Equlibrium adsorption capacity:

$$X^{n+1}_{\infty_{i,j}} - 0.346\exp\left[-5.6\left(\frac{T^{n+1}_{s_{i,j}}}{\left(\frac{1730.63}{8.0713-\log_{10}\left(7.0063P^{n+1}_{i,j}\right)} + 39.724\right)} - 1\right)^{1.6}\right] = f_5 \tag{6.22}$$

Internal mass transfer coefficent:

$$k^{n+1}_{m_{i,j}} - \frac{15}{r_p^2}D_o\exp\left(-E_a/RT^{n+1}_{s_{i,j}}\right) = f_6 \tag{6.23}$$

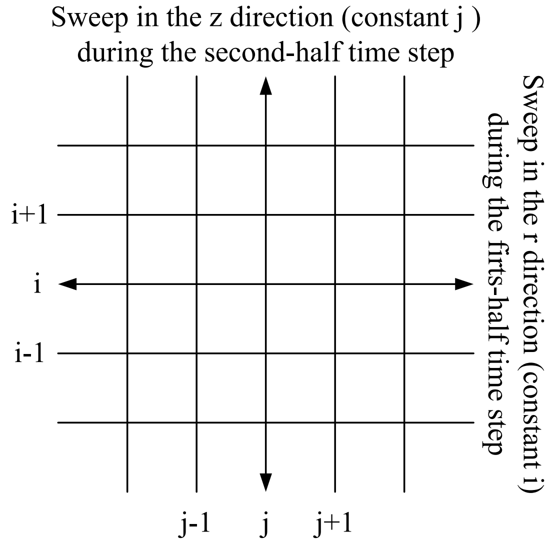

Figure 6.2: ADI implementation.

Adsorption capacity:

$$\frac{X_{i,j}^{n+1} - X_{i,j}^{n}}{\Delta t/2} - k_{m_{i,j}}^{n+1} \left(X_{\infty_{i,j}}^{n+1} - X_{i,j}^{n+1} \right) = f_7 \tag{6.24}$$

Specific heat of the solid-gas phase mixture:

$$c_{ms_{i,j}}^{n+1} - \rho_s \left(1 - \epsilon_t\right) \left[c_{ps} + X_{i,j}^{n+1} c_{pg} \right] = f_8 \tag{6.25}$$

Interface heat transfer coefficient:

$$h_{gs_{i,j}}^{n+1} - \frac{K_g}{d_p} \left(2 + 1.8 Pr^{0.33} \left(Re_{d_{i,j}}^{n+1} \right)^{0.5} \right) = f_9 \tag{6.26}$$

During the first half-time step, T_g, T_s, P and X is known at time level n but are unknown at the $(n+1)$ time level. However, unknown nodal values are associated with the r direction only (i.e constant value of the i in Figure 6.2). The system of nine algebraic equations given above are applied at each grid point in the same row i ($j = 1 \ldots, N_r$ for one value of i only) by taking into account of the boundary conditions. The resulting set of nonlinear algebraic equations is solved iteratively by the combination of the Newton-Raphson iteration scheme and a block tridiagonal matrix solver algorithm (Thomas algorithm). Implementation of these methods are described thoroughly in Chapter 5. The solution of the set of equations gives the intermediate solution for the nine unknowns at the $(n + 1)$ time level in the same row i. The solution methodology described above are repeated for $j = 1\dots, N_r$, for each row, $i = 1\dots, N_z$.

During the second half time-step, the Equation 6.5, 6.6 and 6.4 can be formed as follows, respectively.

Mass conservation equation:

$$\frac{\epsilon_t}{R_g T^{n+2}_{g_{i,j}}}\left[\frac{P^{n+2}_{i,j}-P^{n+1}_{i,j}}{\Delta t/2}\right]-\frac{P^{n+2}_{i,j}}{R_g\left(T^{n+2}_{g_{i,j}}\right)^2}\left[\frac{T^{n+2}_{g_{i,j}}-T^{n+1}_{g_{i,j}}}{\Delta t/2}\right]-\frac{K_d}{\nu_g}\left[\frac{P^{n+2}_{i,j+1}-2P^{n+2}_{i,j}+P^{n+2}_{i,j-1}}{\Delta z^2}\right]$$

$$-\frac{K_d}{\nu_g}\left[\frac{P^{n+1}_{i+1,j}-P^{n+1}_{i-1,j}}{2\Delta r\, r_i}+\frac{P^{n+1}_{i+1,j}-2P^{n+1}_{i,j}+P^{n+1}_{i-1,j}}{\Delta r^2}\right]$$

$$+(1-\epsilon_t)\rho_s k^{n+2}_{m_{i,j}}\left(X^{n+2}_{\infty_{i,j}}-X^{n+2}_{i,j}\right)=f_1 \tag{6.27}$$

Energy conservation equation for the gas phase:

$$c_{pg}\rho^{n+2}_{g_{i,j}}\left[\epsilon_t\frac{T^{n+2}_{g_{i,j}}-T^{n+1}_{g_{i,j}}}{\Delta t/2}-\frac{K_d}{\mu_g}\frac{P^{n+1}_{i+1,j}-P^{n+1}_{i-1,j}}{2\Delta r}\left((1-J)\frac{T^{n+1}_{g_{i,j}}-T^{n+1}_{g_{i-1,j}}}{\Delta r}+J\frac{T^{n+1}_{g_{i+1,j}}-T^{n+1}_{g_{i,j}}}{\Delta r}\right)\right]$$

$$-c_{pg}\rho^{n+2}_{g_{i,j}}\left[\frac{K_d}{\mu_g}\frac{P^{n+2}_{i,j+1}-P^{n+2}_{i,j-1}}{2\Delta z}\left((1-I)\frac{T^{n+2}_{g_{i,j}}-T^{n+2}_{g_{i,j-1}}}{\Delta z}+I\frac{T^{n+2}_{g_{i,j+1}}-T^{n+2}_{g_{i,j}}}{\Delta z}\right)\right]$$

$$+(1-\epsilon_t)\rho_s k^{n+2}_{m_{i,j}}\left(X^{n+2}_{\infty_{i,j}}-X^{n+2}_{i,j}\right)c_{pg}\left(T^{n+2}_{s_{i,j}}-T^{n+2}_{g_{i,j}}\right)-\lambda_{ge}\left[\frac{T^{n+2}_{g_{i,j+1}}-2T^{n+2}_{g_{i,j}}+T^{n+2}_{g_{i,j-1}}}{\Delta z^2}\right]$$

$$-\lambda_{ge}\left[\frac{T^{n+1}_{g_{i+1,j}}-T^{n+1}_{g_{i-1,j}}}{2\Delta r\, r_i}+\frac{T^{n+1}_{g_{i+1,j}}-2T^{n+1}_{g_{i,j}}+T^{n+1}_{g_{i-1,j}}}{\Delta r^2}\right]-a_v h^{n+2}_{gs_{i,j}}\left(T^{n+2}_{s_{i,j}}-T^{n+2}_{g_{i,j}}\right)=f_2 \tag{6.28}$$

Energy conservation equation for the solid phase:

$$c_{ms_{i,j}}^{n+2}\frac{T_{s_{i,j}}^{n+2}-T_{s_{i,j}}^{n+1}}{\Delta t/2}-\lambda_{se}\left[\frac{T_{s_{i+1,j}}^{n+1}-T_{s_{i-1,j}}^{n+1}}{2\Delta r\, r_i}+\frac{T_{s_{i+1,j}}^{n+1}-2T_{s_{i,j}}^{n+1}+T_{s_{i-1,j}}^{n+1}}{\Delta r^2}-\frac{T_{s_{i,j+1}}^{n+2}-2T_{s_{i,j}}^{n+2}+T_{s_{i,j-1}}^{n+2}}{\Delta z^2}\right]$$

$$+\,a_v h_{gs_{i,j}}^{n+2}\left(T_{s_{i,j}}^{n+2}-T_{g_{i,j}}^{n+2}\right)-(1-\epsilon_t)\,\rho_s Q_{ad} k_{m_{i,j}}^{n+2}\left(X_{\infty_{i,j}}^{n+2}-X_{i,j}^{n+2}\right)=f_3 \tag{6.29}$$

Finite difference formulations of the ρ_g, X_∞, k_m, X, c_{ms} and h_{gs} evaluated during the second half-time step are given as below:

Density of the gas phase:

$$\rho_{g_{i,j}}^{n+2}-\frac{P_{i,j}^{n+2}}{R_g T_{g_{i,j}}^{n+2}}=f_4 \tag{6.30}$$

Equlibrium adsorption capacity:

$$X_{\infty_{i,j}}^{n+2}-0.346\exp\left[-5.6\left(\frac{T_{s_{i,j}}^{n+2}}{\left(\frac{1730.63}{8.0713-\log_{10}\left(7.0063P_{i,j}^{n+2}\right)}+39.724\right)}-1\right)^{1.6}\right]=f_5 \tag{6.31}$$

Internal mass transfer coefficent:

$$k_{m_{i,j}}^{n+2}-\frac{15}{r_p^2}D_o\exp\left(-E_a/RT_{s_{i,j}}^{n+2}\right)=f_6 \tag{6.32}$$

Adsorption capacity:

$$\frac{X_{i,j}^{n+2}-X_{i,j}^{n+1}}{\Delta t/2}-k_{m_{i,j}}^{n+2}\left(X_{\infty_{i,j}}^{n+2}-X_{i,j}^{n+2}\right)=f_7 \tag{6.33}$$

Specific heat of the solid-gas phase mixture:

$$c_{ms_{i,j}}^{n+2}-\rho_s\,(1-\epsilon_t)\left[c_{ps}+X_{i,j}^{n+2}c_{pg}\right]=f_8 \tag{6.34}$$

Table 6.1: Effects of the number of grid points and time steps on the solid phase temperature (K) at nearly thermal equilibrium case and various locations in the computational domain.

	$\Delta t = 0.5\,\mathrm{s}$		$\Delta t = 1\,\mathrm{s}$	
r,z (m)	$5 * 25$	$10 * 50$	$5 * 25$	$10 * 50$
0.012, 0.088	314,329935	314,379638	314,334036	314,383828
0.018, 0.088	313,802534	313,845411	313,804846	313,847829
0.012, 0.012	313,998231	314,032621	314,001147	314,035600
0.018, 0.012	313,623038	313,652964	313,624663	313,654667

Interface heat transfer coefficient:

$$h_{gs_{i,j}}^{n+2} - \frac{K_g}{d_p}\left(2 + 1.8Pr^{0.33}\left(Re_{d_{i,j}}^{n+2}\right)^{0.5}\right) = f_9 \qquad (6.35)$$

During the second half-time step, T_g, T_s, P and X are unknown at the $(n+2)$ time level but are known at the intermediate time level $(n+1)$. However, in this case, unknown nodal values are associated with the z direction only (i.e fixed value of the j in Figure 6.2). Therefore, the system of nine algebraic equations associated with all the nodes along one grid line in the z direction is solved for ρ_g, T_g, T_s, P, X_∞, k_m, X, c_{ms} and h_{gs} using the Newton-Raphson iteration scheme and the Thomas algorithm and then, the process is repeated for $i = 1 \ldots, N_z$, for each column, $j = 1 \ldots, N_r$ to advance one time step.

The influence of the number of grid points and time steps on the solid phase temperature at nearly thermal equilibrium case and various locations in the computational domain is shown in Table 6.1. It can be seen from Table 6.1 that the difference between the results obtained for two different grid sizes (5*25 and 10*50) and time steps (0.5 and 1 s) is quite small. Therefore, the number of grid points is varied in the range between 20*80 and 25*100 and the time step is selected as 0.25 s to ensure the reliability of the numerical computations. The grid distribution in the computational domain is uniform. A computer simulation program based on the numerical procedure above was written in Matlab to perform the parametric investigation. The main simulation parameters used in the computer simulation program are given in Table 6.2.

Table 6.2: Base case simulation parameters for 2-D study.

Parameter	Value	Unit	Reference
c_{pg}	1800	$\mathrm{Jkg^{-1}K^{-1}}$	
c_{ps}	924	$\mathrm{Jkg^{-1}K^{-1}}$	[62]
d_p	$5\mathrm{e}^{-4}$	m	[62]
D_o	$2.54\mathrm{e}^{-4}$	$\mathrm{m^2s^{-1}}$	[62]
E_a	$4.2\mathrm{e}^{4}$	$\mathrm{Jmol^{-1}}$	[62]
h	100	$\mathrm{Wm^{-2}K^{-1}}$	
k_g	0.024	$\mathrm{Wm^{-1}K^{-1}}$	
k_s	0.198	$\mathrm{Wm^{-1}K^{-1}}$	[62]
L	0.1	m	
P_{co}	4.246	kPa	
P_{ev}	1.228	kPa	
R_i	0.01	m	
R_o	0.02	m	
T_c	40	°C	
T_h	100	°C	
ϵ_b	0.37		[62]
ϵ_p	0.42		[62]
Q_{ad}	2693	$\mathrm{kJkg_w^{-1}}$	[62]
μ_g	$1.5\mathrm{e}^{-5}$	$\mathrm{kgm^{-1}s^{-1}}$	
ρ_s	2027	$\mathrm{kgm^{-3}}$	[62]

The initial temperatures for the gas and solid phases were calculated by means of the generation temperature of the adsorbent bed (T_h), condenser pressure (P_{co}), and evaporator pressure (P_{ev}). The adsorption capacity of the solid adsorbent was assumed to be constant as the pressure inside the adsorbent bed was decreased from the condenser to the evaporator pressure.

6.5 RESULTS AND DISCUSSION

The effect of the adsorbent bed dimensions in the axial and radial directions, the convective heat transfer coefficient and the thermal conductivity of the adsorbent material on the transient distributions of the temperature difference between the phases, the solid phase temperature, the pressure, the amount adsorbed and the difference in the amount adsorbed calculated from the equilibrium and LDF models have been investigated numerically, and the results are presented below. At the starting point of the adsorption process for all simulations, the amount adsorbed, the solid and gas phase temperatures and the pressure throughout the adsorbent bed are uniform and are equal to 0.2 $\mathrm{kg_w kg_{ad}^{-1}}$, 348.5 K and 1.2282 kPa, respectively, according to the operating conditions of the system given in Table 6.2. In addition to this, for each parametric study all the parameters given in Table 6.2 are kept constant except the parameter investigated i.e. adsorbent bed length.

6.5.1 Temperature difference between the phases for the LTNE model

The temperature difference between the solid and gas phase inside the adsorbent bed was not taken into account in most of the studies published previously (see Table 1.3). Typically, in these studies, a single energy equation was used by assuming LTE between the phases without showing the validity of this assumption. However, it is stated in the literature that this assumption may not be correct in some circumstances and it may lead to unrealistic simulation results [58]. Therefore, one of the main objectives of this study is to investigate the validity of this assumption for the parameters investigated. For this purpose, two different energy conservation equations were developed to determine the separate temperature fields of the gas and solid adsorbent phases.

A parametric study of the transient distributions of the temperature difference between the

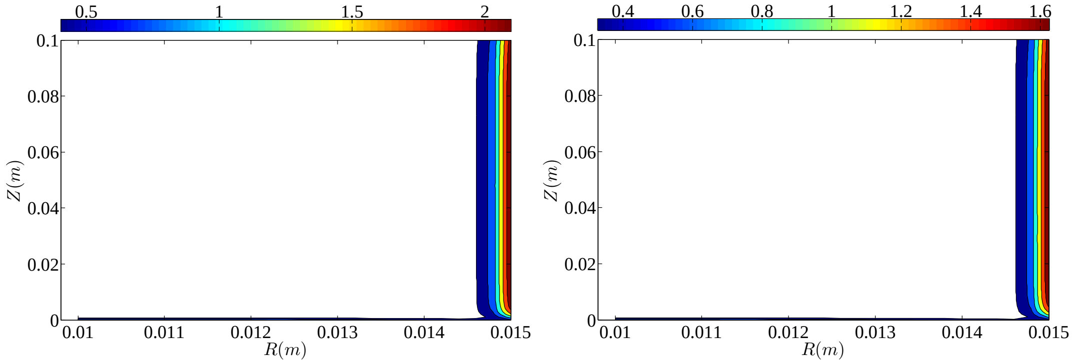

(a) R_o = 0.015 m and t = 50 s (b) R_o = 0.015 m and t = 100 s

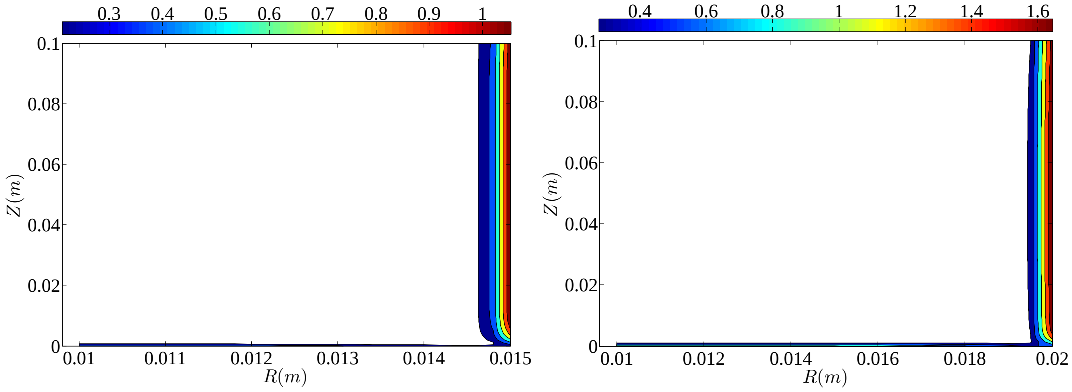

(c) R_o = 0.015 m and t = 200 s (d) R_o = 0.02 m and t = 50 s

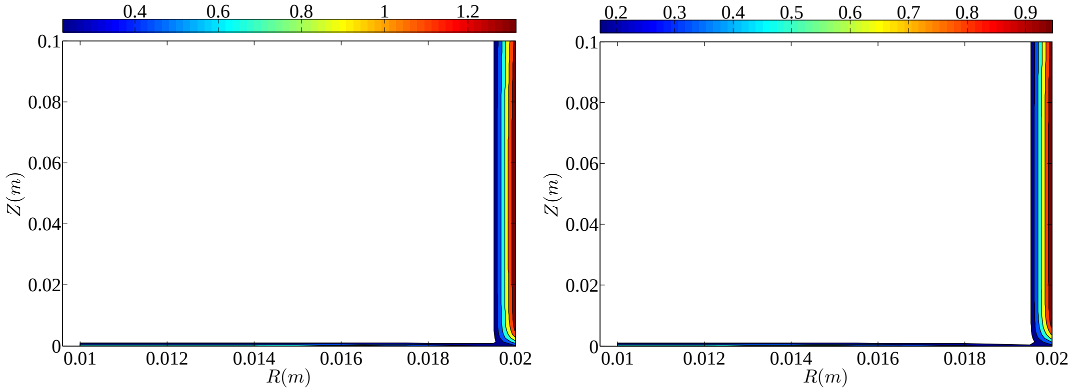

(e) R_o = 0.02 m and t = 100 s (f) R_o = 0.02 m and t = 200 s

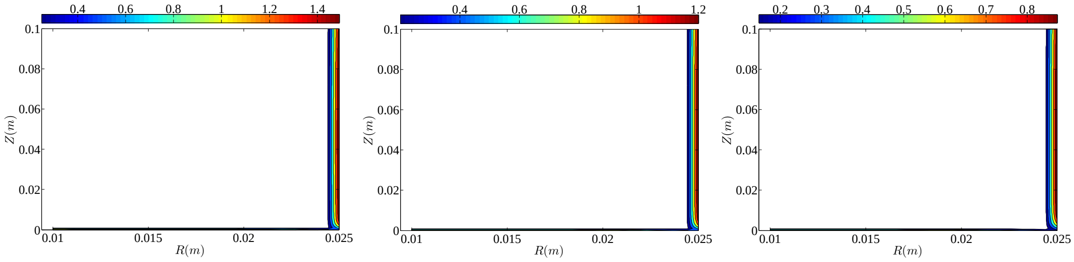

(g) R_o = 0.025 m and t = 50 s (h) R_o = 0.025 m and t = 100 s (i) R_o = 0.025 m and t = 200 s

Figure 6.3: The distribution of temperature difference, K, between the solid and gas phases.

solid and gas phases was performed for the following parameters and ranges: adsorbent bed length (0.05 to 0.2 m) and thickness (0.005 to 0.015 m); HTF convective heat transfer coefficient (25 to 400 $\mathrm{Wm^{-2}K^{-1}}$); and, thermal conductivity of the solid adsorbent material (0.2 to 1.5 $\mathrm{Wm^{-1}K^{-1}}$). For brevity only the conditions of $R_o - R_i = 0.005$ m to $R_o - R_i = 0.015$ m for the process time, 50, 100 and 200 s are presented in Figure 6.3 as this is representative of the other conditions. The heat transfer fluid flows past the right hand and bottom sides of Figure 6.3, which results in large rates of heat transfer and temperature gradients at these boundaries. Conversely, the left and top sides are modeled as adiabatic boundary conditions and therefore the temperature gradients go to zero at these boundaries. Generally, the temperature difference between the phases is only significant (ΔT >4 °C) close to the outer boundaries exposed to the HTF, especially, during the first few seconds. However, this temperature difference typically becomes less than 4 °C for process times greater than 50 s and decays toward zero as the time progress. The temperature difference between the phases at a given time increases with decreasing values of the adsorbent bed thickness and convective heat transfer coefficient and increasing values of the thermal conductivity of the solid adsorbent material, but is relatively insensitive to changes in adsorbent bed thickness. Therefore, it can be concluded that decreasing conductive and increasing convective thermal resistances resulting in low Bio number increases the temperature difference between the solid and gas phases. Consequently, the results obtained in this part of the study indicate that LTE assumption is reasonable for the range of conditions explored and thus, this assumption can be used for the simplicity.

6.5.2 Amount adsorbed difference between the equilibrium and LDF models

The difference in the amount adsorbed distributions for the equilibrium and LDF models for the various values of the adsorbent bed length and thickness, convective heat transfer coefficient and thermal conductivity of the solid adsorbent material are investigated and the range of values explored is the same for the section above. The results presented in Figure 6.4 are representative of the results for the other conditions and for brevity these and other results are discussed but not presented graphically. The difference in amount adsorbed between the equilibrium and LDF models for all the parameters studied is generally negligible small and thus, typically, the equilibrium adsorption model can be used instead of the LDF models for the modeling of the amount adsorbed without leading to any significant computational errors under the given conditions. The difference in amount adsorbed between the equilibrium

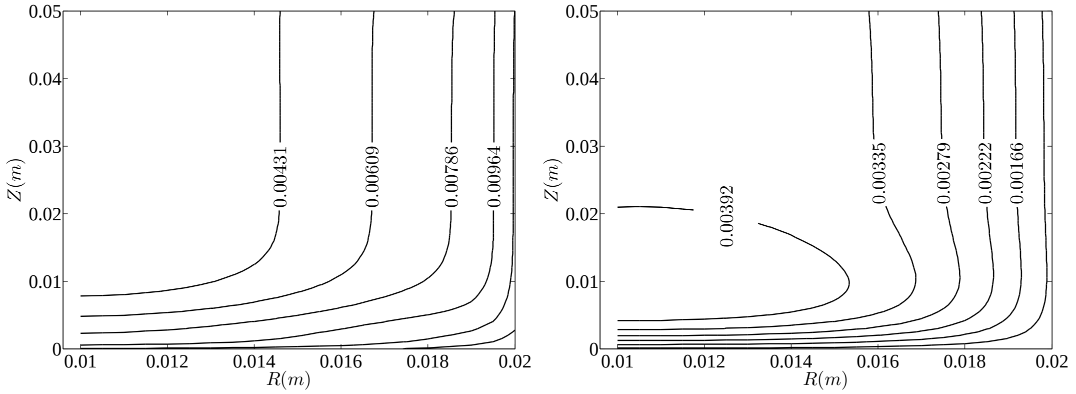

(a) Z = 0.05 m and t = 300 s (b) Z = 0.05 m and t = 900 s

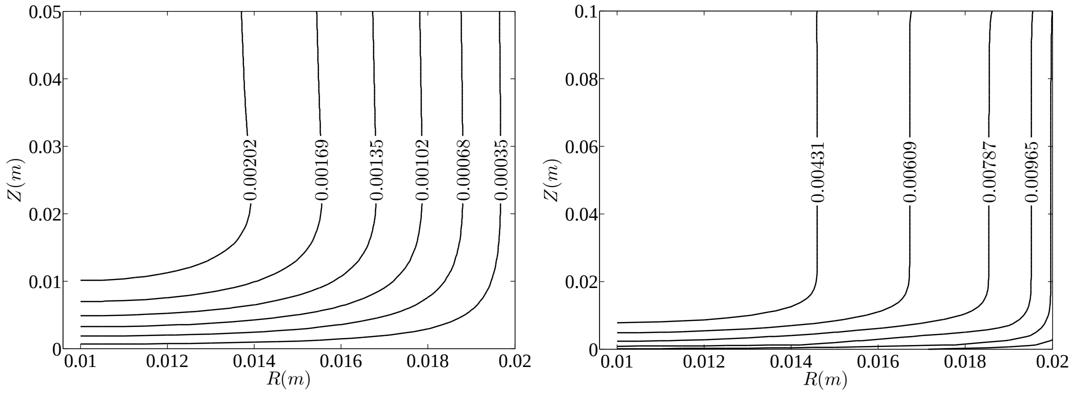

(c) Z = 0.05 m and t = 1800 s (d) Z = 0.1 m and t = 300 s

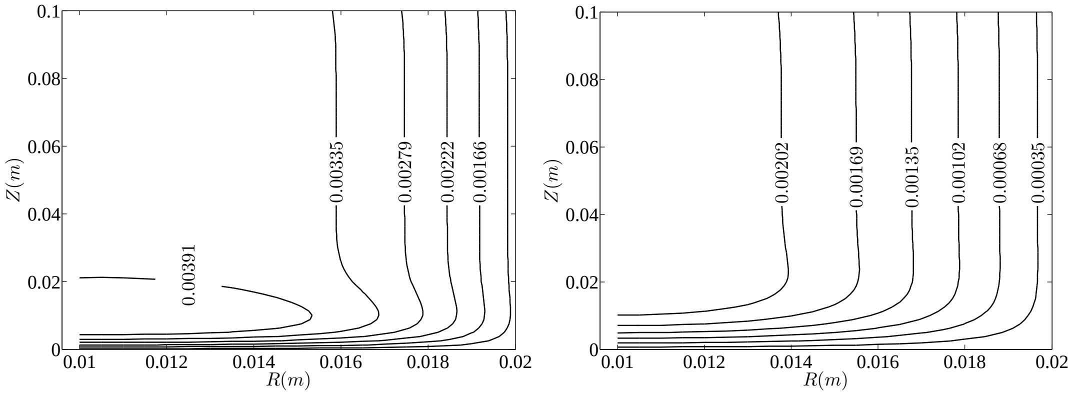

(e) Z = 0.1 m and t = 900 s (f) Z = 0.1 m and t = 1800 s

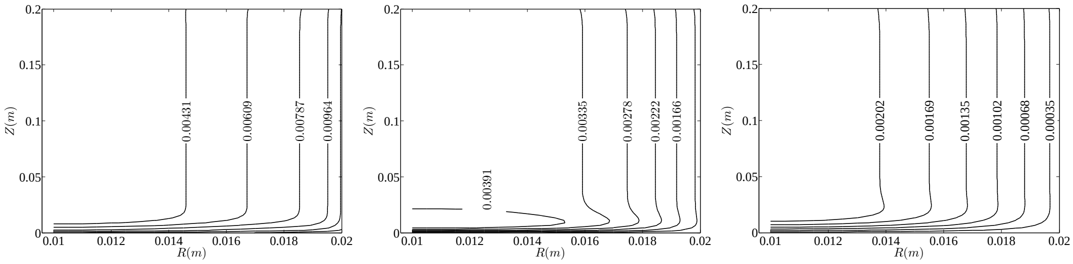

(g) Z = 0.2 m and t = 300 s (h) Z = 0.2 m and t = 900 s (i) Z = 0.2 m and t = 1800 s

Figure 6.4: The distribution of the amount adsorbed difference between the equilibrium and LDF models, $\mathrm{kg_w kg_{ad}^{-1}}$.

and LDF models decreases with increasing process time. This can be explained by the fact that the rate of amount adsorbed calculated from the equilibrium adsorption model is quite high at the early time steps of the process due to the high heat transfer rate and negligible pressure gradients and it decreases as time goes. On the other hand, the rate of amount adsorbed computed from the LDF model is relatively slow at all times because of the internal mass transfer resistances. Therefore, initially, the amount adsorbed difference between the equilibrium and LDF models is relatively large and this difference decreases as time increases.

6.5.3 Effect of the adsorbent bed length

Isotherms of the solid phase, isobars and contours of the amount adsorbed for adsorbent bed lengths of 0.05, 0.1 and 0.2 m and at times of 300, 900 and 1800 s are shown in Figure 6.5, 6.6 and 6.7, respectively. It is clear that the temperature, pressure and amount adsorbed distributions inside the adsorbent bed is only slightly affected by variations in the adsorbent bed length for the given adsorbent bed thickness, especially for adsorbent bed lengths greater than 0.1 m. The temperature and amount adsorbed gradients in the axial direction are only significant near the bottom boundary at the early stages of the process. However, in the radial direction these gradients are not only considerable near the right heat transfer boundary but also throughout the rest of the bed. Temperature and amount adsorbed gradients in both directions gradually become insignificant as the time progress. It can be concluded that the heat and mass transfer inside the adsorbent bed can be approximated as one dimensional in the r direction for large values of adsorbent bed length, but the two-dimensional effects cannot be neglected for aspect ratios nearly equal to one. The pressure gradients throughout the adsorbent bed are generally negligible. The resistance to adsorbate vapor flow in the axial direction is higher than that in the radial direction as a result of the high aspect ratio. Initially, the pressure at the heat transfer boundaries decreases suddenly due to increasing value of the amount adsorbed since there is a sharp temperature drop at these boundaries. Thus, the adsorbate vapor in the interior of the adsorbent bed starts to move from the high pressure to low pressure regions. As a result of this, the amount adsorbed at the outer boundaries increases suddenly. After half an hour, the adsorbent bed nearly reaches thermal, mechanical and chemical equilibrium conditions.

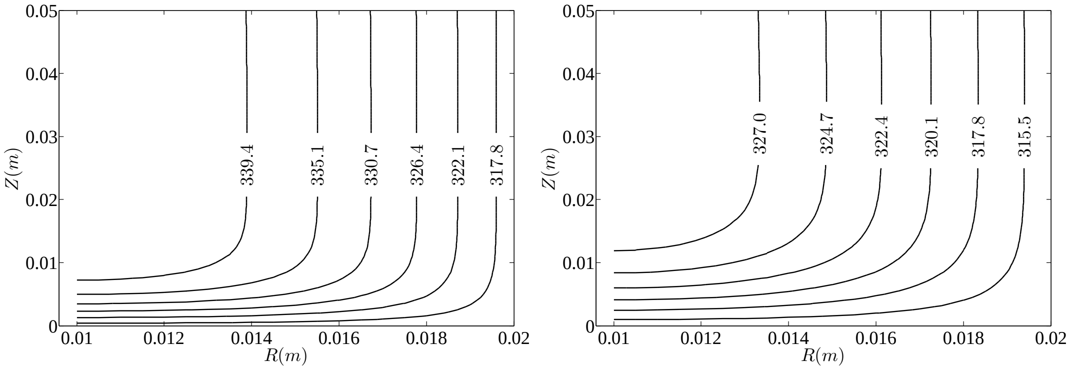

(a) Z = 0.05 m and t = 300 s (b) Z = 0.05 m and t = 900 s

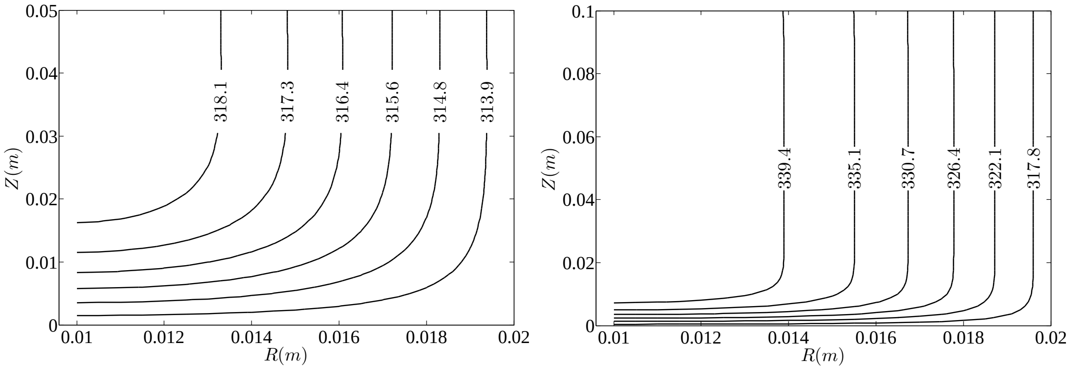

(c) Z = 0.05 m and t = 1800 s (d) Z = 0.1 m and t = 300 s

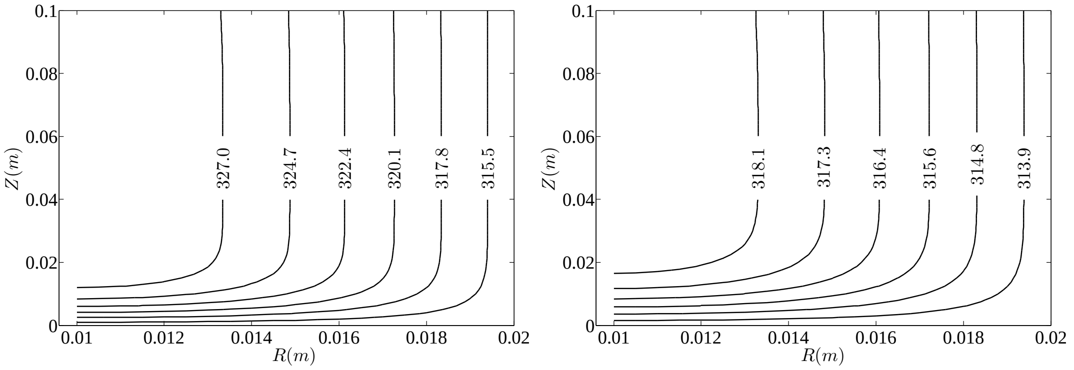

(e) Z = 0.1 m and t = 900 s (f) Z = 0.1 m and t = 1800 s

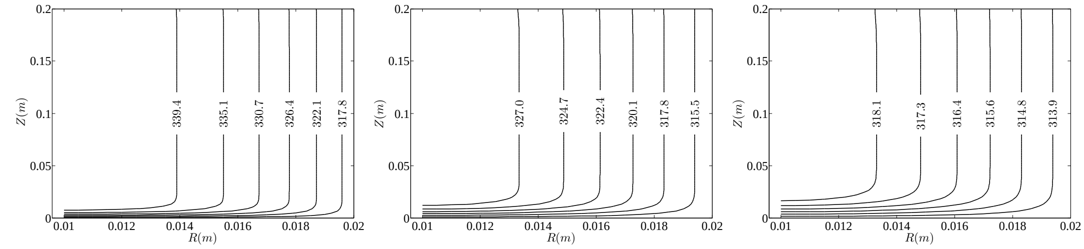

(g) Z = 0.2 m and t = 300 s (h) Z = 0.2 m and t = 900 s (i) Z = 0.2 m and t = 1800 s

Figure 6.5: Transient solid phase temperature, K, distributions for various adsorbent bed lengths.

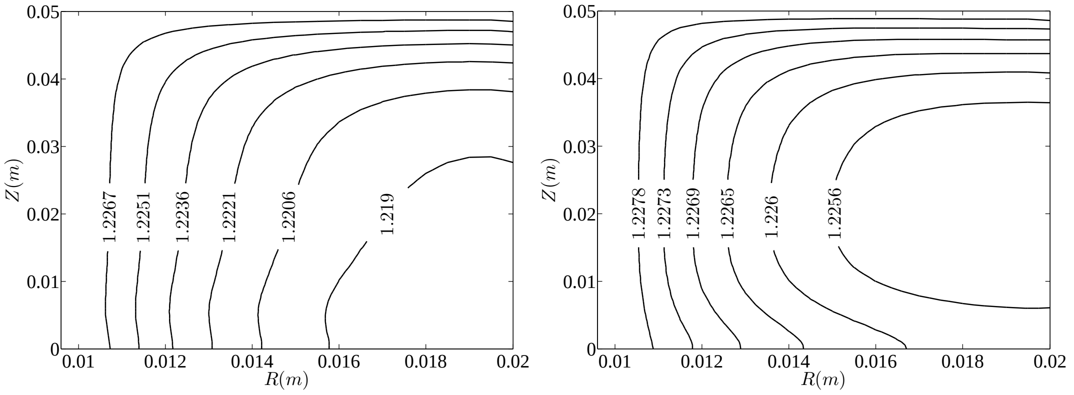

(a) Z = 0.05 m and t = 300 s (b) Z = 0.05 m and t = 900 s

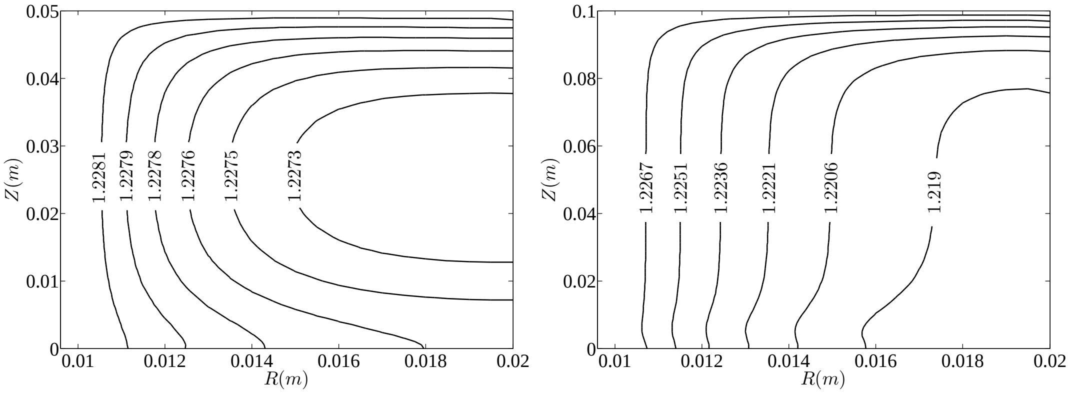

(c) Z = 0.05 m and t = 1800 s (d) Z = 0.1 m and t = 300 s

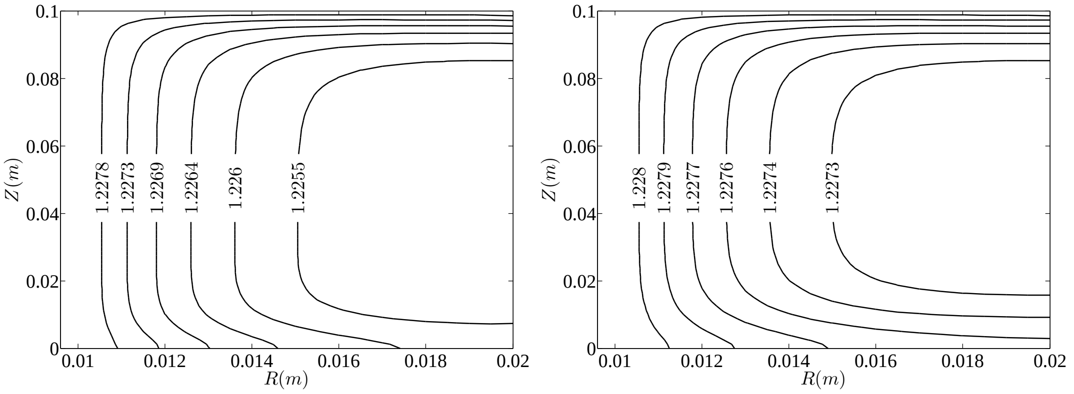

(e) Z = 0.1 m and t = 900 s (f) Z = 0.1 m and t = 1800 s

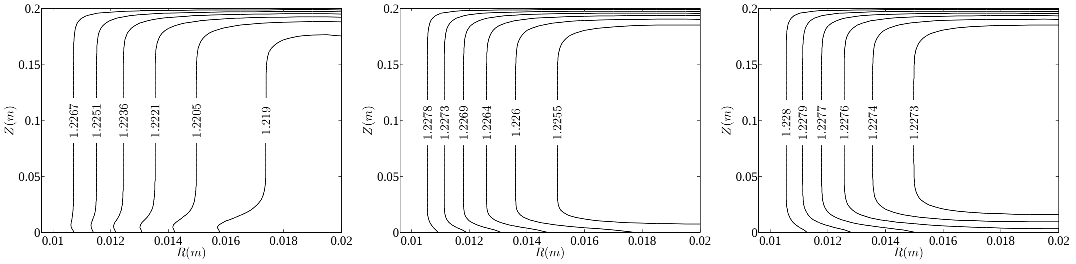

(g) Z = 0.2 m and t = 300 s (h) Z = 0.2 m and t = 900 s (i) Z = 0.2 m and t = 1800 s

Figure 6.6: Transient pressure, kPa, distributions for various adsorbent bed lengths.

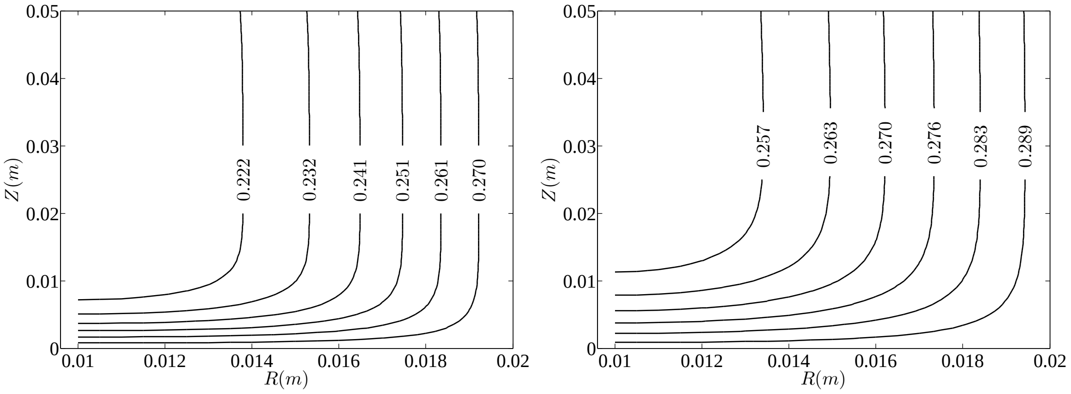

(a) Z = 0.05 m and t = 300 s (b) Z = 0.05 m and t = 900 s

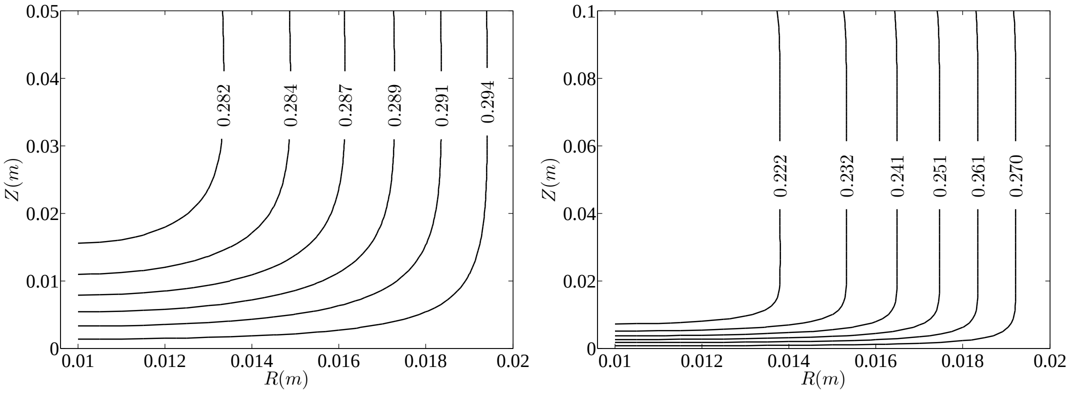

(c) Z = 0.05 m and t = 1800 s (d) Z = 0.1 m and t = 300 s

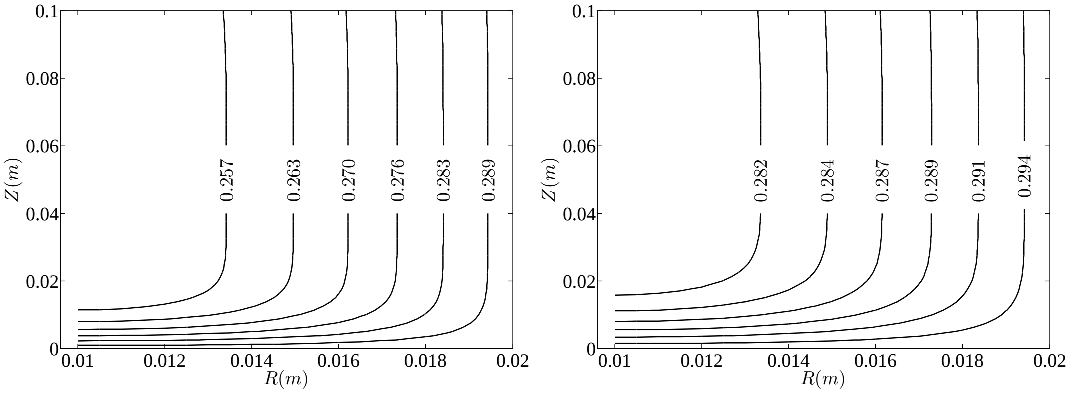

(e) Z = 0.1 m and t = 900 s (f) Z = 0.1 m and t = 1800 s

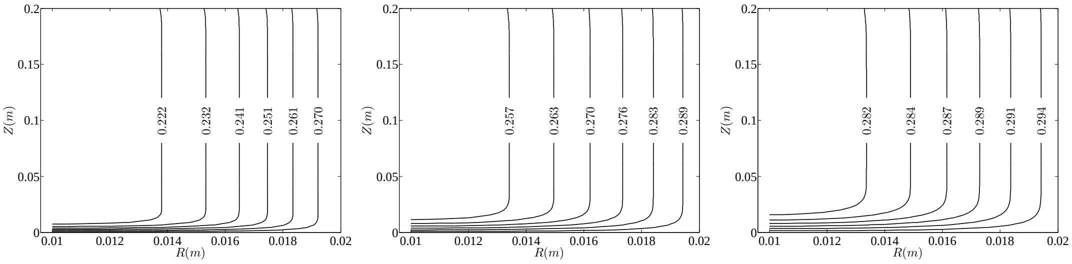

(g) Z = 0.2 m and t = 300 s (h) Z = 0.2 m and t = 900 s (i) Z = 0.2 m and t = 1800 s

Figure 6.7: Transient amount adsorbed, $\mathrm{kg_w kg_{ad}^{-1}}$, distributions for various adsorbent bed lengths.

6.5.4 Effect of the adsorbent bed thickness

The influence of the adsorbent bed thickness on the distributions of the solid phase temperature, pressure and amount adsorbed are presented in Figure 6.8, 6.9 and 6.10, respectively. The adsorbent bed thickness has a great influence on the temperature and amount adsorbed distributions. The heat and mass transfer inside the adsorbent bed depend strongly on the radius when the adsorbent bed thickness is decreased for the given adsorbent bed length. However, the pressure distribution is only slightly affected by the variations in the adsorbent bed thickness, and generally the uniform pressure assumption is valid. The bed approaches thermal, mechanical and chemical equilibrium conditions after 600, 1800 and 3700 s for adsorbent bed thickness 0.005, 0.01 and 0.015 m, respectively. The reason behind this result is that the thermal resistance inside the adsorbent bed increases with increases in the adsorbent bed thickness and this results in longer times to equilibrium. Therefore, the adsorbent bed thickness should be kept as small as possible to improve the heat transfer conditions and as result, reduce the process time. However, this conclusion is based on the assumption that the mass of the shell is neglected. Additionally, it is quite obvious in Figure 6.8 that the adsorbent bed thickness, $R_o - R_i$, should not be greater than 0.01 m for good heat transfer characteristics. Improving the heat transfer conditions makes it possible to reach the chemical equilibrium condition in a shorter time as well since the amount adsorbed is mainly a function of temperature and pressure.

6.5.5 Effect of the convective heat transfer coefficient

The variation of the solid phase temperature, pressure, and amount adsorbed inside the adsorbent bed for values of the convective heat transfer coefficient between the adsorbent bed and heat transfer fluid of 25, 200 and 400 $\mathrm{Wm^{-2}K^{-1}}$ at times of 600, 1200, and 2000 s are presented in Figure 6.11, 6.12 and 6.13, respectively. The simulations were terminated after 2000 s as the system was close to equilibrium. The temperature distribution, and thus pressure and amount adsorbed distributions as well, are nearly insensitive to the variation of the convective heat transfer coefficient due to the low thermal conductivity of the adsorbent material. The pressure distribution throughout the adsorbent bed is generally uniform except at early time steps of the process. This is due to the fact that the temperatures of the solid and gas

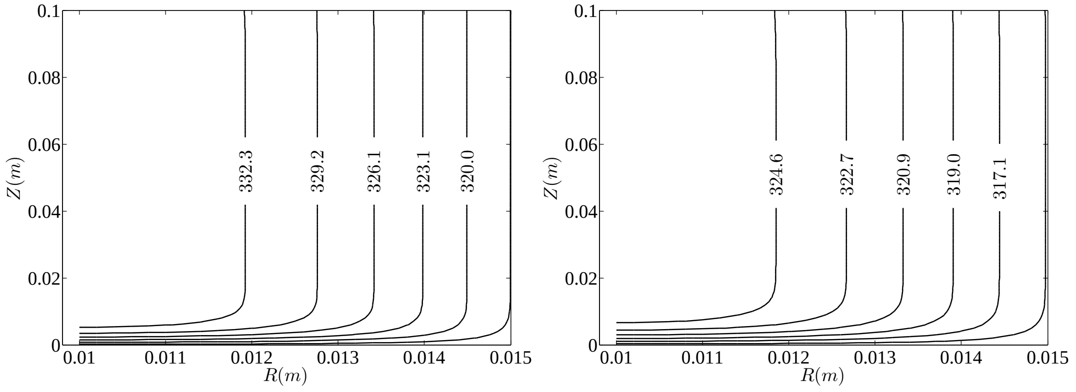

(a) $R_o - R_i$ = 0.005 m and t = 150 s (b) $R_o - R_i$ = 0.005 m and t = 300 s

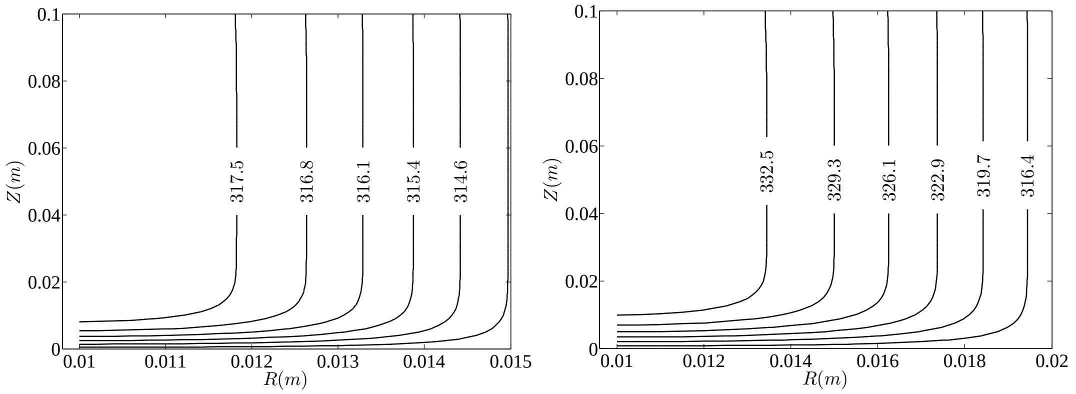

(c) $R_o - R_i$ = 0.005 m and t = 600 s (d) $R_o - R_i$ = 0.01 m and t = 600 s

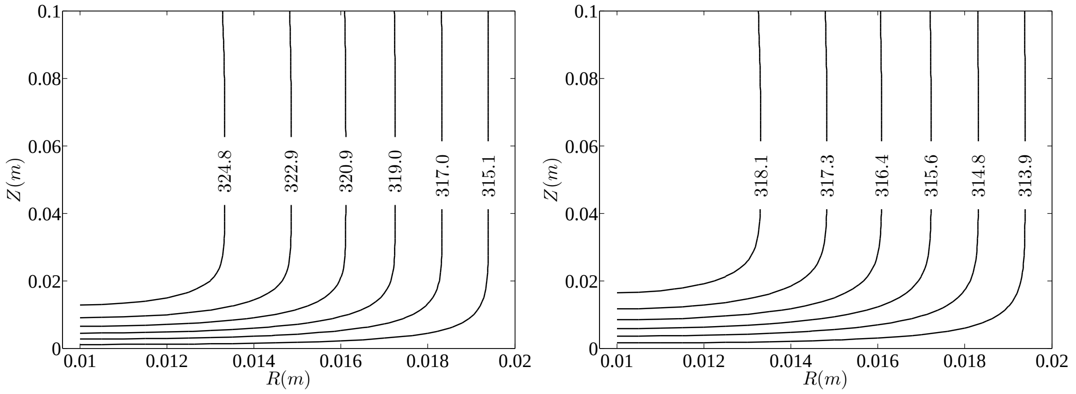

(e) $R_o - R_i$ = 0.01 m and t = 1050 s (f) $R_o - R_i$ = 0.01 m and t = 1800 s

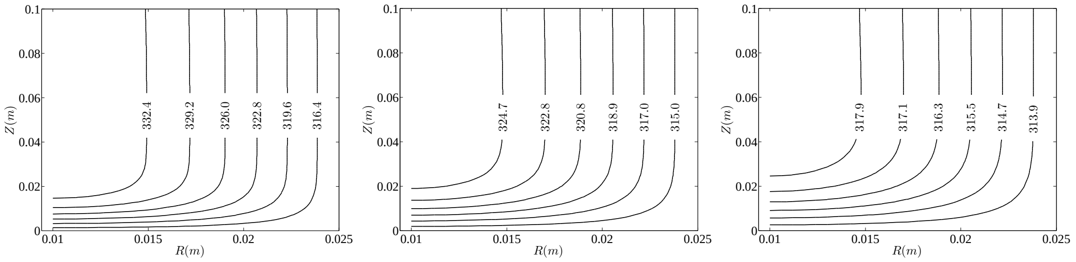

(g) $R_o - R_i$ = 0.015 m and t = 1300 s (h) $R_o - R_i$ = 0.015 m and t = 2200 s (i) $R_o - R_i$ = 0.015 m and t = 3700 s

Figure 6.8: Transient solid phase temperature, K, distributions for various adsorbent bed thicknesses.

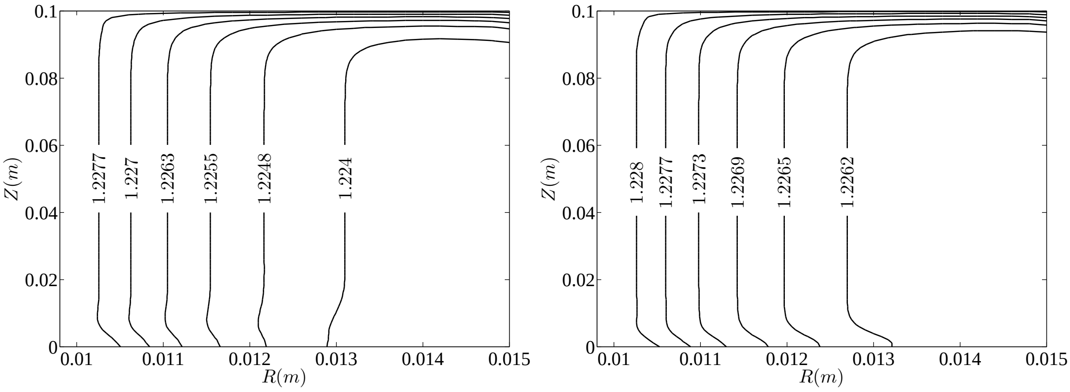

(a) $R_o - R_i$ = 0.005 m and t = 150 s (b) $R_o - R_i$ = 0.005 m and t = 300 s

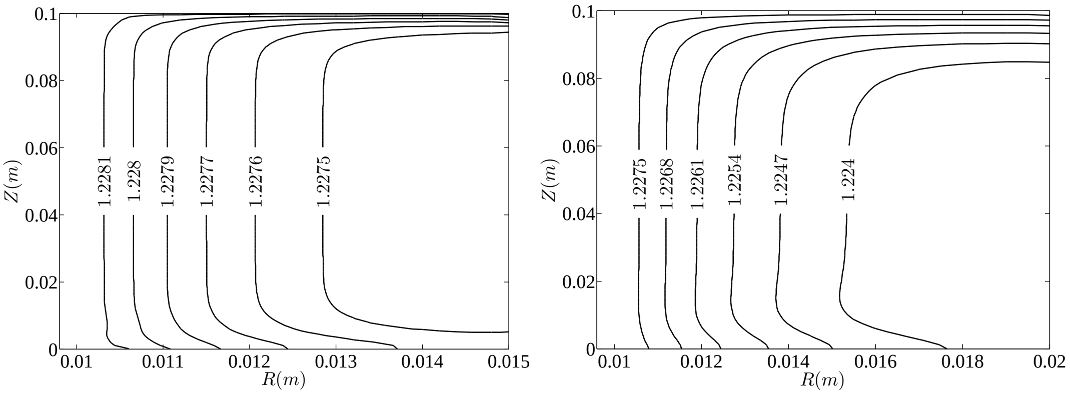

(c) $R_o - R_i$ = 0.005 m and t = 600 s (d) $R_o - R_i$ = 0.01 m and t = 600 s

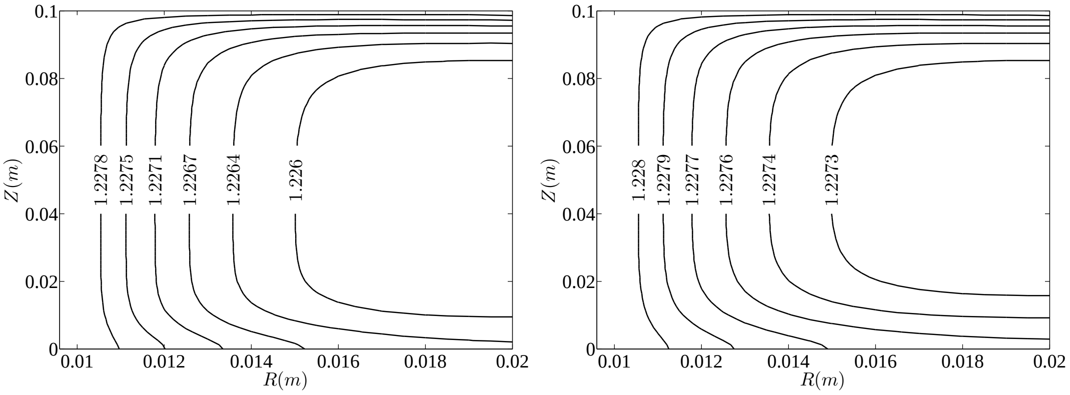

(e) $R_o - R_i$ = 0.01 m and t = 1050 s (f) $R_o - R_i$ = 0.01 m and t = 1800 s

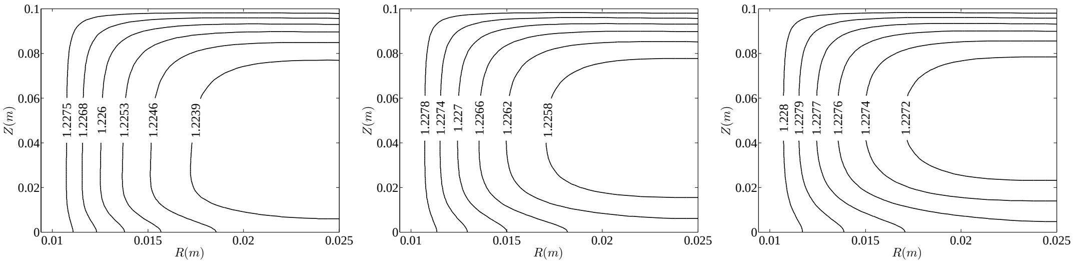

(g) $R_o - R_i$ = 0.015 m and t = 1300 s (h) $R_o - R_i$ = 0.015 m and t = 2200 s (i) $R_o - R_i$ = 0.015 m and t = 3700 s

Figure 6.9: Transient pressure, kPa, distributions for various adsorbent bed thicknesses.

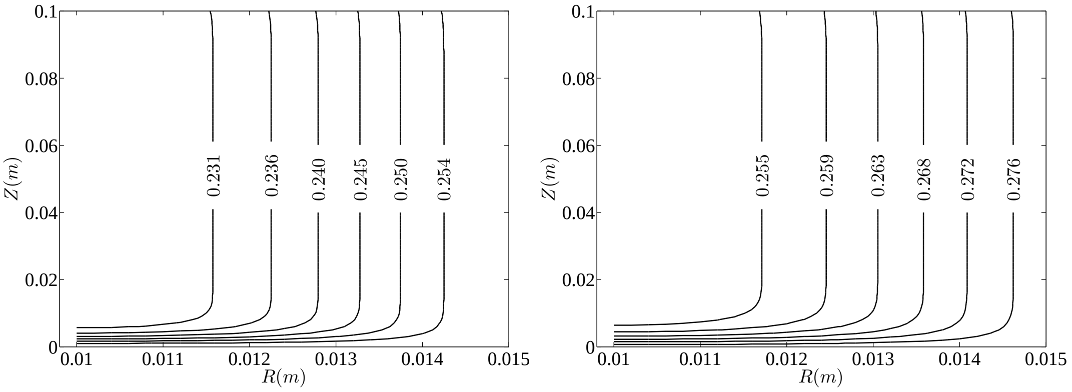

(a) $R_o - R_i$ = 0.005 m and t = 150 s (b) $R_o - R_i$ = 0.005 m and t = 300 s

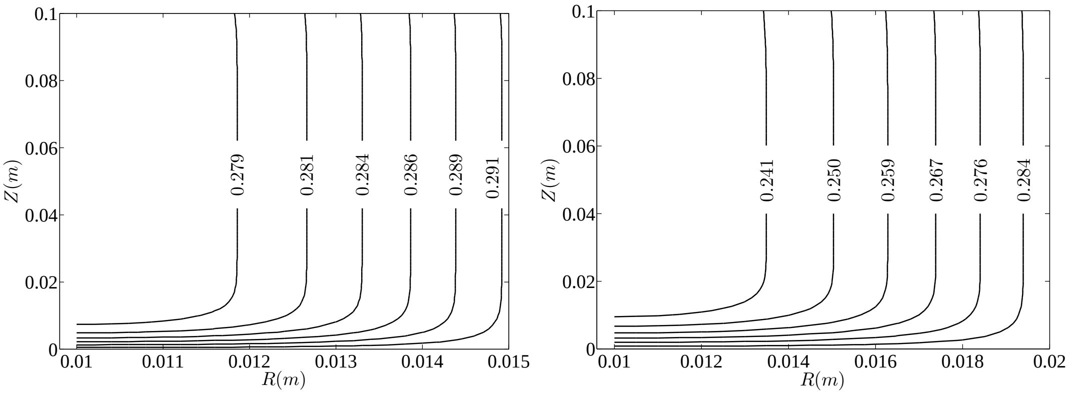

(c) $R_o - R_i$ = 0.005 m and t = 600 s (d) $R_o - R_i$ = 0.01 m and t = 600 s

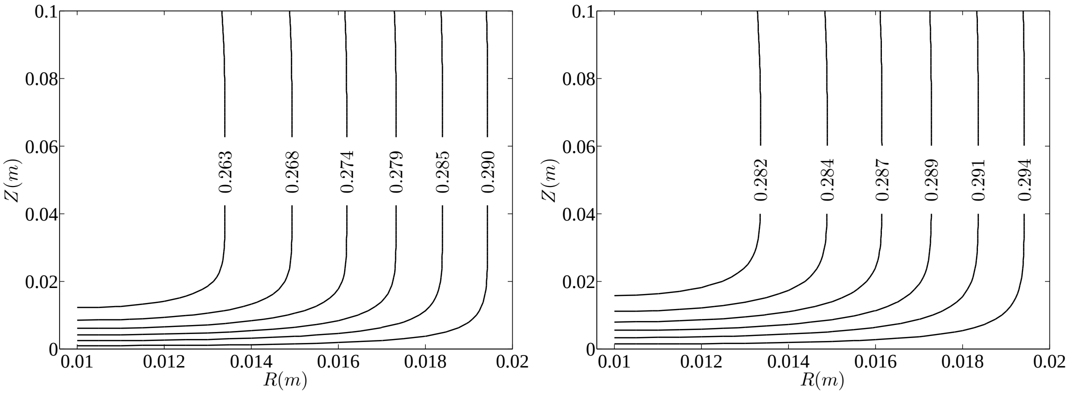

(e) $R_o - R_i$ = 0.01 m and t = 1050 s (f) $R_o - R_i$ = 0.01 m and t = 1800 s

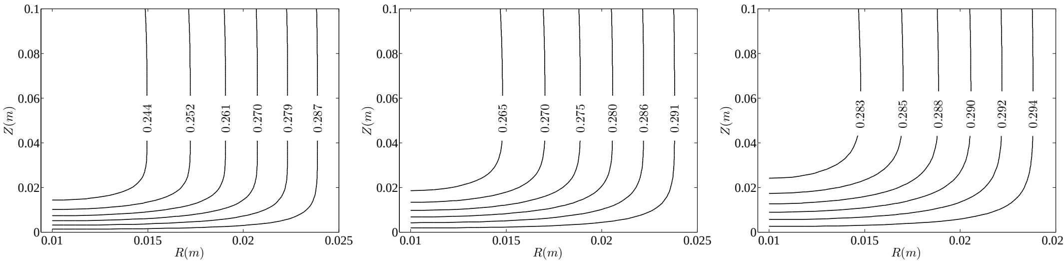

(g) $R_o - R_i$ = 0.015 m and t = 1300 s (h) $R_o - R_i$ = 0.015 m and t = 2200 s (i) $R_o - R_i$ = 0.015 m and t = 3700 s

Figure 6.10: Transient amount adsorbed, $\mathrm{kg_w kg_{ad}^{-1}}$, distributions for various adsorbent bed thicknesses.

phases near the heat transfer boundaries decreases under the given boundary conditions and as a result of this the amount adsorbed increases and the pressure decreases. Consequently, the pressure gradients inside the adsorbent bed becomes significant and adsorbate vapor flows from high pressure to low pressure regions and thus the pressure also decreases at the adiabatic boundaries. In terms of the thermal response of the system little benefit is seen in increasing the value of the convective heat transfer coefficient above 200 Wm^{-2}K^{-1} since there is not any significant difference between the 200 and 400 Wm^{-2}K^{-1} in terms of temperature, pressure and amount adsorbed distributions.

6.5.6 Effect of the thermal conductivity of the solid adsorbent material

The variation of the solid phase temperature, pressure and amount adsorbed inside the adsorbent bed at 150, 300 and 500 s for thermal conductivities of the solid adsorbent material of 0.2, 0.75 and 1.5 Wm^{-1}K^{-1} are shown in Figure 6.14, 6.15 and 6.16, respectively. It is clear in Figure 6.14 that heat transfer conditions inside the adsorbent bed are affected positively by increases in the solid phase thermal conductivity. Temperature gradients in the both directions decrease when the thermal conductivity of the solid adsorbent material is increased. The thermal equilibrium condition (maximum temperature difference within the bed is less than 3 °C) is nearly satisfied for the adsorbent bed having a thermal conductivity of 1.5 Wm^{-1}K^{-1} for process times equal to 500 s. However, at this time instant, temperature gradients are comparatively high for a thermal conductivity of 0.2 Wm^{-1}K^{-1}. Therefore, the specific cooling power of the adsorption cooling system can be improved considerably by eliminating the limiting effects of the heat transfer rate inside the adsorbent bed. Pressure distributions for the three cases are generally uniform but the pressure distribution for the k=1.5 Wm^{-1}K^{-1} is slightly less than the others at early time steps of the process due to the high adsorption rate. This is due to the fact that the heat transfer rate is comparatively high and this results in a sudden temperature drop inside the adsorbent bed. As a result of this, the adsorption rate increases and the pressure decreases, and this pressure drop is not compensated for by an increase in the vapor diffusion flux. Adsorption equilibrium condition inside the adsorbent bed is achieved in a comparatively short period of time when the thermal conductivity of the solid adsorbent material is high.

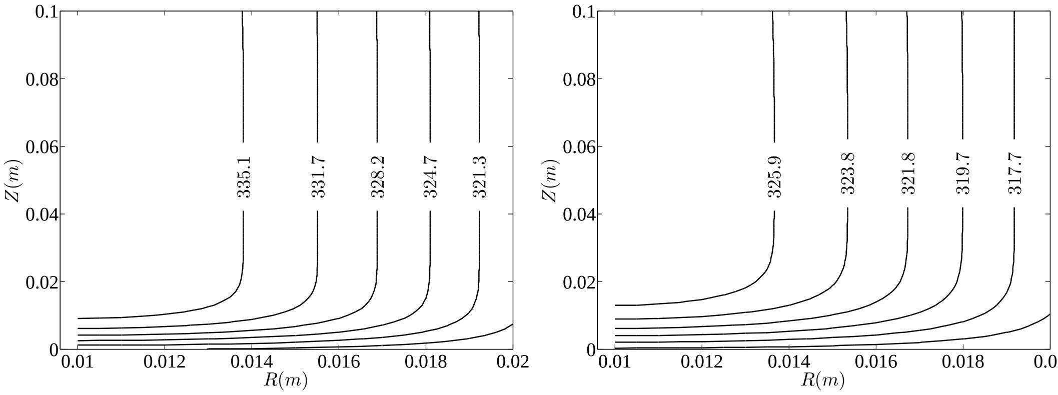

(a) h = 25 Wm^{-2}K^{-1} and t = 600 s (b) h = 25 Wm^{-2}K^{-1} and t = 1200 s

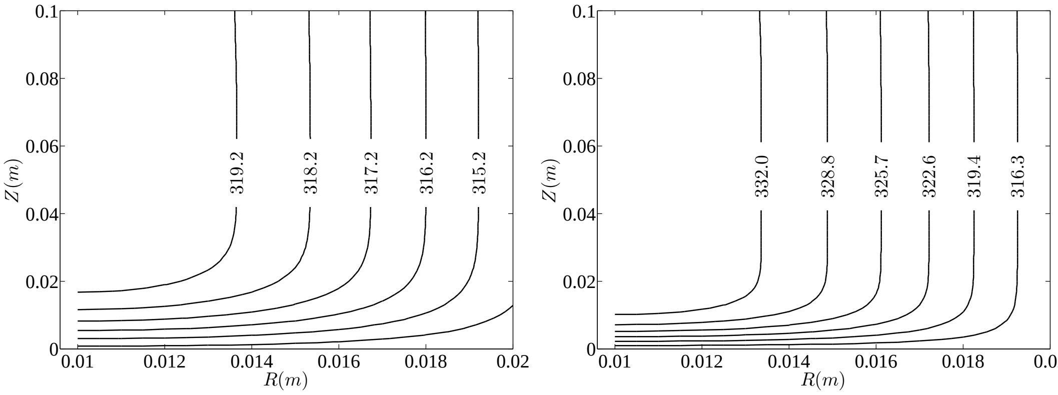

(c) h = 25 Wm^{-2}K^{-1} and t = 2000 s (d) h = 200 Wm^{-2}K^{-1} and t = 600 s

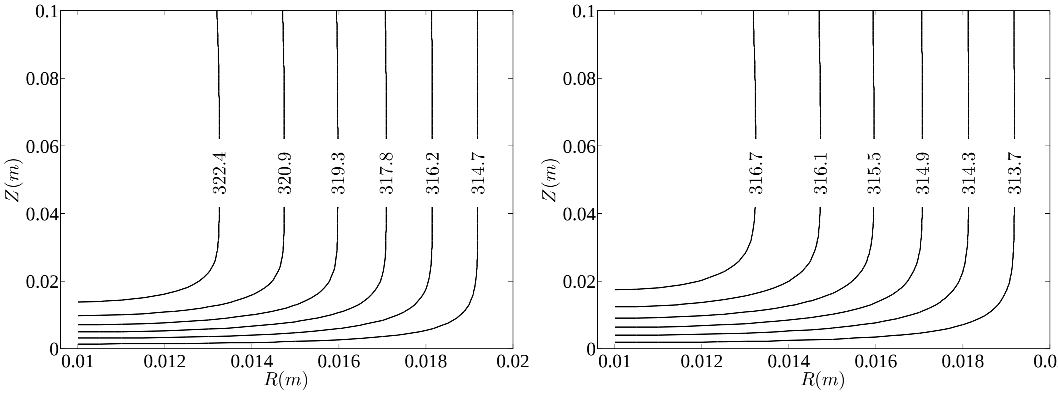

(e) h = 200 Wm^{-2}K^{-1} and t = 1200 s (f) h = 200 Wm^{-2}K^{-1} and t = 2000 s

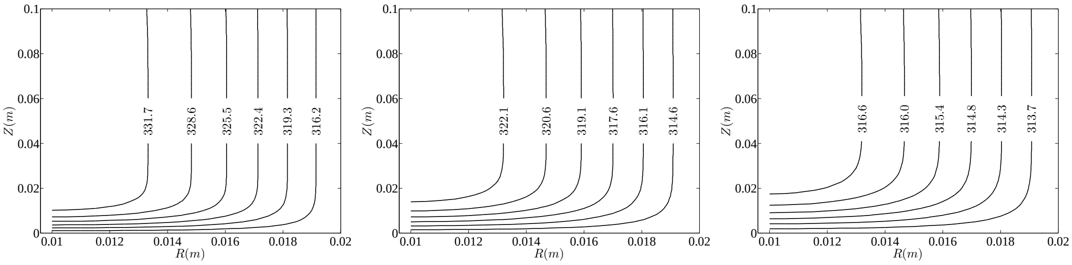

(g) h = 400 Wm^{-2}K^{-1} t = 600 s (h) h = 400 Wm^{-2}K^{-1} t = 1200 s (i) h = 400 Wm^{-2}K^{-1} t = 2000 s

Figure 6.11: Transient solid phase temperature, K, distributions for various values of the convective heat transfer coefficients.

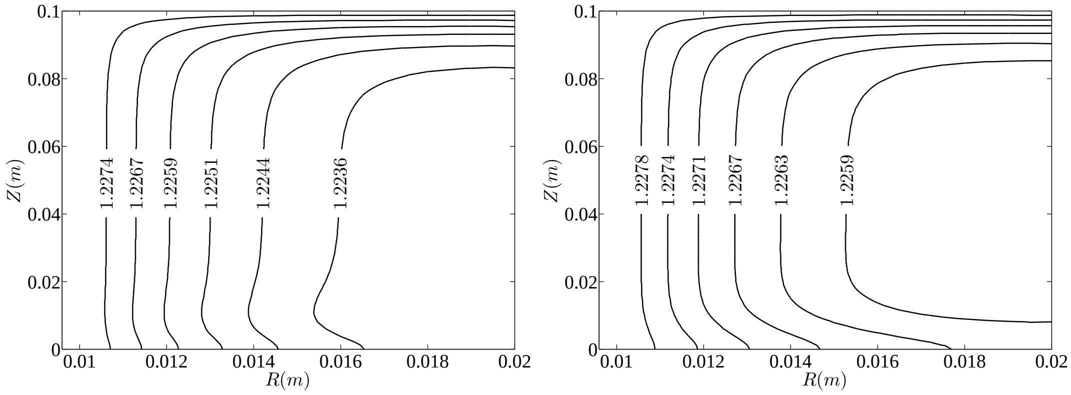

(a) h = 25 Wm^{-2}K^{-1} and t = 600 s (b) h = 25 Wm^{-2}K^{-1} and t = 1200 s

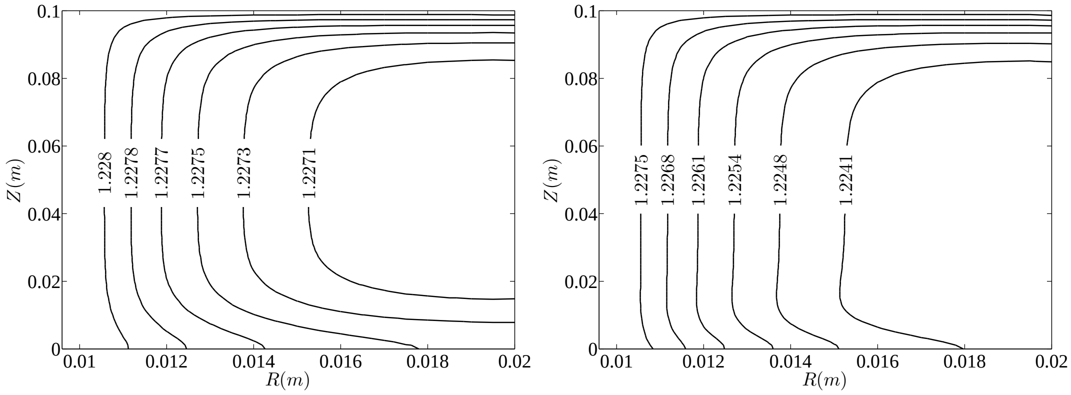

(c) h = 25 Wm^{-2}K^{-1} and t = 2000 s (d) h = 200 Wm^{-2}K^{-1} and t = 600 s

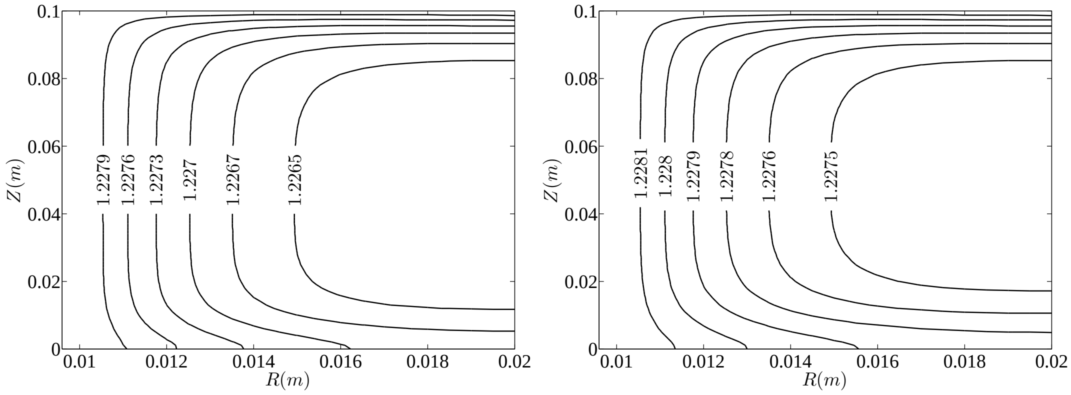

(e) h = 200 Wm^{-2}K^{-1} and t = 1200 s (f) h = 200 Wm^{-2}K^{-1} and t = 2000 s

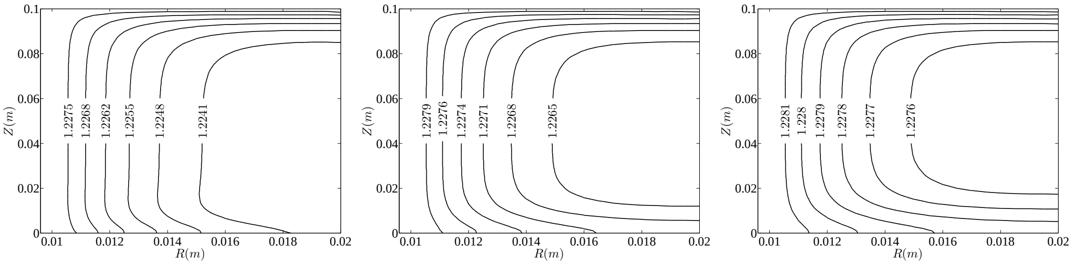

(g) h = 400 Wm^{-2}K^{-1} t = 600 s (h) h = 400 Wm^{-2}K^{-1} t = 1200 s (i) h = 400 Wm^{-2}K^{-1} t = 2000 s

Figure 6.12: Transient pressure, kPa, distributions for various values of the convective heat transfer coefficients.

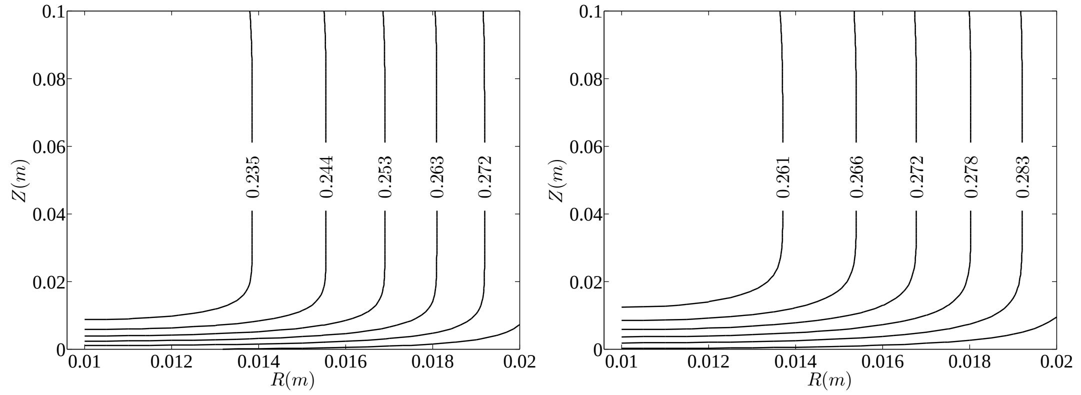

(a) h = 25 Wm^{-2}K^{-1} and t = 600 s (b) h = 25 Wm^{-2}K^{-1} and t = 1200 s

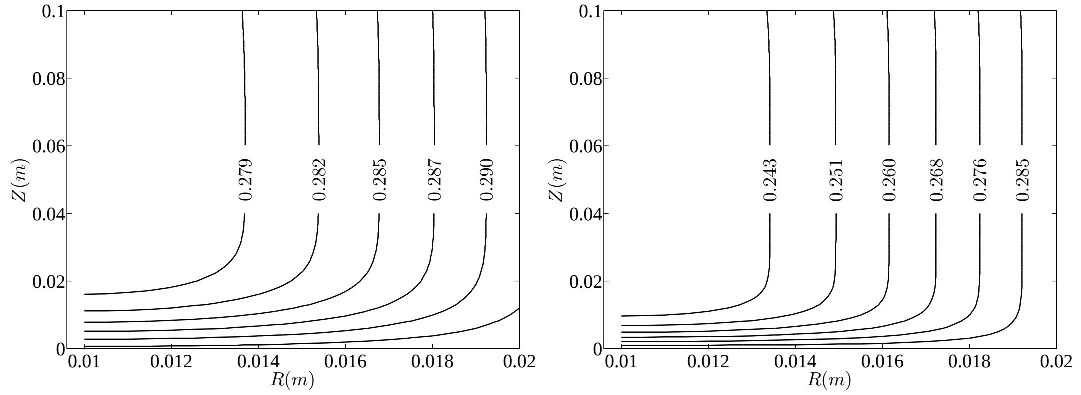

(c) h = 25 Wm^{-2}K^{-1} and t = 2000 s (d) h = 200 Wm^{-2}K^{-1} and t = 600 s

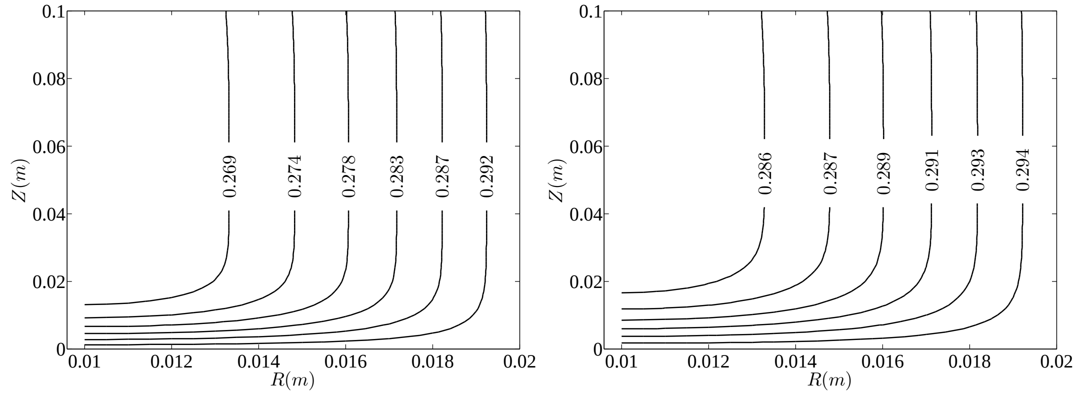

(e) h = 200 Wm^{-2}K^{-1} and t = 1200 s (f) h = 200 Wm^{-2}K^{-1} and t = 2000 s

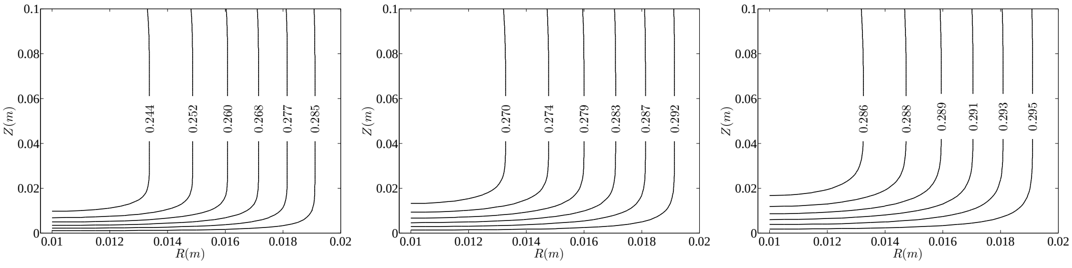

(g) h = 400 Wm^{-2}K^{-1} t = 600 s (h) h = 400 Wm^{-2}K^{-1} t = 1200 s (i) h = 400 Wm^{-2}K^{-1} t = 2000 s

Figure 6.13: Transient amount adsorbed, $\mathrm{kg_w kg_{ad}^{-1}}$, distributions for various values of the convective heat transfer coefficients.

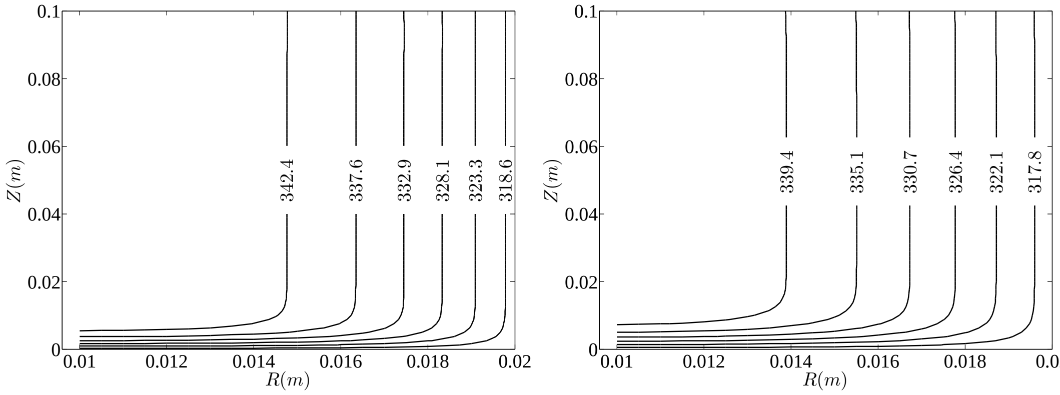

(a) k_s = 0.2 Wm^{-1}K^{-1} and t = 150 s (b) k_s = 0.2 Wm^{-1}K^{-1} and t = 300 s

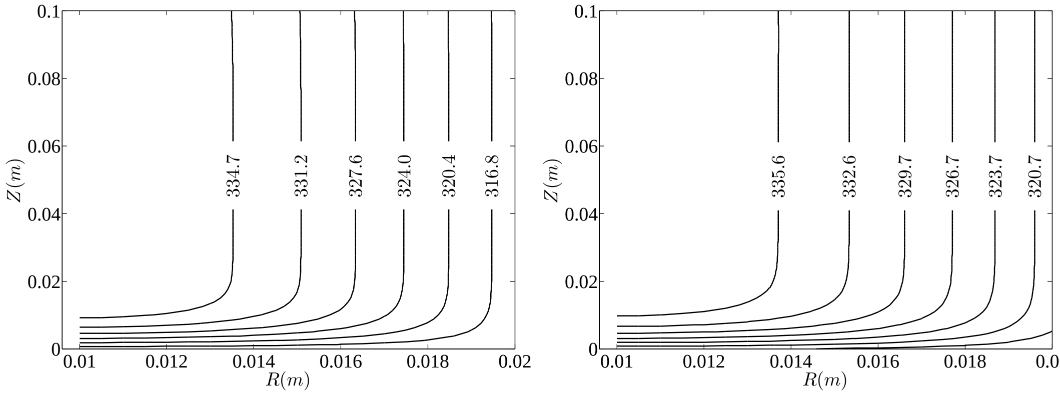

(c) k_s = 0.2 Wm^{-1}K^{-1} and t = 500 s (d) k_s = 0.75 Wm^{-1}K^{-1} and t = 150 s

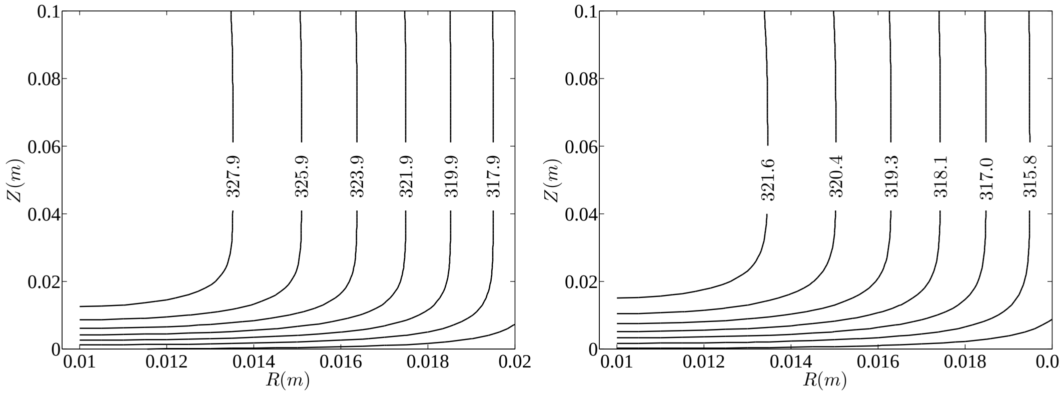

(e) k_s = 0.75 Wm^{-1}K^{-1} and t = 300 s (f) k_s = 0.75 Wm^{-1}K^{-1} and t = 500 s

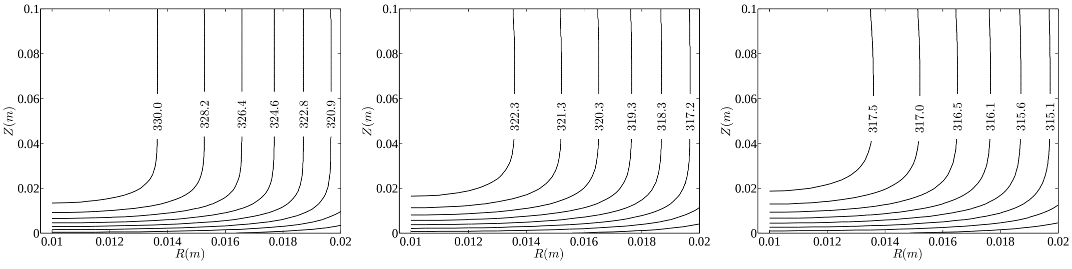

(g) k_s = 1.5 Wm^{-1}K^{-1} t = 150 s (h) k_s = 1.5 Wm^{-1}K^{-1} t = 300 s (i) k_s = 1.5 Wm^{-1}K^{-1} t = 500 s

Figure 6.14: Transient solid phase temperature, K, distributions for various adsorbent material conductivity.

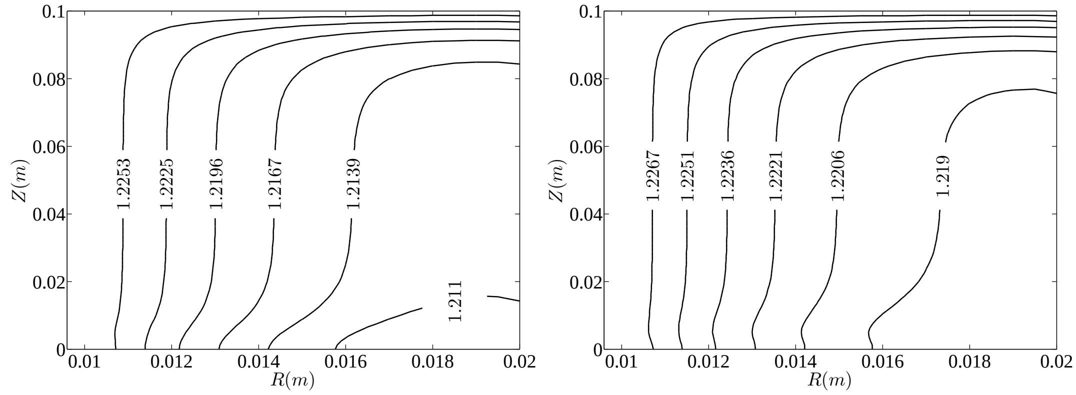

(a) k_s = 0.2 $\mathrm{Wm^{-1}K^{-1}}$ and t = 150 s (b) k_s = 0.2 $\mathrm{Wm^{-1}K^{-1}}$ and t = 300 s

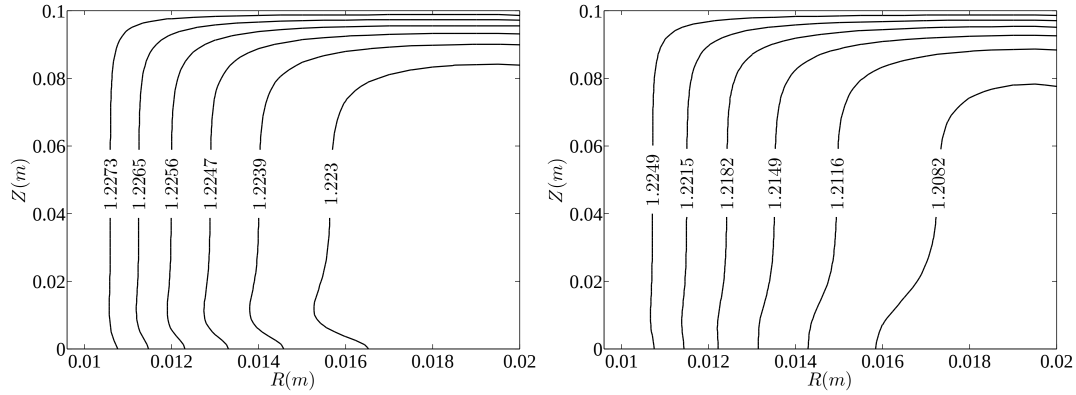

(c) k_s = 0.2 $\mathrm{Wm^{-1}K^{-1}}$ and t = 500 s (d) k_s = 0.75 $\mathrm{Wm^{-1}K^{-1}}$ and t = 150 s

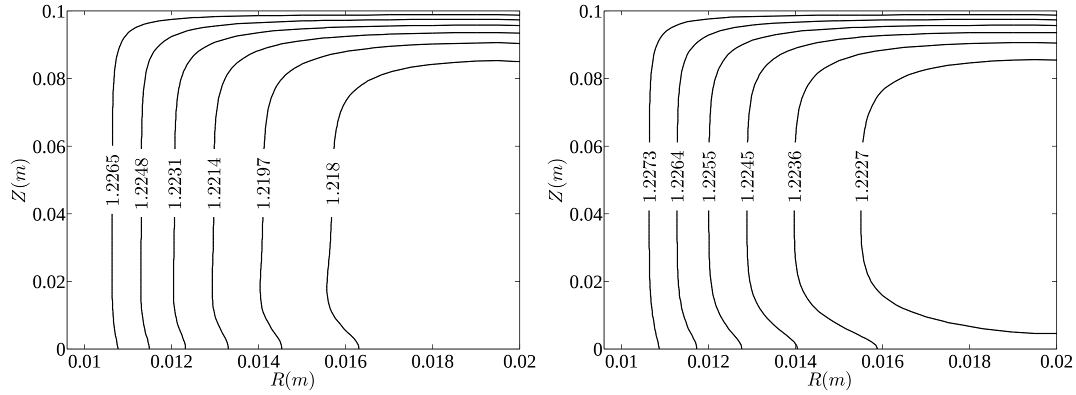

(e) k_s = 0.75 $\mathrm{Wm^{-1}K^{-1}}$ and t = 300 s (f) k_s = 0.75 $\mathrm{Wm^{-1}K^{-1}}$ and t = 500 s

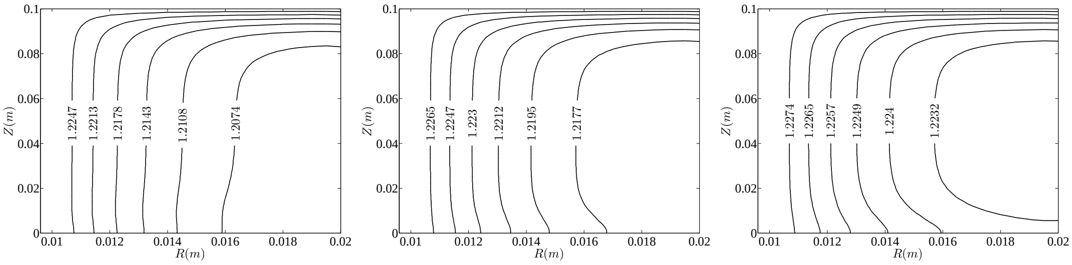

(g) k_s = 1.5 $\mathrm{Wm^{-1}K^{-1}}$ t = 150 s (h) k_s = 1.5 $\mathrm{Wm^{-1}K^{-1}}$ t = 300 s (i) k_s = 1.5 $\mathrm{Wm^{-1}K^{-1}}$ t = 500 s

Figure 6.15: Transient pressure, kPa, distributions for various adsorbent material conductivity.

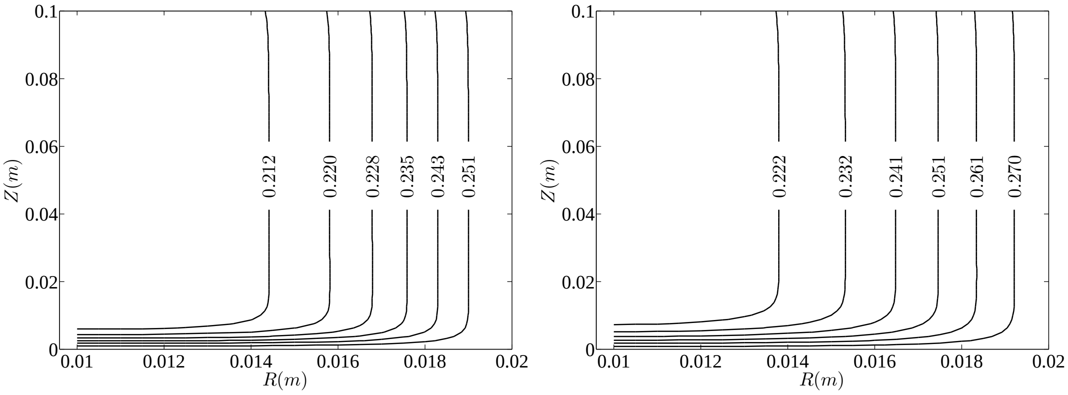

(a) k_s = 0.2 Wm^{-1}K^{-1} and t = 150 s

(b) k_s = 0.2 Wm^{-1}K^{-1} and t = 300 s

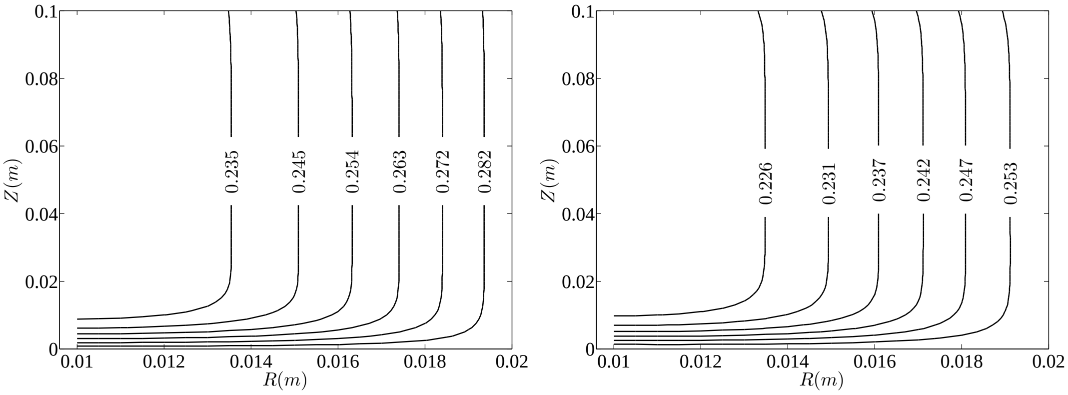

(c) k_s = 0.2 Wm^{-1}K^{-1} and t = 500 s

(d) k_s = 0.75 Wm^{-1}K^{-1} and t = 150 s

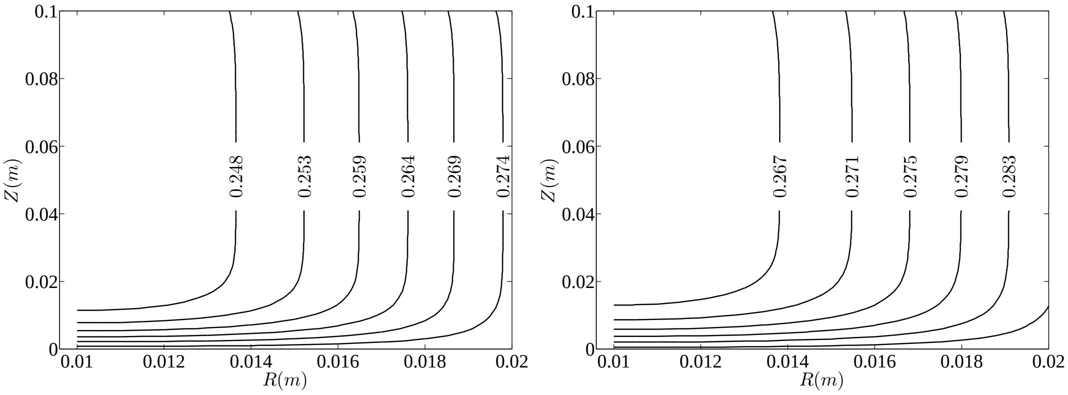

(e) k_s = 0.75 Wm^{-1}K^{-1} and t = 300 s

(f) k_s = 0.75 Wm^{-1}K^{-1} and t = 500 s

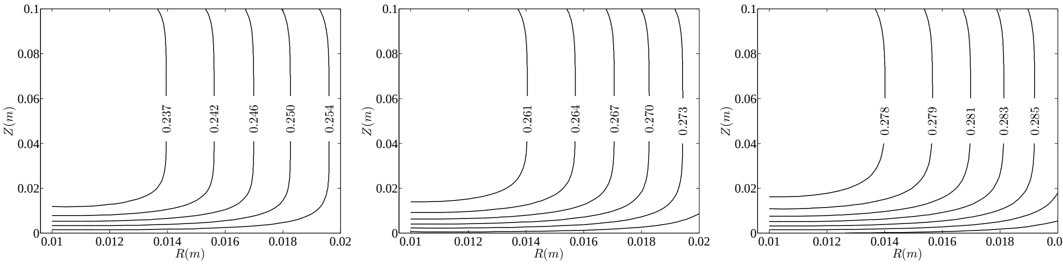

(g) k_s = 1.5 Wm^{-1}K^{-1} t = 150 s

(h) k_s = 1.5 Wm^{-1}K^{-1} t = 300 s

(i) k_s = 1.5 Wm^{-1}K^{-1} t = 500 s

Figure 6.16: Transient amount adsorbed, $\mathrm{kg_w kg_{ad}^{-1}}$, distributions for various adsorbent material conductivity.

CHAPTER 7

CONCLUSIONS

The equilibrium adsorption capacity of water on natural zeolite for adsorption/desorption processes have been measured and the results are discussed in Chapter 2. The maximum adsorption capacity of the natural zeolite-water working pair is nearly 12 % for zeolite temperatures and water vapor pressures in the range 40-150 °C and 0.87-7.38 kPa. As expected, the amount of water that is adsorbed by the adsorbent material increases with increasing refrigerant pressure and decreasing adsorbent temperature. However, the adsorption capacity of the adsorbent material is a weak function of the refrigerant pressure at high adsorbent temperatures. Isosteric heat of adsorption has changed between the values 2500-3800 $\mathrm{kJkg_w^{-1}}$ for the adsorption capacities ranging from 0.12 to 0.02 $\mathrm{kg_w kg_{ad}^{-1}}$.

Using the experimental X, T_{ad}, and T_{sat} data sets, the D-A equation was fitted to only the adsorption data, only the desorption data, and all the sorption data (adsorption + desorption) to yield k, x_o and n values for three types of adsorption capacity models: adsorption, desorption, and average. To get the best fit to the adsorption and desorption experimental data, different n values for adsorption and desorption process are used and thus, the different n values for both processes indicates that there is a hysteresis effect. Although the adsorption and desorption experimental data can be represented by a single D-A equation, the goodness of fit decreases relative to using separate adsorption and desorption models.

A comparison has been made with the other common working pairs: activated carbon-methanol; silica gel-water; and, zeolite13X-water and the conclusions can be summarized as follows:

- Activated carbon-methanol working pair is the best among all pairs in terms of cyclic adsorption capacity for evaporator temperatures used in present study.

- Natural zeolite-water pair has the lowest dependency on evaporator and condenser temperatures.

- Regeneration temperatures are lower for the pairs of activated carbon-methanol and silica gel-water. However, cyclic adsorption capacities of these pairs do not increase significantly with increasing regeneration temperatures.

In the future, experiments will continue with other new generation pairs in order to find a better pair that has low regeneration temperature, better adsorption properties and no need for higher vacuum conditions.

A thermally powered adsorption cooling prototype using natural zeolite-water as a working pair has been designed and built in Chapter 3. The effect of various evaporator temperatures on the performance of the experimental prototype has been investigated and presented. The mean COP, SCP_v and SCP values of the experimental prototype are 0.25, 4.8 kWm^{-3} and 6.4 Wkg^{-1}, respectively. The average cycle time of the experimental prototype is approximately 395 min and the duration of the adsorption process is longer than that of the desorption process.

This work can be considered as a starting point of our research on the thermally powered adsorption cooling systems. Research is going to be conducted on the existing experimental prototype using the various adsorbent-adsorbate working pairs and the experimental prototype is going to be powered by solar energy. In addition to this, research has been carrying out to design a novel adsorbent bed to improve the system performance as well. Finally, Turkey has a large solar energy potential as well as natural zeolite resources. On the other hand, electricity based cooling demand is increasing rapidly especially Mediterranean and Aegean coasts of the country and hence, solar powered adsorption cooling systems using natural zeolite-water as a working pair could be a reliable and economical solution for Turkey to meet this increasing cooling demand partially with a free and environmentally friendly available energy.

A transient one-dimensional local thermal nonequilibrium model has been developed to investigate the effect of several bed parameters on the transient distributions of the temperature (gas and solid phases), pressure and amount adsorbed inside the adsorbent bed of a solid sorption cooling unit during the adsorption process in Chapter 5. In the frame of the numerical results, the conclusions can be summarized as follows:

- In general, the single energy equation is sufficient to describe the temperature field for both solid and gas phases.

- The influence of the diameter of the adsorbent particles on the transient temperature distribution and internal mass transfer coefficient are considerable. The internal mass transfer resistances increase with particle diameter.

- The thickness of the adsorbent bed has a strong influence on the heat transfer rate, and the heat transfer rate increases with decreasing the bed thickness. Additionally, while an increase in bed thickness increases the external mass transfer resistance, the external mass transfer resistance is generally negligibly small for the conditions investigated. The use of the equilibrium adsorption model instead of the LDF model may lead to unrealistic simulation results when the adsorbent bed thickness is small.

- The heat transfer rate and external mass transfer resistance are positively affected by increasing total porosity. The total porosity of the adsorbent bed in the range investigated has a small effect on the transient amount adsorbed distributions for the LDF and the equilibrium adsorption models. However, the internal mass transfer resistance is significant for all cases and it has to be taken into account.

- The effect of the solid phase thermal conductivity of the adsorbent material on the pressure distribution is negligible. The internal mass transfer resistance has to be considered when the solid phase thermal conductivity is high.

Two-dimensional dynamic behavior of the adsorbent bed of an adsorption cooling unit during the adsorption process has been analyzed numerically in Chapter 6. The local thermal non equilibrium model that accounts for both internal and external mass transfer resistances has been developed using local volume averaging method. The followings are the conclusions drawn from the two-dimensional study.

- The temperature difference between the solid and the gas phase is generally insignificant. The local thermal equilibrium assumption is valid. However, the exception is only during the early stages of the process.

- The amount adsorbed difference between the equilibrium and LDF models is only slightly affected by the variation of the parameters investigated and hence, it can be expressed that internal mass transfer resistances are negligibly small.

- For all the cases, the distribution of the gas phase pressure inside adsorbent bed does not vary significantly and thus, spatially isobaric bed assumption can be accepted without leading to any significant computational errors.
- The heat and mass transfer inside the adsorbent bed occurs almost only in the radial direction when the ratio of the adsorbent length over adsorbent bed thickness is greater than 10.
- The adsorbent bed thickness has a large influence on the heat and mass transfer inside adsorbent bed and it should not be more than 0.01 m for a good heat transfer rate and hence, small process time. The heat and mass transfer gradually become one dimensional (only in the r direction) when the adsorbent bed thickness is decreased for a certain value of the adsorbent bed length.
- The heat and mass transfer inside the adsorbent bed is nearly insensitive to the variation of the convective heat transfer coefficient since the thermal conductivity of the solid adsorbent material is low. Therefore, the value of the convective heat transfer coefficient should not be more than 200 $\mathrm{Wm^{-2}K^{-1}}$ since increasing the value of the convective heat transfer coefficient (greater than 200 $\mathrm{Wm^{-2}K^{-1}}$) does not lead to any significant difference on the temperature, pressure and amount adsorbed distributions.
- The solid phase thermal conductivity has a strong influence on the heat and mass transfer conditions inside the adsorbent bed and both conditions of the adsorbent bed can be improved considerably by using highly conductive adsorbent materials, fins, or other thermal enhancements.

Most of the models proposed previously assume local thermal equilibrium between the vapor and solid phases without fully justifying the validity of this assumption. Therefore, one of the innovative points of the one and two dimensional numerical studies is to be considered the local thermal non equilibrium between the gas and solid phases and validity of the single energy equation model that results from this assumption has been studied.

In general, an ideal adsorbent bed is always at thermal, mechanical and chemical equilibrium. The deviation of the bed from thermal, mechanical or chemical equilibrium, or the time required to reach thermal, mechanical and chemical equilibrium, is a measure of the opportunity to improve the performance of the bed through better design. In this model, the deviations from thermal, mechanical, and chemical equilibrium scale with heat transfer, external (interparticle) mass transfer, and internal (intraparticle) mass transfer resistances. The length scales associated with the heat transfer and external mass transfer resistances are on the order of the radius of the adsorbent bed while that associated with the internal mass transfer resistance is on the order of the particle diameter. The significant spatial temperature and pressure gradients indicate that heat transfer and external mass transfer resistance are important, while significant deviations of the amount adsorbed from the equilibrium amount adsorbed indicate that internal mass transfer resistances are important. To improve the performance of the bed, effort should be focused on reducing any significant resistances.

REFERENCES

[1] D.K. Baker, B. Kaftanoğlu, 2008, Trends In Cop For Adsorption Cooling Cycles With Thermal Regeneration And Finite Number Of Beds, 2nd International Conference on Energy Sustainability (ES2008), August 10-14, Jacksonville, FL.

[2] Ministry of Foreign Affairs, The Republic of Turkey. Turkey's Energy Strategy, www.econturk.org, last accessed on 19/12/2011.

[3] TEİAŞ. Türkiye Elektrik Enerjisi 10 Yıllık Üretim Kapasite Projeksiyonu (2007-2016), www.teias.gov.tr, last accessed on 19/12/2011.

[4] J. M. Calm, Emissions and environmental impacts from air-conditioning and refrigeration systems. International Journal of Refrigeration, 25 (2002) 293-305.

[5] M. Izquierdoa, A. Moreno-Rodrígueza, A. González-Gilb and N. García-Hernandoa, Air conditioning in the region of Madrid, Spain: An approach to electricity consumption, economics and CO2 emissions. Energy, 36 (2011) 1630-1639.

[6] A. Avgelis, A.M. Papadopoulosa, Application of multicriteria analysis in designing HVAC systems. Energy and Buildings, 41 (2009) 774-780.

[7] D.S. Kim, C.A. Infante Ferreira. Solar refrigeration options - a state-of-the-art review. International Journal of Refrigeration, 31 (2008) 3-15.

[8] M. Asifa and T. Muneer, Energy supply, its demand and security issues for developed and emerging economies. Renewable and Sustainable Energy Reviews, 11 (2007) 1388-1413.

[9] C. A. Balaras, G. Grossman, H.M. Henning, C. A. I. Ferreira, E. Podesser, L. Wang, E. Wiemken, Solar air conditioning in Europe-an overview. Renewable and Sustainable Energy Reviews, 11 (2007) 299-314.

[10] IEA, 2002, Ongoing research relevant for solar assisted air conditioning systems, Technical Report: IEA solar heating and cooling task 25: Solar-assisted air-conditioning of buildings. International Energy Agency Solar Heating and Cooling Program.

[11] Papadopoulos, A.M., Oxizidis, S., and Kyriakis, N., Perspectives of solar cooling in view of the developments in the air-conditioning sector, Renewable and Sustainable Energy Reviews, 7 (2003) 419-438.

[12] F. Meunier, Adsorptive cooling: a clean technology. Clean Products and Processes, 3 (2001) 8-20.

[13] A. O. Dieng and R. Z. Wang, Literature review on solar adsorption technologies for ice-making and air-conditioning purposes and recent developments in solar technology. Renewable and Sustainable Energy Reviews, 5 (2001) 313-342.

[14] The simulation adsorption of methanol in zeolite MFI. http://zeolites.cqe.northwestern.edu/Members/louie/illustration.html, last accessed on 20/12/2006.

[15] E.E. Anyanwu, Review of solid adsorption solar refrigeration II: An overview of the principles and theory. Energy Conversion and Management, 45 (2004) 1279-1295.

[16] K. Sumathy, K.H. Yeung, Li Yong, Technology development in the solar adsorption refrigeration systems. Progress in Energy and Combustion Science, 29 (2003) 301-327.

[17] Adsorption/Desorption Cycles with Zeolite/Water. http://www.zeo-tech.de/jpg/zeoform.jpg, last accessed on 19/12/2011.

[18] I.I. El-Sharkawy, K. Kuwahara, B.B. Saha, S. Koyama, K.C. Ng, Experimental investigation of activated carbon fibers/ethanol pairs for adsorption cooling system application. Applied Thermal Engineering, 26 (2006) 859-865.

[19] K.C. Ng, H.T. Chua, C.Y. Chung, C.H. Loke, T. Kashiwagi, A. Akisawa, B.B. Saha, Experimental investigation of the silica-gel water adsorption isotherm characteristics. Applied Thermal Engineering, 21 (2001) 1631-1642.

[20] Q. Cui, G. Tao, H. Chen, X. Guo, H. Yao, Environmentally benign working pairs for adsorption refrigeration. Energy, 30 (2005) 261-271.

[21] R.Z. Wang, and B.Q. Wang, Adsorption mechanism and improvements of the adsorption equation for adsorption refrigeration pairs. International Journal of Energy Research, 23 (1999) 887-898.

[22] L.W. Wang, R.Z. Wang, Z.S. Lu, C.J. Chen, K. Wang, J.Y. Wu, The performance of two adsorption ice making test units using activated carbon and a carbon composite as adsorbents. Carbon, 44 (2006) 2671-2680.

[23] W.S. Loh, I.I. El-Sharkway, K.C. Ng, B.B. Saha, Adsorption cooling cycles for alternative adsorbent/refrigerant pairs working at partial vacuum and pressurized conditions. Applied thermal Engineering, 29 (2009) 793-798.

[24] B.B. Saha, A. Chakraborty, S. Koyama, S.H. Yoon, I. Mochida, M. Kumja, C. Yap, K.C. Ng, Isotherms and thermodynamics for the adsorption of n-butane on pitch based activated carbon. International Journal of Heat and Mass Transfer, 51 (2008) 1582-1589.

[25] L.W. Wang, R.Z. Wang, R.G. Olieveira, A review on adsorption working pairs for refrigeration. Renewable and Sustainable Energy Reviews, 13 (2009) 518-534.

[26] D.C. Wang, Z.Z. Xia, J.Y. Wu. Design and performance prediction of a novel zeolite-water adsorption air conditioner. Energy Conversion and Management, 47 (2006) 590-610.

[27] L.Z. Zhang, Design and testing of an automobile waste heat adsorption cooling system. Applied Thermal Engineering, 20 (2000) 103-114.

[28] Y.Z. Lu, R.Z. Wang, S. Jianzhou, M. Zhang, Y.X. Xu, J.Y. Wu., Performance of a diesel locomotive waste-heat-powered adsorption air conditioning system. Adsorption, 10 (2004) 57-68.

[29] R.Z. Wang, J.Y. Wu, Y.X. Xu, W. Wang, Performance researches and improvements on heat regenerative adsorption refrigerator and heat pump. Energy Conversion and Management, 42 (2001) 233-249.

[30] Y.L. Liu, R.Z. Wang, Z.Z. Xia, Experimental performance of a silica gel-water adsorption chiller. Applied Thermal Engineering, 25 (2005) 359-375.

[31] K. Oertel, M. Fischer, Adsorption cooling system for cold storage using methanol/silica gel. Applied Thermal Engineering, 18 (1998) 773-786.

[32] B.B. Saha, A. Akisawa, T. Kashiwagi, Solar/waste heat driven two-stage adsorption chiller: the prototype. Renewable Energy, 23 (2001) 93-101.

[33] D.C. Wang, J.Y. Wu, Z.Z. Xia, H. Zhai, R.Z. Wang, W.D. Dou, Study of a novel silica gel-water adsorption chiller. Part II. Experimental study. International Journal of Refrigeration, 28 (2005) 1084-1091.

[34] M. Li, R.Z. Wang, Y.X. Xu, J.Y. Wu, A.O. Dieng, Experimental study on dynamic performance analysis of a flat-plate solar solid-adsorption refrigeration for ice maker. Renewable Energy, 27 (2002) 211-221.

[35] F. Buchter, P. Dind, M. Pons, An experimental solar-powered adsorptive refrigerator tested in Burkina-Faso. International Journal of Refrigeration, 26 (2003) 79-86.

[36] C. Hildbrand, P. Dind, M. Pons, F. Buchter, A new solar powered adsorption refrigerator with high performance. Solar Energy, 77 (2004) 311-318.

[37] M.H. Chahbani, J. Labidi, J. Paris, Modeling of adsorption heat pumps with heat regeneration. Applied Thermal Engineering, 24 (2004) 431-447.

[38] H. Demir, M. Mobedi, S. Ülkü, Effect of porosity on heat and mass transfer in a granular adsorbent bed. International Communications in Heat and Mass Transfer, 36 (2009) 372-377.

[39] A. Mhimid, Theoretical study of heat and mass transfer in a zeolite bed during water desorption: validity of local thermal equilibrium assumption. International Journal of Heat and Mass Transfer, 41 (1998) 2967-2977.

[40] K.C. Leong, Y. Liu, Numerical modeling of combined heat and mass transfer in the adsorbent bed of a zeolite/water cooling system. Applied Thermal Engineering, 24 (2004) 2359-2374.

[41] L. Z. Zhang, A three dimensional non-equilibrium model for an intermittent adsorption cooling system. Solar Energy, 69 (2000) 27-35.

[42] L. Z. Zhang, L. Wang, Effects of coupled heat and mass transfers in adsorbent on the performance of a waste heat adsorption cooling unit. Applied Thermal Engineering, 19 (1999) 195-215.

[43] W. D. Wu, H. Zhang, D. W. Sun, Mathematical simulation and experimental study of a modified zeolite 13X-water adsorption refrigeration module. Applied Thermal Engineering, 29 (2009) 645-651.

[44] Y.J. Dai, K. Sumathy, Heat and mass transfer in the adsorbent of a solar adsorption cooling system with glass tube insulation. Energy, 28 (2003) 1511-1527.

[45] M. H. Chahbani, J. Labidi, J. Paris, Effect of mass transfer kinetics on the performance of adsorptive heat pump systems. Applied Thermal Engineering, 22 (2002) 23-40.

[46] G. Maggio, A. Freni, G. Restuccia, A dynamic model of heat and mass transfer in a double-bed adsorption machine with internal heat recovery. International Journal of Refrigeration, 29 (2006) 589-600.

[47] L. Marletta, G. Maggio, A. Freni, M. Ingrasciotta, G. Restuccia, A non-uniform temperature non-uniform pressure dynamic model of heat and mass transfer in compact adsorbent beds. International Journal of Heat and Mass Transfer, 45 (2002) 3321-3330.

[48] M. Li, R.Z. Wang, Heat and mass transfer in a flat plate solar solid adsorption refrigeration ice maker. Renewable Energy, 28 (2003) 613-622.

[49] A. El Fadar, A. Mimet, M. Perez-Garcia, Modeling and performance study of a continuous adsorption refrigeration system driven by parabolic trough solar collector. Solar Energy, 83 (2009) 850-861.

[50] K.C. Leong, Y. Liu, Numerical study of a combined heat and mass recovery adsorption cooling cycle. International Journal of Heat and Mass Transfer, 47 (2004) 4761-4770.

[51] K.C. Leong, Y. Liu, System performance of a combined heat and mass recovery adsorption cooling cycle: A parametric study. International Journal of Heat and Mass Transfer, 49 (2006) 2703-2711.

[52] Y. Liu, K.C. Leong, The effect of operating conditions on the performance of zeolite/water adsorption cooling systems. Applied Thermal Engineering, 25 (2005) 1403-1418.

[53] L. M. Sun, Y. Feng, M. Pons, Numerical investigation of adsorptive heat pump systems with thermal wave heat regeneration under uniform-pressure conditions. International Journal of Heat and Mass Transfer, 40 (1997) 281-293.

[54] Y. Pei-Zhi, Heat and mass transfer in adsorbent bed with consideration of non-equilibrium adsorption. Applied Thermal Engineering, 29 (2009) 3198-3203.

[55] A. Jemni, S.B. Nasrallah, Study of two-dimensional heat and mass transfer during absorption in a metal-hydrogen reactor. International Journal of Hydrogen Energy, 20 (1995) 43-52.

[56] J. J. Guilleminot, F. Meunier, Heat and mass transfer in a non-isothermal fixed bed solid adsorbent reactor: a uniform pressure non-uniform temperature case. International Journal of Heat and Mass Transfer, 30 (1987) 1595-1606.

[57] Li Yong, K. Sumathy, Comparison between heat transfer and heat mass transfer models for transportation process in an adsorbent bed. International Journal of Heat and Mass Transfer, 47 (2004) 1587-1598.

[58] F. Duval, F. Fichot, M. Quintard, A local thermal non-equilibrium model for two-phase flows with phase-change in porous media. International Journal of Heat and Mass Transfer, 47 (2004) 613-639.

[59] D.A. Nield, A. Bejan, Convection in Porous Media, 2^{nd} ed., Springer, 1999.

[60] B. Aylangan, Numerical Analysis of Natural Convective Heat Transfer Through Porous Medium, MSc. Thesis, Department of Mechanical Engineering (2006) METU.

[61] Volumetric Flux: Darcy's Law. http://www.owlnet.rice.edu/ceng571/notes.htm, last accessed on 19/12/2011.

[62] H.T. Chua, K.C. Ng, W. Wang, C. Yap, X.L. Wang, Transient modeling of a two-bed silica gel-water adsorption chiller. International Journal of Heat and Mass Transfer, 47 (2004) 659-669.

[63] I. Solmus, C. Yamalı, B. Kaftanoğlu, D. Baker, A. Çağlar, Adsorption properties of a natural zeolite-water pair for use in adsorption cooling cycles. Applied Energy, 87 (2010) 2062-2067.

[64] D. Zhu, S. Wang, Experimental investigation of contact resistance in absorber of solar adsorption refrigeration. Solar Energy, 73 (2002) 177-185.

[65] M. Sözen, K. Vafai, Analysis of the non-thermal equilibrium condensing flow of a gas through a packed bed. International Journal of Heat and Mass Transfer, 33 (1990) 1247-1261.

[66] D.M. Ruthven, Principles of Adsorption and Adsorption Processes, John Wiley and Sons, Inc., 1984.

[67] J. Hager, R. Wimmerstedt, S. Whitaker, Steam drying a bed of porous spheres: Theory and experiment. Chemical Engineering Science, 55 (2000) 1675-1698.

[68] C. Moyne, S. Didierjean, H.P. Amaral Souto, O.T. da Silveira, Thermal dispersion in porous media: one-equation model. International Journal of Heat and Mass Transfer, 43 (2000) 3853-3867.

[69] J. Di, J.Y. Wu, Z.Z. Xia, R.Z. Wang, Theoretical and experimental study on characteristics of a novel silica gel-water chiller under the conditions of variable heat source temperature. International Journal of Refrigeration, 30 (2007) 515-526.

[70] J. Karger, M.D. Rutheven, Diffusion in zeolites and other microporous solids, A Wiley-Interscience Pubs., New York, 1992.

[71] M.A. Rady, A.S. Huzayyin, E. Arquis, P. Monneyron, C. Lebot, Heat and mass transfer in a composite bed of silica gel and macro-encapsulated pcm for dehumidification. 5th European Thermal-Sciences Conference, Netherlands, 2008.

[72] D. Andrew S. Rees, The numerical solution of ordinary and partial differential equations using the Keller Box method, Lecture Notes.

[73] J.C. Tannehill, D.A. Anderson, R.H. Pletcher, Computational Fluid Mechanics and Heat Transfer, 2^{nd} ed., Taylor and Francis, 1997.

[74] L.J.Genik, A computational approach to simultaneous two-dimensional heat and mass transfer in a heat generating porous media, PhD. Thesis, Department of Mechanical Engineering (1998) Michigan State University.

[75] C.A.J. Fletcher, Computational techniques for fluid dynamics 1, 2^{nd} ed., Springer-Verlag, 1990.

CURRICULUM VITAE

PERSONAL INFORMATION

Surname, Name: Solmuş, İsmail

Nationality: Turkish (TC)

Date and Place of Birth: 10 January 1980, Erzincan

Phone:+90 555 652 49 28 (GSM)

email: solmus@metu.edu.tr, er24dem@hotmail.com

EDUCATIONAL BACKGROUND

Visiting Researcher	University of Bath-Mechanical Engineering	2010-2011
M.Sc.	METU-Mechanical Engineering	2006
B.Sc.	Dumlupınar University-Mechanical Engineering	2002

WORK EXPERIENCE

Research and Teaching Assistant, METU-Mechanical Engineering Department (2002-2011)

PUBLICATIONS

- **Solmuş İ.**, Rees D. Andrew S., Yamalı C., Baker D., Kaftanoğlu B., Numerical Investigation of couple heat and mass transfer inside the adsorbent bed of an adsorption cooling unit. International Journal of Refrigeration, doi:10.1016/j.ijrefrig.2011.12.006.
- **Solmuş İ.**, Kaftanoğlu B., Yamalı C., Baker D., Experimental investigation of a natural zeolite-water adsorption cooling unit. Applied Energy 88 (2011) 4206-4213.
- **Solmuş İ.**, Yamalı C., Kaftanoğlu B., Baker D., Çağlar A., Adsorption properties of a natural zeolite-water pair for use in adsorption cooling cycles. Applied Energy 87 (2010) 2062-2067.
- Yamalı C., **Solmuş İ.**, A solar desalination system using humidification dehumidification process: Experimental study and comparison with the theoretical results. De-

salination 220 (2008) 538-551. (also presented at Desalination and the Environment, Halkidiki, Greece, 22-25 April 2007)

- Yamalı C., **Solmuş İ.**, Theoretical investigation of a humidification-dehumidification desalination system configured by a double-pass flat plate solar air heater. Desalination 205 (2007) 163-177. (also presented at EuroMed, Montpellier, France, 21-25 May 2006)

REVIEWER

- International Journal of Thermodynamics
- Applied Energy
- International Journal of Refrigeration
- Microporous and Mesoporous Materials

AWARDS

- Güneş Enerjisi Destekli Doğal Zeolit-Su Çalışma Çiftini Kullanan Adsorpsiyonlu Prototip soğutma sistemi, MMO IV. Necdet Eraslan Project Competition, 2009 (4000 TL).
- DAAD Scholarship for summer school at Technische Universität Berlin, 2007.
- 2214 TÜBİTAK Scholarship

PROJECT WORK

- Kaftanoğlu B., Yamalı C., Baker D., **Solmuş İ.**, Solar powered adsorption cooling system using zeolite/water pair. This work was supported by The Scientific and Technological Research Council of Turkey (TÜBİTAK) project 105M244 and Ataç Holding Company, Antalya, Turkey.
- Yamalı C., **Solmuş İ**, Theoretical and experimental investigations of a humidification-dehumidification desalination system using solar energy, METU BAP Project (2003-2006).

SUMMER SCHOOL PARTICIPATION

- Advanced Separation Technologies in Chemical Engineering at the Process Engineering School at Technische Universität Berlin, 20.8.2007 - 31.8.2007.

LANGUAGE SKILLS

- English (Good)
- French (Beginner)

COMPUTER SKILLS

- AutoCAD
- CadKey
- MatLab
- MathCAD
- LaTex

MEMBERSHIPS

- Turkish Society of Mechanical Engineers
- Member of European Desalination Society